Connectomic analysis of the input to the principal cells of the mammalian cerebral cortex

von Philip Alex Michael Laserstein

Inaugural-Dissertation zur Erlangung der Doktorwürde
der Tierärztlichen Fakultät der Ludwig-Maximilians-Universität
München

Connectomic analysis of the input to the principal cells of the mammalian cerebral cortex

von Philip Alex Michael Laserstein

aus Freiburg im Breisgau

München 2018

Aus dem Veterinärwissenschaftlichen Department

der Tierärztlichen Fakultät

der Ludwig-Maximilians-Universität München

Lehrstuhl für Pharmakologie, Toxikologie und Pharmazie

Arbeit angefertigt unter der Leitung von: Univ.-Prof. Dr. Heidrun Potschka

Angefertigt am: Max Planck Institut für Hirnforschung in Frankfurt am Main

Mentor: Dr. Moritz Helmstaedter

Gedruckt mit der Genehmigung der Tierärztlichen Fakultät

der Ludwig-Maximilians-Universität München

Dekan:	Univ.-Prof. Dr. Reinhard K. Straubinger, Ph.D.
Berichterstatter:	Univ.-Prof. Dr. Heidrun Potschka
Korreferent/en:	Priv.-Doz. Dr. Sven Reese
	Univ.-Prof. Dr. Rüdiger Wanke
	Univ.-Prof. Dr. Cornelia A. Deeg
	Prof. Dr. Andrea Fischer

Tag der Promotion: 10.02.2018

To my family

TABLE OF CONTENTS

ABBREVIATIONS

2P	2-Photon
AD	Apical dendrite
ad sp	Apical trunk spine
AP	Action potential
ATUM	Automated tape collection microtomy
BAC	Back-propagating action potential activated Ca2+ spikes
BC	Bipolar cell
BROPA	brain-wide reduced-osmium staining with pyrogallol-mediated amplification
BSE	Backscattered electrons
CCD	Charged coupled device
CO	Cytochrome oxidase
DAB	Diaminobenzidine
DL	Deeper layer
EM	Electron-microscopy
EPSP	Excitatory postsynaptic potential
EXC	Excitatory neuron
FIBSEM	Focused ion beam scanning electron-microscopy
fMRI	Functional magnetic resonance imaging
GABA	Gamma amino butaric acid
IB	Intrinsic burst neurons
IN	Inhibitory Interneuron
keV	Kilo electron Volts
L4 sn	Layer 4 spiny neuron
L4 spyr	Layer 4 star pyramidal neuron
L4 sst	Layer 4 Spiny stellate cell
LI	Layer 1

LII/III	Layer 2/3
LIV	Layer 4
LV	Layer 5
LVI	Layer 6
M1	Primary motor cortex
MVx	Megavoxel
M	mol
mM	Milli mol
nA	Nano ampere
NaN	Not a number
nm	Nanometers
ob sp	Apical oblique spine
OsO_4	Osmium tetroxide
PATCO	periodic-acid-thiocarbohydrazide-OsO4
PBS	Phosphate buffered Saline
PSD	Postsynaptic density
Pyr	Pyramidal neuron
RS	Regular spiking neurons
S1	Primary somatosensory cortex
S2	Secondary somatosensory cortex
SACs	Starbust amacrine cells
SD	Standard deviation
SEM	Scanning electron-microscopy
SEM	Standard error of the mean
ssTEM	Serial section transmission electron-microscopy
TCH	thiocarbohydrazide
TEMCA	Transmission electron-microscopy camera array
UA	Uranyl acetate
V1	Primary visual cortex
wbPATCO	Whole brain periodic-acid-thiocarbohydrazide-OsO4
XBC	X bipolar cell

I. INTRODUCTION

Sensory reception is fundamental for all species in order to retrieve information about the environment. While human beings primarily rely on visual perception, rodents such as mice and rats gain the majority of sensory inputs via tactile information (VINCENT, 1912; DIAMOND et al., 2008). Hence, these animals show anatomical specializations both in the periphery and in the information processing organ itself – the brain. Tactile stimuli at the muzzle get detected via multiple whiskers, each individually embedded in its own whisker follicle, innervated by sensory fibers. Each individual whisker deflection is projected via thalamo-cortical fibers to the primary somatosensory cortex. As other cortices, this area is anatomically defined in six layered sheets of neuronal tissue, the cortical layers I-VI. Thalamic fibers carrying information from individual whiskers form discrete clusters of synapses in layer 4 which appear as well circumscribed barrels, giving this area its name, barrel cortex (WOOLSEY and VAN DER LOOS, 1970; JONES and DIAMOND, 1995). These barrels display the same spatial configuration as the animal's whisker pad and are therefore considered the cortical processing equivalent to its peripheral tactile organ. It has been proposed that these well circumscribed barrels might form individual functional units vertically spreading throughout all cortical layers as separated "cortical columns". Due to this peculiarity, barrel cortex is the ideal subject for functional and structural studies of cortical signal processing. Therefore it has been extensively studied over the last four decades (FELDMEYER et al., 2013).

Although a large body of work on rodent barrel cortex mainly using electrophysiology as well as light imaging techniques, has led to insights on how sensory information is functionally integrated within and between barrels, the underlying structural basis still remains unresolved. In this context, the question of how sensory information derived from an animal's environment is processed together with feedback information from other cortical areas leading to cortical output and ultimately distinct behaviors such as movement is considered fundamental for neuronal circuit's function. Comprising 70-85 % of all neurons in cerebral cortex (DEFELIPE and FARINAS, 1992), pyramidal neurons appear to play a major role in this process. Their prominent apical dendrite spanning L5 – L1 (RAMÓN Y CAJAL, 1899) constitutes a salient feature of these neurons.

Unlike other neurons, pyramidal neurons in layer 5 display a second dendritic spike initiation zone in their distal apical tuft compartment, a region where long range projections from other cortices also target these structures (SCHILLER et al., 1997; STUART et al., 1997a). The occurrence of back-propagating action potentials together with sub-threshold EPSPs, trigger this second initiation zone to fire Ca^{2+} spikes, a process described as “coincidence detection” (LARKUM et al., 1999). This feature allows the combination of two separate information streams (one feed-forward from thalamus and one feedback stream from projection neurons). This compartment coupling has been shown to be modulated by the number and distribution of apical oblique dendrites (SCHAEFER et al., 2003). While these features have been well studied functionally, the underlying structural, modulatory innervation mechanisms still remain unresolved. The existence of specific inhibitory or excitatory innervations of these structures could only be resolved by synapse mapping. In this context, it is generally unknown whether synaptic contacts between billions of neurons throughout the brain are established randomly, based on geometric proximity as postulated by Peters’ rule (PETERS and FELDMAN, 1976; BRAITENBERG and SCHÜZ, 1998) or synapses are specifically established on distinct neuronal structures. Electron microscopy alone provides the necessary imaging resolution to resolve even the smallest neuronal processes involved in synapse formation. The relatively novel technique of high-resolution connectomics yields at densely mapping such synaptic wiring by the use of volume electron-microscopy.

In this work, nerve tissue from mouse barrel cortex L4 was imaged at high resolution (11.24 x 11.24 x 30 nm) with a volume of 424 x 428 x 84 µm³ using serial block-face scanning electron microscopy (DENK and HORSTMANN, 2004). The dataset is centered at L4 but also contains parts of L5A and L3. Thereby it is well suitable to study the apical oblique compartment. In order to address whether these structures receive cell type specific inputs and to what extent the innervation of apical oblique dendrites differs from other dendrites, innervation profiles of L5 apical trunks and apical oblique dendrites were studied by reconstructing 129 axons with a total path length of 57.75 mm and annotating all established 4979 synapses.

II. LITERATURE REVIEW

1. Connectomics

The mouse brain contains around 157.500 neurons per mm^3 (WHITE and PETERS, 1993), four kilometers of axons per mm^3 forming one synapse per μm^3 (BRAITENBERG and SCHÜZ, 1998) .

Each neuron contacts around one thousand other neurons (HELMSTAEDTER, 2013), making the mammalian brain clearly an outstanding organ. The term "Connectomics" is used for a variety of neuroscientific techniques yielding to map synaptic connections between multiple neurons or potentially within the entire brain, in order to understand the brain's computations such as of perception, behavior and memory.

As it's still unknown whether the brain is organized in distinct modules, which have been proposed to be shaped e.g. as cortical columns (HUBEL and WIESEL, 1963; MOUNTCASTLE, 1978) and could potentially function as isolated units, some laboratories focus on mapping distinct brain regions, whereas brain wiring in its entirety as of whole mouse brains is currently being investigated, too (MIKULA, 2016).

While low resolution techniques such as fMRI and light microcopy are applicable to map connections on the scale of coarse brain areas and sparse neuron populations, high resolution electron microscopy (EM) based connectomics alone allow one to visualize synaptic contacts on a single cell level, making electron microscopy based techniques the currently most feasible method to densely analyze mammalian cortical circuits and potentially whole brains at cellular single cell resolution (MIKULA, 2016).

1.1. Electron microscopy based Connectomics

The minimal required resolution for dense neural circuit mapping is given by the smallest diameters of neuronal processes. Cortical mammalian axons and spine necks have been reported to get as thin as 50 nm, requiring 25- 30 nm minimal resolution, assuming isotropic neuropil (HELMSTAEDTER, 2013). Hence, as light-microscopic techniques are resolution limited by the light's minimal wavelengths and only reasonably applicable for sparsely labeled tissue, it

becomes clear that only electron-microscopy techniques are feasible for dense cortical circuit mapping.

The first electron microscopy based neural circuit analysis was published more than thirty years ago (WHITE et al., 1986), when a group of scientists mapped 302 neurons of the nematode C. elegans, at the time facing challenges with data acquisition and analyses which are partially still present today.

Since then, many different electron microscopic approaches for high resolution connectomic circuit analyses have evolved.

Irrespective of the imaging techniques applied and described in 1.1.3 every connectomical investigation starts with the extraction of nerve tissue or even entire brains, followed by complex staining procedures.

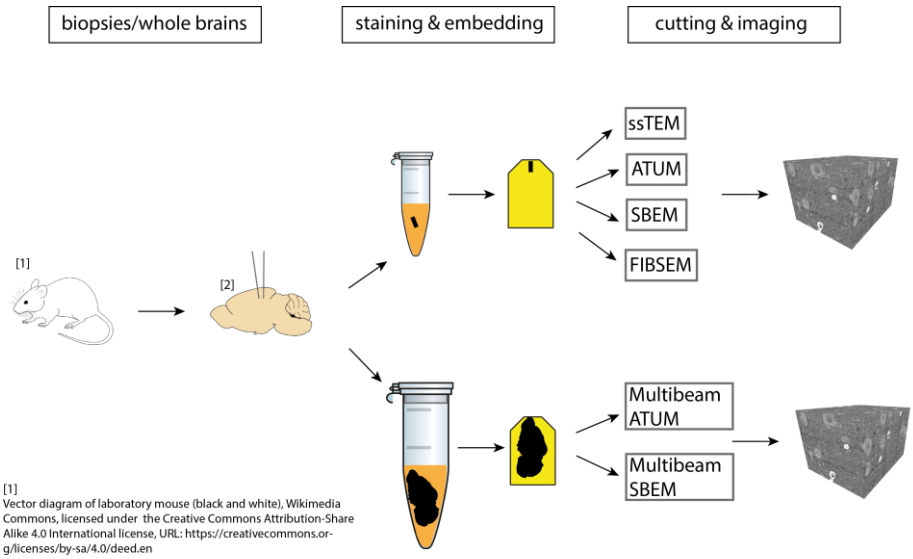

[1]
Vector diagram of laboratory mouse (black and white), Wikimedia Commons, licensed under the Creative Commons Attribution-Share Alike 4.0 International license, URL: https://creativecommons.org/licenses/by-sa/4.0/deed.en
[2]
Sagittal section of a mouse brain, Wikimedia Commons, licensed under the Creative Commons CC0 1.0 Universal Public Domain Dedication, URL: https://creativecommons.org/publicdomain/zero/1.0/deed.en

Figure 1: Overview of EM based connectomics pipelines. Nerve tissue extracted and stained with heavy metal components. Stained tissue blocks EM imaged and cut or vice versa in order to obtain 3D EM stacks for dense neural circuit reconstruction. Depicted dataset kindly provided by K.M. Boergens.

1.1.1. Staining methods for 3D EM

Nerve tissue staining yields contrast for EM, usually provided by heavy metal compounds like Osmium tetroxide (OsO_4) and uranyl acetate (UA) in order to outline neurons, their processes and synaptic vesicles (HUA et al., 2015). In addition, heavy metal compounds provide electrical conductivity, which is crucial

to resolve high resolution images from electrons accelerated on biological tissues to prevent electron accumulations, which would charge up the sample, resulting in poor image and cutting quality (the latter in case of SBEM).

As electron microscopy techniques were historically focused on TEM imaging, simple OsO_4 and UA staining protocols (PALADE, 1952; WATSON, 1958) were well applicable for thin tissue sections. Since en-bloc staining for connectomics became reasonable and required larger volumes and better electrical conductivity (TAPIA et al., 2012), staining techniques for EM also underwent certain innovations.

The first en-bloc 3D EM experiments (DENK and HORSTMANN, 2004) were performed with tissue blocks that underwent fully en-bloc staining with a modified protocol of existing TEM slice staining methods (WYFFELS, 2001). They used potassium ferric cyanide reduced OsO_4 in combination with UA and were capable of providing electrical conductivity and contrast levels, allowing one to distinguish several neural processes from each other. When first mammalian circuit analyses were approached (BRIGGMAN et al., 2011; HELMSTAEDTER et al., 2013), staining required better contrast and larger volumes. Yielding these goals, samples were stained using potassium ferric cyanide reduced OsO_4, thiocarbohydrazide (TCH) amplified OsO_4 and UA (BRIGGMAN et al., 2011; TAPIA et al., 2012) (Fig.2,b). While these staining methods are feasible to stain and image smaller blocks of tissue (~100-200 µm penetration depth, (HUA et al., 2015)), allowing one to stain and image small circuits like retina (BRIGGMAN et al., 2011; HELMSTAEDTER et al., 2013), larger mammalian cortical circuit reconstructions, such as an entire “barrel” requires tissue blocks of at least 1 mm diameter.

One of today’s most commonly used en-bloc staining protocols for targeted nerve tissue samples uses slight alterations of existing rOTO (reduced OsO_4-TCH-OsO_4) staining principles and provides homogeneously stained tissue blocks of 1 mm diameter, allowing for high contrast, high resolution 3D EM imaging (HUA et al., 2015) (Fig.2, e). En-bloc staining yields at high penetration depths and high contrast; there are however certain intrinsic restrictions to achieve these two goals. The more agents binding to membranes and improving the contrast, the lower the availability in greater depths (HUA et al., 2015).

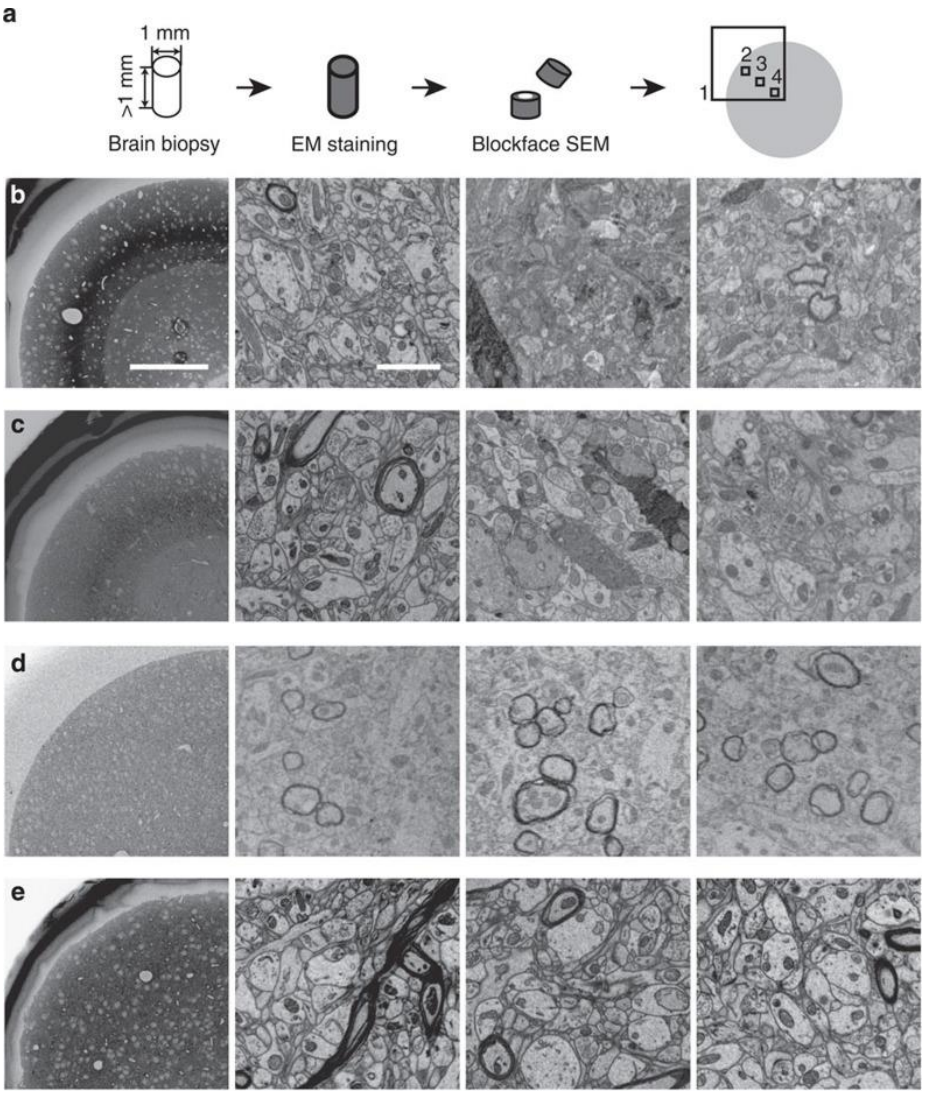

Figure 2: Novel large-scale en-bloc EM staining protocol for dense connectomic circuit reconstruction: protocol comparison. (a) Screening strategy (b-e) SEM images from mouse cortex biopsies screened as indicated in (a) and stained with en-bloc protocols from (BRIGGMAN et al., 2011) (b, rOTO), (HOLCOMB et al., 2013) (c, rOTO), (MIKULA et al., 2012) (c, PATCO), (HUA et al., 2015) (e, rOTO).

From (HUA et al., 2015), reprinted with permission of the Nature Publishing Group

The described staining protocol overcomes these restrictions by two alterations: First, by separating the OsO_4 fixation step from the potassium ferric cyanide enhancement. Second, by splitting the UA staining into one longer step (overnight) at low temperature (4°C), allowing the UA to penetrate deep into the tissue, followed by a two hours UA step (50°C) providing membrane and protein staining (HUA et al., 2015). As this protocol is capable of providing high contrast

en-bloc staining of tissues with at least 1 mm diameter within a couple of days, it makes targeting precision of smaller cortical circuits (~350 µm diameter (HUA et al., 2015) less of a burden, while keeping staining routines at feasible time scales.

1.1.2. Whole brain staining methods for 3D EM

Facing the challenge of densely mapping neural circuits of an entire mouse brain clearly requires special EM staining efforts due to the previously described tradeoff between penetration depth and sample contrast, as well as micro damage caused by prolonged incubation times (HUA et al., 2015).

First attempts to obtain fully en-bloc stained whole mouse brain samples tried to alternate a periodic-acid-TCH-OsO_4 (PATCO) (SELIGMAN et al., 1965) with prolonged immersion, so called whole brain PATCO (wbPATCO) (MIKULA et al., 2012). However, this method only provides good contrast in myelinated axons and is therefore not suitable to densely map neural circuits on a local or brainwide level. Therefore, today's whole brain approaches focus on a new protocol called brain-wide reduced-osmium staining with pyrogallol-mediated amplification (BROPA) (MIKULA and DENK, 2015).

The method is based on rOTO protocols, basically correcting for two whole brain staining barriers: Highly charged chemicals like ferrocyanide ($Fe(CN)_6^{4-}$) seem to be limited in penetration depth in tissue without extracellular space preservation. Secondly, the important OsO_4 amplification step with TCH seems to generate N_2 bubbles, which cause severe tissue damage at immersion times required for whole brain penetration. The BROPA protocol addresses these two problems by adding the organic solvent formamide to the reduced OsO_4 step and by replacing thiocarbohydrazide with a chemical called pyrogallol (1,2,3-trihydroxybenzene) (MIKULA and DENK, 2015).

While this protocol is capable of obtaining high contrast en-bloc stained whole brain samples for SBEM (MIKULA and DENK, 2015; MIKULA, 2016) and serial sectioning techniques (MIKULA, 2017), it appears impractical for staining of smaller tissue volumes (HUA, unpublished).

1.1.3. Imaging methods for 3D EM

Once nerve tissues or entire brains were stained such that they provide electrical conductivity and membrane contrast sufficient for high electron dose exposure, a number of EM imaging and cutting techniques is available to obtain 3D EM volumes for dense circuit reconstructions (Fig. 3 a-d).

While each of the described methods below has both its benefits and certain challenges, they all rely on alternations of two dimensional (2D) electron microscopic imaging combined with slicing or milling tissue from the block's surface. By aligning the acquired images, data is transformed into three dimensional image stacks. Since neural processes like axons and spine necks become as thin as 50 nm (HELMSTAEDTER, 2013), every approach shares the common challenge of avoiding even single section loss over long periods of imaging/alternations of cutting and imaging over months (HELMSTAEDTER, 2013), or in case of whole brain approaches even years (MIKULA, 2016)) in order to maintain tissue continuity.

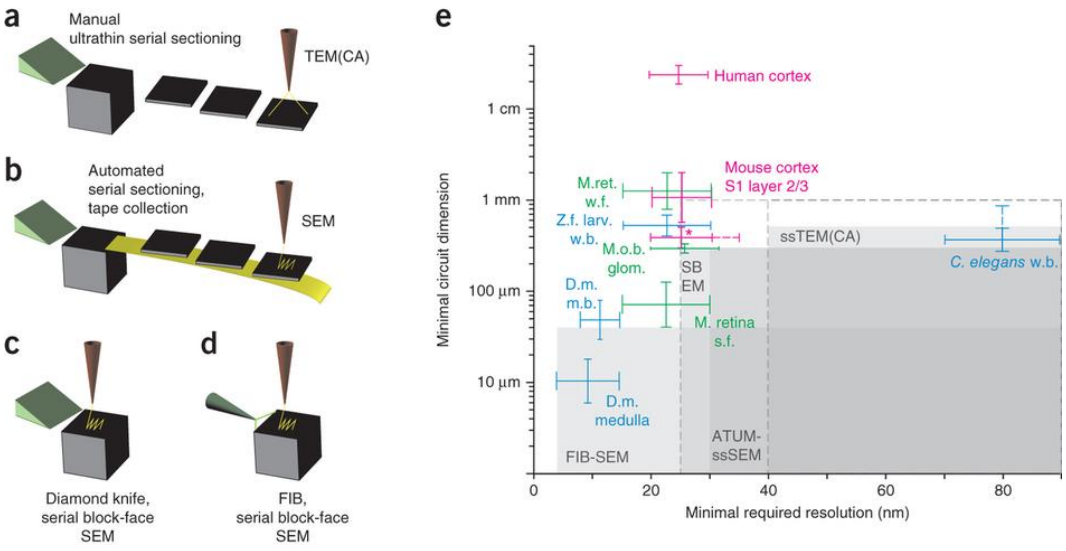

Figure 3: (a-d) Sketches of the four most widely used methods for dense-circuit reconstruction: conventional manual ultrathin sectioning of neuropil (a) followed by TEM or TEMCA imaging (e) Approximate minimal resolution and smallest spatial dimension typically attainable with the imaging techniques in a–d.

From (HELMSTAEDTER, 2013), reprinted with permission of the Nature Publishing Group

1.1.3.1. Serial-section transmission electron-microscopy (ssTEM)

Serial-section transmission EM is probably the most “straight forward” approach when considering imaging biological tissues not only in two, but three dimensions.

Therefore, it is not surprising that this technique was used for first electron microscopy based connectomics studies as described in 1.1. and was more or less the only available 3D EM method until the development of serial-blockface EM (DENK and HORSTMANN, 2004) in the early years of this century.

Blocks of biological tissue are sectioned with a diamond knife in an ultramicrotome at cutting thicknesses of typically 40 – 90 nm (BRIGGMAN and BOCK, 2012; HELMSTAEDTER, 2013) and the resulting sections are manually collected on grids for TEM imaging (Fig. 3, a).

While ssTEM allows for large fields of view and high resolutions in xy, the technique is very limited in minimal cutting thickness (z resolution) and struggles to provide a larger series of continuous slices along the cutting axis due to cutting and collection errors.

As commercially available TEM setups are still suitable to image these kinds of ultrathin sections but very slow in image acquisition, recent customized developments of high speed charge-coupled device (CCD) camera arrays integrated into a TEM setup brought about a system called TEM camera array (TEMCA), which is supposed to scale up data acquisition speed by an order of magnitude (BOCK et al., 2011).

TEM imaging techniques allow for higher electron doses and therefore result in higher resolution and contrast. In addition, representing a non-destructive volume electron microscopy method, all sections could be imaged multiple times and potentially allow for e.g. immune labelling after EM imaging. However, loss of sections, cutting thickness (z-resolution) limitations, slow slice and image acquisition as well as difficult image registration and alignment are still major challenges to be faced when working with volume TEM.

1.1.3.2. Automated serial-section tape-collection electron-microscopy (ATUM)

As previously described, manual slice collection and grid imaging are very time consuming and error-prone, the so called automated serial-section tape-collection technique (Fig.3, b) speeds up the slice generation and yields to lower cutting thickness limitation down to 30 nm (HAYWORTH et al., 2006; SCHALEK et al., 2011; HELMSTAEDTER, 2013).

While the process of cutting and slice collection are fully automated, the slices which are collected on a thin metal coated tape still need to be manually prepared for EM imaging. The first cellular level approaches using this technique were focused on combination with TEM imaging. The tape stripes containing the automatically cut and collected slices were stamped in order to get slices prepared for TEM grids suitable for post-staining and TEM imaging (HAYWORTH et al., 2006).

As the TEM grid preparation and imaging are very time-consuming and difficult to automate, automated tape ultramicrotome approaches today usually focus on combination with SEM setups (SCHALEK et al., 2011). The tape is manually cut into multiple stripes with different lengths in order to be glued on a silicon wafer, so that multiple slices one after another could be imaged in a commercial scanning electron-microscopy (SEM) setup with high electron doses and resolutions.

This technique decreases risk of section loss and makes imaging preparations and imaging itself more practical. While this technique also introduces the obvious possibility to make parallelization of data acquisition with more than one SEM/TEM setup plausible, a more feasible approach today yields at parallelization of electron beams within one setup (EBERLE et al., 2015) rather than single beams of multiple setups.

Tissue containing tape stripes on metal coated silicon wafers get initially registered on low magnifications with light-microscopy within a commercially provided multi-beam scanning electron microscope. Once the field of view is determined, each slice could be imaged with 61 hexagonally arranged electron beams in parallel, allowing acquisition speeds of ~1 GHz (EBERLE et al., 2015).

While this non-destructive method makes high quality data acquisition of large three dimensional nerve tissue blocks feasible, it is still facing certain issues with respect to section loss, wrinkled sections as well as difficulties in image alignment.

1.1.3.3. Serial block-face electron-microscopy (SBEM)

Whereas previously described non-destructive volume EM methods distinctly separate the process of cutting and imaging, allowing for multiple imaging, which makes image aberrations a bit less of a problem, serial block-face electron microscopy (DENK and HORSTMANN, 2004) irretrievably removes every imaged tissue section (Fig. 3, c).

Fully stained tissue blocks get transferred into the chamber of a commercial SEM setup combined with a usually customized microtome installed into the microscope chamber. The block's surface is typically imaged at xy resolutions around 12 nm (BRIGGMAN et al., 2011; HELMSTAEDTER et al., 2013), followed by a usually automatically triggered cut with an ultramicrotomy diamond knife, removing 25-30 nm from the block's surface (BERNING et al., 2015).

Although these imaging and cutting alterations provide large field of view areas and allow for well alignable cutting series of at least 300 µm (BRIGGMAN et al., 2011), cutting biological tissue in an electron-microscope chamber comes at certain costs.

Not only debris particles causing interactions with the electron beam and resulting in focus issues, but also maintaining a sharp diamond knife over longer series of sections constitute present and future challenges for SBEM approaches.

1.1.3.4. Multibeam serial block-face electron-microscopy (SBEM)

While conventional SBEM setups are well-suited to acquire image stacks of local neural circuits, the approach is not very feasible to image very large fields of view, such as necessary for imaging an entire mouse brain. Recent developments in Munich resulted in a unique SBEM setup using 91 parallel electron beams scanning a large block of tissue, exploring the challenge of imaging an entire mouse brain (MIKULA, 2016).

However, exposing such large fields of view to high electron doses comes with the problem of charging and needs in chamber coating (TITZE and DENK, 2013) to prevent defocused images (MIKULA, 2016).

1.1.3.5. Focused ion beam scanning electron-microscopy (FIBSEM)

Representing a second block-face technique, focused ion beam scanning electron microscopy (Fig. 3, d) integrates the process of third dimensional tissue removal into the imaging setup (KNOTT et al., 2008). Stained blocks of nerve tissue are transferred into a FIBSEM chamber and the surface gets subsequently imaged. Each surface imaging procedure is then alternated by a focused beam of Gallium ions. The ion beam is capable of milling tissue with high precision and a minimal milling thickness of down to 8 nm (HAYWORTH et al., 2015).

Although this technique also facilitates high xy-resolutions and is therefore convenient in order to provide high quality EM image stacks, it is limited to a total imaging z depth of 40 µm, therefore limiting its applications to circuit reconstructions which need very high resolutions in small volumes such as in the fly nervous system (HELMSTAEDTER, 2013)

1.1.3.6. Hot knife with FIBSEM

As previously described, FIBSEM setups are limited to a total imaging z depth which is far from making it a suitable technique to image mammalian brain circuits.

In order to overcome the ion beam milling limitation, recent developments brought up a “hot knife microtomy” technique (HAYWORTH et al., 2015).

Tissue blocks are sectioned into slices of typically 20-30 µm thickness with an ultrasonicated diamond knife heated up to 60 °C. The resulting slices are then transferred into FIBSEM chambers for volume imaging. While this approach allows for massive parallelization of high resolution image acquisition and overcomes depth limitations, it still faces challenges with border alignment and potential loss of very small processes within subsequent stacks.

1.1.4. Challenges and milestones of EM-based connectomics

Irrespective of the technique of choice, all approaches in connectomics are currently facing very time-consuming pipelines, each step including major technical (see Table 1 for an overview) and in some cases also pecuniary

challenges (e.g. whole mouse brain data disk storage costs: 2.8 million Euros/human whole brain data disk storage costs: 8.75 billion Euros (MIKULA, 2016)). While first mammalian circuit reconstructions required datasets at the scale of hundreds of Gigabytes (BOCK et al., 2011; BRIGGMAN et al., 2011; HELMSTAEDTER et al., 2013), more recent datasets of up to 100 Terabytes (MORGAN et al., 2016) and upcoming whole brain datasets spanning dozens of Petabytes (MIKULA, 2016), make storage and access of such datasets a challenge in and of itself. Although staining and imaging techniques have improved in quality and speed recently, data analyses currently seems to represent the bottleneck of cortical circuit reconstructions (HELMSTAEDTER, 2013).

Table 1: Overview of 3D EM imaging techniques for connectomics with its respective advantages and challenges.

Imaging technique	Advantages	Challenges
ssTEM/TEMCA	high x/y resolution non-destructive	z resolution limitations manual interaction
ATUM	high x/y resolution non-destructive	z resolution limitations wrinkles, alignment
SBEM	speed good alignment	image aberrations
FIBSEM	high xyz resolution	sample size limitations
FIBSEM + hot knife	high xyz resolution	alignment/continuity of large sections

Mapping neural circuits from 3D EM data requires resolving each neurite's identity as well as its pre- and postsynaptic partners. This task of following single neural processes over sometimes several millimeters path length is still primarily faced by human annotators. The first EM-based connectomics approach (WHITE et al., 1986) was based on a single annotator's reconstructions, demanding ten to twenty thousand hours (HELMSTAEDTER, 2013) for the Connectome of 302 neurons. At the time, neurites were traced by contouring their volumes. This technique is obviously very time-consuming (200-400 h/mm neurite

reconstruction) and prohibitive for larger circuit reconstructions (HELMSTAEDTER et al., 2008a; HELMSTAEDTER et al., 2011).

More recent mammalian circuit reconstructions (BRIGGMAN et al., 2011; HELMSTAEDTER et al., 2013) involved more than one hundred undergraduate annotators providing thousands of reconstruction hours at much higher tracing speed due to a technique known as “skeletonization” (HELMSTAEDTER et al., 2011). Instead of labeling the volume of each neurite, the annotators placed connected nodes at the center of neuronal processes, increasing annotation speed by ~50 fold up to ~3-9 h/mm path length.

While manual annotation proved suitable to reconstructing smaller circuits, required reconstruction times for dense circuit mappings in contemporary and future datasets are (and will be) almost impossible to be accomplished by human annotators alone. Circuit mapping of an entire mouse brain e.g. would require around 500.000 years reconstruction time at total costs of 50 billion Euros (MIKULA, 2016), making such efforts prohibitive for manual annotation. Even though recent efforts at speeding up manual reconstruction times by improving annotation software have been published (BOERGENS et al., 2017), the future of human annotation rather lies in supporting and proofreading of automated, machine-learning based algorithms.

Early automated reconstruction approaches (CHKLOVSKII et al., 2010; JAIN et al., 2010; TURAGA et al., 2010) were lagging behind human annotators accuracy, thus they were so far only applied in combination with massive manual annotation (HELMSTAEDTER et al., 2013; TAKEMURA et al., 2013). However, recently developed machine learning algorithms seem capable of reducing the required human annotation time by a factor of ten, making larger circuit reconstructions (~400 μm^3) within reasonable time scales realistic (BERNING et al., 2015).

In order to obtain neural circuit maps, it is crucial not only to know the identities of neurons in given volumes but also about their synaptic contacts. Manual synapse identification on reconstructed axonal paths currently take ~1.6 h/mm path length, resulting in ~730 years manual annotation time for all the synapses in a volume of 1 mm^3 (STAFFLER et al., 2017). Catching up with automated neuron reconstructions, recent machine learning algorithms like SynEM (STAFFLER et al., 2017) for automated synapse detection achieve very high precision recall,

basically removing the burden of manual synapse annotations and making large volume circuit mapping plausible.

As electron microscopy based connectomics is still evolving in terms of imaging techniques as well as dataset reconstruction constraints, one might have the impression that the field is not yet capable of providing new biological insights. However, EM-based connectomics has already proven to answer questions which would have been impossible to resolve with any other currently available technique (see Table 2 for an overview).

Table 2: Overview of EM-based connectomics milestones.

Year	Method	Key findings	Reference
1986	ssTEM	302 neurons reconstructed and classified Highly locally connected neurons	(WHITE et al., 1986)
2010	ssTEM	Axo-dendritic touch alone does not predict synapses	(MISHCHENKO et al., 2010)
2011	TEMCA + two Photon (2P)	Convergent synaptic inputs onto Interneurons predicted by proximity	(BOCK et al., 2011)
2011	SBEM + two Photon (2P)	Specific wiring of SACs contributes to direction selectivity in the retina	(BRIGGMAN et al., 2011)
2013	SBEM	New cell type	(HELMSTAEDTER

		XBC discovered. Connectivity allows cell type classification	et al., 2013)
2013	ssTEM	Insights in Drosophila's motion detection circuit	(TAKEMURA et al., 2013)
2014	Reanalysis of e2198 from (BRIGGMAN et al., 2011)	Synapse site preference of a BC type on SACs	(KIM et al., 2014)
2014	ATUM	Distinct longitudinal distribution of myelin	(TOMASSY et al., 2014)
2015	ATUM	Physical proximity doesn't predict connectivity	(KASTHURI et al., 2015)
2016	TEMCA + 2P	Connectivity based subnetwork in L2/3 of V1	(LEE et al., 2016)
2016	SBEM	Specific wiring in the zebra fish's olfactory bulb	(WANNER et al., 2016)
2016	ATUM	Network subdivision in thalamus based on dendritic properties	(MORGAN et al., 2016)

2017	SBEM	Selective scaling of synapses during sleep	(DE VIVO et al., 2017)
2017	SBEM + 2P	Synaptic chains driving song behavior in zebra finch	(KORNFELD et al., 2017)

1.2. Light microscopy in connectomics

Light microscopy allowed first insights into cell-type and connectivity-based organization of the brain since reliable neuronal staining methods were discovered at the beginning of the last century (OSTEN and MARGRIE, 2013). As it was the only efficient method for neuron visualization until electron microscopy became feasible, the technique has been broadly used since the second half of the last century in order to map anatomical pathways (one at a time) with neuro-anatomical tracers providing first principles of connectivity motives in the brain (ROCKLAND and PANDYA, 1979; FELLEMAN and VAN ESSEN, 1991).

Recent improvements in neuronal labeling (anterograde & retrograde tracer injections) and automated light-microscopy setups are currently used by several groups in the US (e.g. Allen Institute for Brain Science) to approach a mesoscopic connectivity map of the whole mouse brain ("mesoscopic connectome") (BOHLAND et al., 2009; OSTEN and MARGRIE, 2013).

Like in EM, one potential approach in LM to acquire 3D datasets for brain wide connectivity investigations is to alternate LM imaging with tissue slicing. Although alternative techniques exist (e.g. light sheet fluorescence microscopy LSFM (NIEDWOROK et al., 2012)), research groups yielding the mesoscopic whole mouse brain connectome are currently combining 2P – microscopy (DENK et al., 1990) with a microtome sectioning (~50 µm) the imaged brain block (RAGAN et al., 2012) – a technique called STP (serial two photon tomography).

While mesoscopic connectome approaches are clearly suitable to contribute further insights into brainwide cell-type distribution and point-to-point connectivity between anatomical regions (BOHLAND et al., 2009; OSTEN and

MARGRIE, 2013) they prohibit dense neuronal circuit reconstructions due to resolution barriers and lack of synapse visualization.

Another aspect of LM in connectomics lies in its potential of in-vivo imaging. In order to understand the neural circuits driving e.g. behavior, perception and memory, it is fundamental not only to know about the underlying anatomy but also its function. Combination of functional 2P calcium imaging followed by 3D EM has proven to be valuable in regards to investigating structure-function relationships such as in the retina (BRIGGMAN et al., 2011) and will most likely contribute to cortical structure-function knowledge in the near future (Hua et al, in preparation).

1.3. Electrophysiology in connectomics

For decades, patch clamp and whole cell recordings have been broadly used in order to measure neuronal functional properties, classify cell types and to map neuronal receptive fields (e.g. (BRECHT and SAKMANN, 2002). Although paired electrophysiological recordings additionally allow investigation of synaptic connections at a pairwise level (e.g. (JIANG et al., 2016) and have been shown valuable to obtain insights into circuit driven axonal morphologies (KOELBL et al., 2015), it is highly questionable whether electrophysiology alone could reveal neural circuit organization.

1.4. MRI in Connectomics

There are several ongoing approaches such as functional resting-state fMRI (rfMRI), task fMRI or diffusion MRI in order to map macroscopic functional connections at a low resolution level. While all these approaches are powerful in coarsely revealing connected brain areas by interpreting hemodynamic time courses, they clearly fail to contribute to the notion of brain wiring mechanisms at a local circuit level, due to lack of synapse resolution.

2. Barrel cortex

2.1. Overview

Barrel cortex is one of the most extensively studied regions in rodent neocortex. It was first described in 1970 when two scientists clarified the cellular organization of layer IV somatosensory cortex (WOOLSEY and VAN DER LOOS, 1970). Barrel cortex represents 69 % of the primary somatosensory cortex (LEE and ERZURUMLU, 2005) spanning 2.1 – 2.8 mm^3 in the mouse and 4.7-6.4 mm^3 in the rat (inter-animal variability) (WELKER and WOOLSEY, 1974; RIDDLE and PURVES, 1995).

All tactile stimuli derived from the whisker pad are projected to two thalamic nuclei and subsequently processed within the contralateral barrel cortex. The thalamic fibers form dense accumulations of thalamocortical synapses within layer IV of the barrel cortex, defining discrete structures shaped like a barrel and separated from each other by septa. These bouton formations shape the center of each barrel, which tends to be sparser in cell density than the border area ("barrel wall") (FOX, 2008b). The cells outlining the barrel wall, asymmetrically orientate their dendrites towards the center of the barrel where they receive thalamocortical inputs (SIMONS and WOOLSEY, 1984; FELDMEYER et al., 1999).

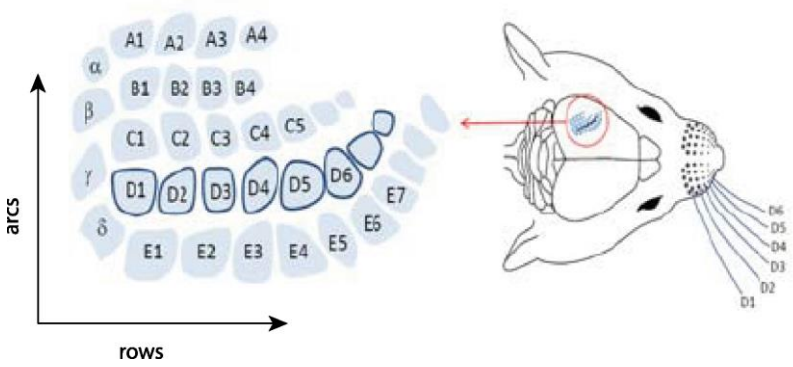

Figure 4: Barrel cortex scheme. Each barrel processes the tactile information from its corresponding contralateral whisker.

Modified from (VALENTE et al., 2012)

So what makes barrel cortex so unique that it is one of the most extensively studied cortices and our model of choice? Investigating the principles of how afferents get computed within neuronal circuits driving cortical output is at the very core of understanding the brain's function. However, the mammalian brain

comprises billions of neurons each contacting around a thousand other neurons, making it very challenging to localize single circuits. As each barrel represents a morphologically and connectivity based unit for its corresponding whisker with just three synapses in its afferent pathway, it intrinsically comprises a well circumscribed unit, introducing experimental advantages. Such units have been previously described in cats and monkeys and are considered to form repeated elements of vertically organized cell arrays ("cortical columns"), each independently computing its thalamic input (MOUNTCASTLE, 1957; MOUNTCASTLE et al., 1957; MOUNTCASTLE and POWELL, 1959).

While most rodents have barrels, carnivores usually have no barrel field despite having whiskers, indicating different importance of somatosensory sensitivity (Table 3).

Table 3: Barrel field species comparison.

Order	**Species**	**Barrels**	**Reference**
Rodent	Mouse	+	(WOOLSEY und VAN DER LOOS, 1970)
Rodent	Rat	+	(KILLACKEY, 1973)
Rodent	Hamster	+	(RICE et al., 1985)
Rodent	Guinea pig	+	(WOOLSEY et al., 1975)
Rodent	Chinchilla	+	(WOOLSEY et al., 1975)
Lagomorpha	Rabbit	+/- (indistinct)	(RICE et al., 1985)
Carnivora	Cat	-	(RICE et al., 1985)

Carnivora	Dog	-	(RICE et al., 1985)
Mustelids	Ferret	+	(MOSCONI and RICE, 1991)
Primates	Rhesus monkey	-	(WOOLSEY et al., 1975)

Although cell density gradients (wall/center, barrel/septum) allow slight light-microscopic visualization of barrels, there are plenty of staining methods resolving the barrel field in more detail. While the most common staining method cytochrome oxidase (CO) visualizes the center of the barrels (mitochondria staining, lots of mitochondria at boutons) (LAND and SIMONS, 1985), other staining methods like Nissl stain outline the barrel wall by contrasting somata (Fig. 5).

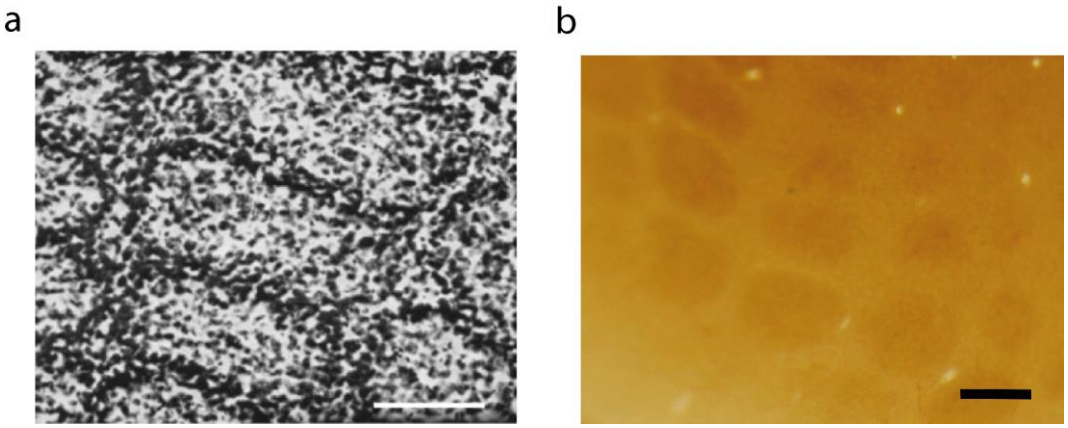

Figure 5: Barrel cortex visualization. (a) Cell density drop from barrel wall compared to septum and barrel core, Nissl stain. Modified from (WOOLSEY and VAN DER LOOS, 1970), reprinted with permission of Elsevier. (b) CO-stain visualizing the barrel core. Scale bars 100 µm.

2.2. Cellular organization and composition

Usually the term barrel field refers to only a subset of the entire barrel field, namely the posteriomedial part of the barrel field. While the anterior lateral part contains smaller barrels, the posteriomedial subfield is shaped by larger barrels. The larger barrels are sized 200 µm x 100 µm in mouse and are arranged in rows referred to as A-E (Fig. 4). The number of rows and arcs could vary between different species, depending on the whisker configuration (WOOLSEY et al., 1975).

Each large barrel is shaped by ~2000 neurons in mouse (PASTERNAK and WOOLSEY, 1975) and ~4400 neurons in rat (MEYER et al., 2010b). In mouse, about 86 % of the neurons are considered to be excitatory and 14 % inhibitory (per barrel) (LIN et al., 1985), while in rat the fraction of reported inhibitory neurons is only around 8 % per barrel and around 11.5 % per column (MEYER et al., 2011).

2.2.1. Excitatory cells

There are three types of excitatory cells in barrel cortex. Although they show certain morphological diversities, they have some things in common: 1) the dendrites of all three cell types are usually equipped with a decent number of dendritic spines, giving rise to the term “spiny neurons” for excitatory cells in LIV barrel cortex. 2) Glutamate is the common neurotransmitter for all spiny neurons.

2.2.1.1. Spiny stellate cells

The spiny stellate is the dominant cell type in layer IV barrel cortex, constituting around 80 % of the excitatory cells (LUBKE et al., 2000; STAIGER et al., 2004). Their star-shaped dendritic pattern varies depending on the location. While spiny stellate cells in the barrel wall tend to asymmetrically project their dendrites towards the barrel center (FELDMEYER et al., 1999), those located in the barrel center or in the septum show more symmetrically arranged dendrites (HARRIS and WOOLSEY, 1979).

2.2.1.2. Star pyramidal cells

Star pyramids differ from spiny stellates by presence of a clear apical dendrite ascending to supragranular layers without reaching layer I (LUBKE et al., 2000). In contrast to pyramidal cells, the soma does not appear triangular (e.g. in Nissl

stain) and the apical dendrite is relatively short, raising the notion of star pyramidal cells being an intermediate form between spiny stellate and pyramidal cells (SIMONS and WOOLSEY, 1984).

2.2.1.3. Pyramidal cells

Pyramidal cells are characterized by the triangular shape of their soma, a distinct main apical dendrite ascending vertically towards pia mater, usually terminating within Layer I and several basal dendrites originating from the cell body's base (RAMÓN Y CAJAL, 1899; FOX, 2008a). As pyramidal cells appear in many different cortical layers (primarily LII/III, LV, LVI), they show certain diversities with respect to their morphological and electrical features. Layer V pyramidal cells, for instance, appear much larger compared to pyramids within LII/III and show several distinct membrane properties (FOX, 2008a). Layer VI apical dendrites of pyramidal cells terminate within L IV, while apical dendrites of LII pyramidal cells sometimes even run parallel to the pia surface, demonstrating the diversity of this cell type.

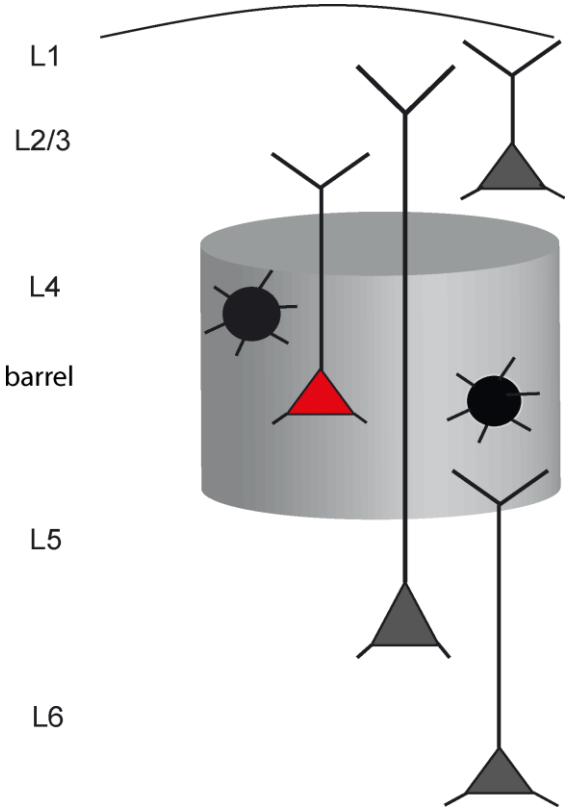

Figure 6: Excitatory cells in barrel cortex. Cell types and their laminar distribution sketched: spiny stellates in black, star pyramidal cell in red, pyramidal cells in grey.

2.2.2. Inhibitory cells

Inhibitory cells (also referred to as GABAergic interneurons or interneurons/INs in this study) modulate cortical excitability and play a role in synchronous activity of pyramidal cells (BUZSAKI and WATSON, 2012).

There are several features to categorize inhibitory cells in the barrel cortex: Morphologically they differ in terms of soma, axon and dendritic arborisation. Furthermore, on a molecular level they express numerous types of neuropeptide transmitters and show different intrinsic membrane properties on an electrophysiological level (GIBSON et al., 1999; MARKRAM et al., 2004). Despite these morphological differences, all inhibitory neurons have one molecular feature in common: their primary neurotransmitter GABA. As excitatory neurons, inhibitory neurons also share a common dendritic feature, which is contrary to spiny neurons, the very sparse or missing distribution of dendritic spines. All subsequent descriptions of different inhibitory cell types will mainly be based on morphological characteristics and axonal projection patterns (HELMSTAEDTER et al., 2009a; HELMSTAEDTER and FELDMEYER, 2010).

2.2.2.1. Basket cells

Basket cells owe their name to their axonal branching pattern which shows several basket-shaped elaborations (RAMÓN Y CAJAL, 1899). Three main types of basket cells have been described so far: small basket cells, large basket cells and, their intermediate form, the nest basket cell (WANG et al., 2002). While small basket cells tend to project their axons rather vertically in close proximity to their dendritic range, large basket cells show much broader trajectories irrespective of columnar borders, sometimes extending through all cortical layers (JONES, 1984). The intermediate form, nested basket cells, appear with axons sized between small and large basket cells (path length wise) and shorter dendrites compared to both of the other types (WANG et al., 2002). All basket cell types have two things in common: 1) their primary neurotransmitter is GABA 2) they all target primarily pyramidal cells' and interneurons' somata and proximal dendrites (JONES, 1984; CZEIGER and WHITE, 1997; FOX, 2008c).

2.2.2.2. Chandelier cells

In contrast to most other cell types, chandelier cells have not been described in the pioneering effort by Ramon y Cajal and Lorente de Nó. They were first identified

many decades later in 1975 and at the time considered to primarily target apical dendrites of pyramidal neurons (JONES, 1975; SZENTÁGOTHAI, 1975). However, electron microscopic reconstructions of Golgi stained material soon revealed the chandelier cell's true primary innervation target: axon initial segments (AIS) of pyramidal cells (SOMOGYI, 1977; FAIREN and VALVERDE, 1980). These axo-axonal synapses are formed by boutons at the terminals of vertically oriented branches arranged in an array like fashion which looks similar to "candlesticks", bringing up the name "chandelier cell" (today also called axo-axonic cells) (WOODRUFF et al., 2010).

By targeting the AIS of pyramidal cells, they can modulate or even "veto" cortical output and suppress back-propagating action potentials. Although chandelier axons occur in all cortical layers, they are primarily found in LII/III (DEFELIPE et al., 1985; INDA et al., 2007).

2.2.2.3. Martinotti cells

Martinotti cells are characterized by their vertically projecting axons forming prominent terminal arbors within layer I (MARTINOTTI, 1889). Contrary to early assumptions, the axons form collaterals on their pathway to layer I, mainly targeting dendritic shafts (~70%) (WANG et al., 2004). In layer I, Martinotti cells target dendritic shafts and to a small fraction also somata of Cajal-Retzius cells (RADNIKOW et al., 2002; WANG et al., 2004). Dendrites of Martinotti cells usually exit the soma in bundles of two to four primary dendrites running vertically towards infragranular layers, sometimes branching extensively (WANG et al., 2004). Martinotti cells appear in all cortical layers II-VI, showing certain layer specific characteristics with respect to their axonal and dendritic morphologies, e.g. in some cases dendrites of LIV Martinotti cells are restricted to LIV, axonal boutons appear spiny (MARKRAM et al., 2004; WANG et al., 2004).

2.2.2.4. Bipolar cells

Bipolar cells owe their name to their very simple dendritic configuration, usually projecting one ascending and one descending primary dendrite from opposite ends of the soma. Like the dendrites, the axon is vertically oriented and is known to form asymmetrical synapses on spines and dendrites of pyramidal neurons (PETERS and KIMERER, 1981). Although interneurons are generally considered to be aspiny (as previously described in 2.3.2.), bipolar cells appear with sparsely

spiny and smooth dendrites to equal ratios (FELDMAN and PETERS, 1978). Bipolar neurons appear in cortical layers II – V (PETERS and KIMERER, 1981).

2.2.2.5. Double bouqet cells/bitufted cells

Similar to bipolar cells, double bouquet cells are named after their vertically projecting dendrites emerging from opposite ends of the soma, branching multiple times. These cells primarily occur in LII/III and their bundled axons (also referred to as "horsetails") vertically project from LII to LV, innervating spines and pyramidal cell's dendrites (YANEZ et al., 2005).

2.2.2.6. Barrel-confined inhibitory interneuron (BIn)

This rather new type of interneuron has been only described in rat barrel cortex so far (KOELBL et al., 2015). It is characterized by its densely branching axonal pattern, which is strictly confined to a single barrel, targeting L4 spiny stellate cells.

2.3. Anatomical pathways

The afferent pathways involved in signal transmission from a given whisker stimulus to barrel cortex are very well understood and lead from whisker follicles through brainstem ganglia to thalamic nuclei.

Each whisker follicle on the muzzle of mouse, rat and other species (see Table 3 for an overview) is specifically innervated by up to 200 afferent axons (axons do not innervate more than one whisker follicle), emerging from the trigeminal ganglion and carried by the infraorbital nerve (LEE and WOOLSEY, 1975; DÖRFL, 1985; LI et al., 1995).

Trigeminal ganglion cells project their axons within the trigeminal nerve to four termination zones in the brainstem, known as trigeminal nuclei (Fig.7, b). As each afferent fiber contains information of only a single whisker follicle, all four trigeminal nuclei (namely nucleus principalis, nucleus interpolaris, nucleus caudalis, nucleus oralis) represent the whisker pad configuration which can be visualized in CO-stained sections for all nuclei but is less distinct in nucleus oralis (MA, 1991; CHIAIA et al., 1992; JACQUIN et al., 1993). As in barrel cortex, these termination zones histologically appear in cylinder shaped subdivisions called "barrelettes" (MA and WOOLSEY, 1984; HENDERSON and JACQUIN, 1995).

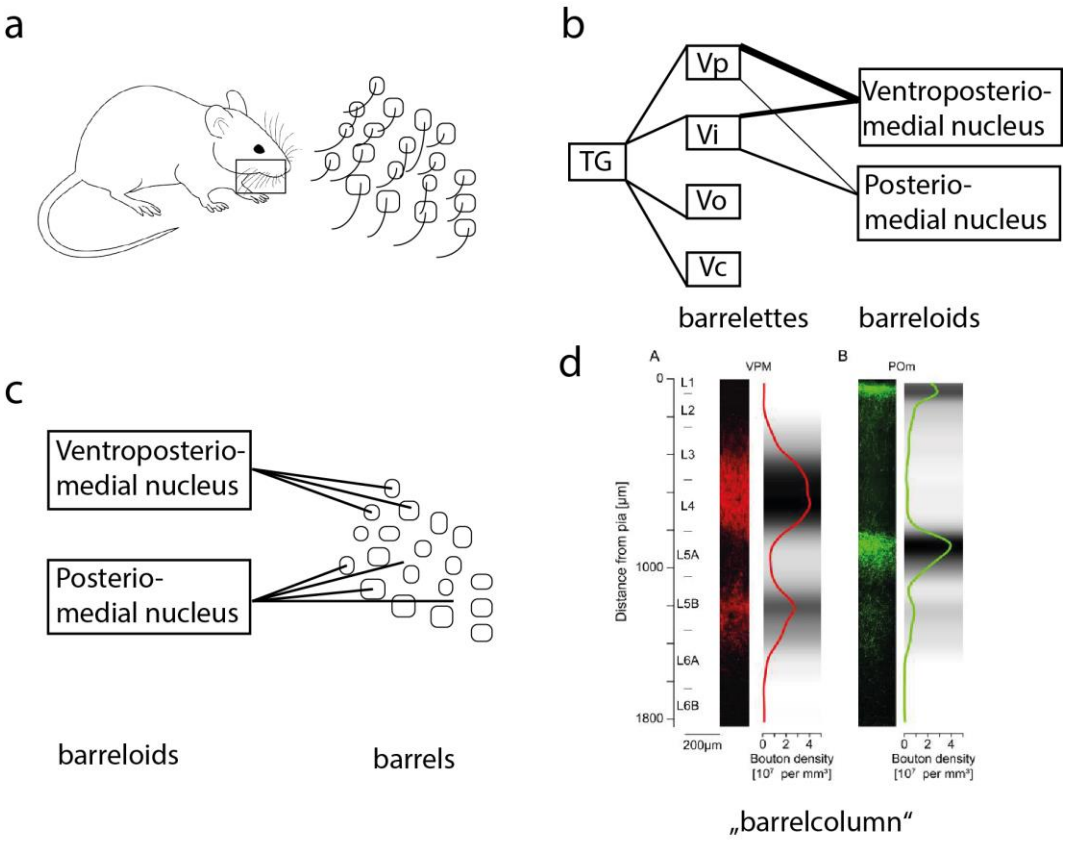

Figure 7: Anatomical pathways to barrel cortex. (a) Whisker pad configuration on mouse/rat muzzle (mouse sketch license, see Fig. 1): (b) Trigeminal projections to thalamic nuclei, line width correlates with innervation strength. (c) Thalamocortical projections to barrel field. (d) Thalamocortical bouton density profiles, from: (MEYER et al., 2010a), reprinted with permission of the Oxford University Press.

Nucleus principalis projects to the ventro-posterior-medial nucleus (VPm) of thalamus, where its termination zones once more form histological compartments related to single whisker information, the so called “barreloids” (VAN DER LOOS, 1976)(Fig.7,b). Nucleus interpolaris provides a second input to VPm and like nucleus principalis also innervates the posterior-medial (POm) thalamic nucleus to a smaller degree (CHIAIA et al., 1991). In contrast to nucleus principalis and interpolaris, nucleus oralis and caudalis target thalamic nuclei to a smaller fraction, but in addition also project to cerebellum and superior colliculus (HALLAS and JACQUIN, 1990; VEINANTE et al., 2000b). All four trigeminal nuclei are interconnected with each other except for nucleus oralis sparing projections to nucleus interpolaris (JACQUIN et al., 1990).

2.3.1. Thalamic projections

VPm barreloids project single whisker excitations to LIII, LVb and LVI but primarily to L IV of barrel cortex confining the barrel field (KILLACKEY, 1973; CHMIELOWSKA et al., 1989; AGMON et al., 1993; LU and LIN, 1993)(Fig. 7, c, d). LIV, LVb and LVI respond to whisker stimuli almost simultaneously while LIII fires weaker and delayed (DE KOCK et al., 2007).

POm fibers mainly project to the area surrounding the barrels, so called septa in a complementary fashion (KORALEK et al., 1988; WIMMER et al., 2010)(Fig.7, c). While this septa innervation is considered highly specific for POm axons, VPm projects to barrel and septal areas (VEINANTE and DESCHENES, 1999; FURUTA et al., 2009; WIMMER et al., 2010). In contrast to VPm, POm primarily targets LI and LVa, extending its axonal arbors broadly throughout septa, suggesting that POm provides modulatory inputs to S1 rather than a parallel pathway (VIAENE et al., 2011)(Fig.7, d). In addition, POm provides some inputs to S2 and M1 (DESCHENES et al., 1998).

Thalamic inputs constitute about 10-23 % of all synapses on spiny stellate's spine heads and about 8% of all input synapses on GABAergic interneurons in barrel cortex (BENSHALOM and WHITE, 1986; KELLER and WHITE, 1987; STAIGER et al., 1996).

2.3.2. Excitatory columnar pathways

As thalamic inputs comprise only a small fraction of input synapses on LIV barrel cortex, they are highly outnumbered by intra-cortical, translaminar circuitries and LIV interconnections (FELDMEYER et al., 1999), indicating the complexity of cortical signal processing.

The current view of how thalamic inputs are processed in barrel cortex is described as a so-called "canonical microcircuit" (DOUGLAS and MARTIN, 1991): LIV projects vertically to LII/III neurons which send descending fibers to infragranular LV (SCHUBERT et al., 2001; FELDMEYER et al., 2002; LUBKE et al., 2003; FELDMEYER et al., 2013).

Layer IV axons are horizontally confined to the barrel column and tend to be highly interconnected (~20-30 % paired connectivity) (FELDMEYER et al., 1999) with other LIV neurons of the same cell type (star pyramids-star pyramids, spiny stellates-spiny stellates) (COWAN and STRICKER, 2004). While axons of

spiny stellate cells strictly respect the barrel borders, some star pyramidal cells also project to other barrel columns, suggesting separate circuitries for these cell types (SCHUBERT et al., 2003). Despite the previously described “wiring rules” for the canonical microcircuit initially defined in V1 (DOUGLAS and MARTIN, 1991), barrel cortex shows some violation of what is suggested to be a “standard cortical column”, repeatedly present throughout cortex. For instance, it was shown that some of the initially descending fibers of LIV excitatory neurons also contact LVa neurons at a yet unknown postsynaptic target structure (apical dendrite/basal dendrite?) (FELDMEYER et al., 2005), which has not been described in V1 so far.

In contrast to spiny LIV neurons, Layer II/III pyramidal cell axons also spread horizontally into neighboring barrels while descending to infragranular layers, where they establish synapses onto LV neurons (DE NÓ, 1922; BERNARDO et al., 1990; GOTTLIEB and KELLER, 1997). LII/III neurons are highly interconnected: A single pyramidal cell receives almost as many inputs from other pyramidal cells (~270 (FELDMEYER et al., 2006)) as from LIV spiny neurons (~300-400 (LUBKE et al., 2003)), suggesting a signal amplification mechanism in LII/III by feedback excitation.

Layer V neurons receive LII/III inputs which were initially considered as this layer’s main driver (THOMSON and DEUCHARS, 1997; REYES and SAKMANN, 1999). However, it turned out that these interconnected neurons (FRICK et al., 2008) are targeted by LV and LVI neurons almost homogeneously while LII/III and LIV inputs appear more patchy (SCHUBERT et al., 2001). Projections from LV neurons are different for the two cell types present in this cortical layer – slender tufted pyramidal cells with a slender terminal tuft at the end of its apical dendrite and thick tufted pyramidal cells (LARKMAN and MASON, 1990). Apart from densely projecting to other LV neurons, slender tufted LVa axon collaterals ascend to LII/III broadly spreading throughout barrel field irrespective of barrel column borders (SHEPHERD et al., 2005; OBERLAENDER et al., 2011). Furthermore, LVa neurons project to M1 (MAO et al., 2011) and the contralateral S1 (LARSEN et al., 2007). In contrast to slender tufted pyramidal cells, LVb axons mainly stick to LV (~60 %) (FELDMEYER, 2012) with less than half of the intra-cortical axonal path length (OBERLAENDER et al., 2011). Local pairwise connectivity is relatively high (5-

20 %) (LE BE et al., 2007; LEFORT et al., 2009; FELDMEYER, 2012) and LVb neurons tend to receive some inputs from descending LVa axon – though the reverse does not hold true for ascending LVb collaterals (LEFORT et al., 2009). Long range projections from thick tufted pyramidal cells are found in the thalamic and trigeminal nuclei, the striatum and the superior colliculus (VEINANTE et al., 2000a; LARSEN et al., 2007; BROWN and HESTRIN, 2009).

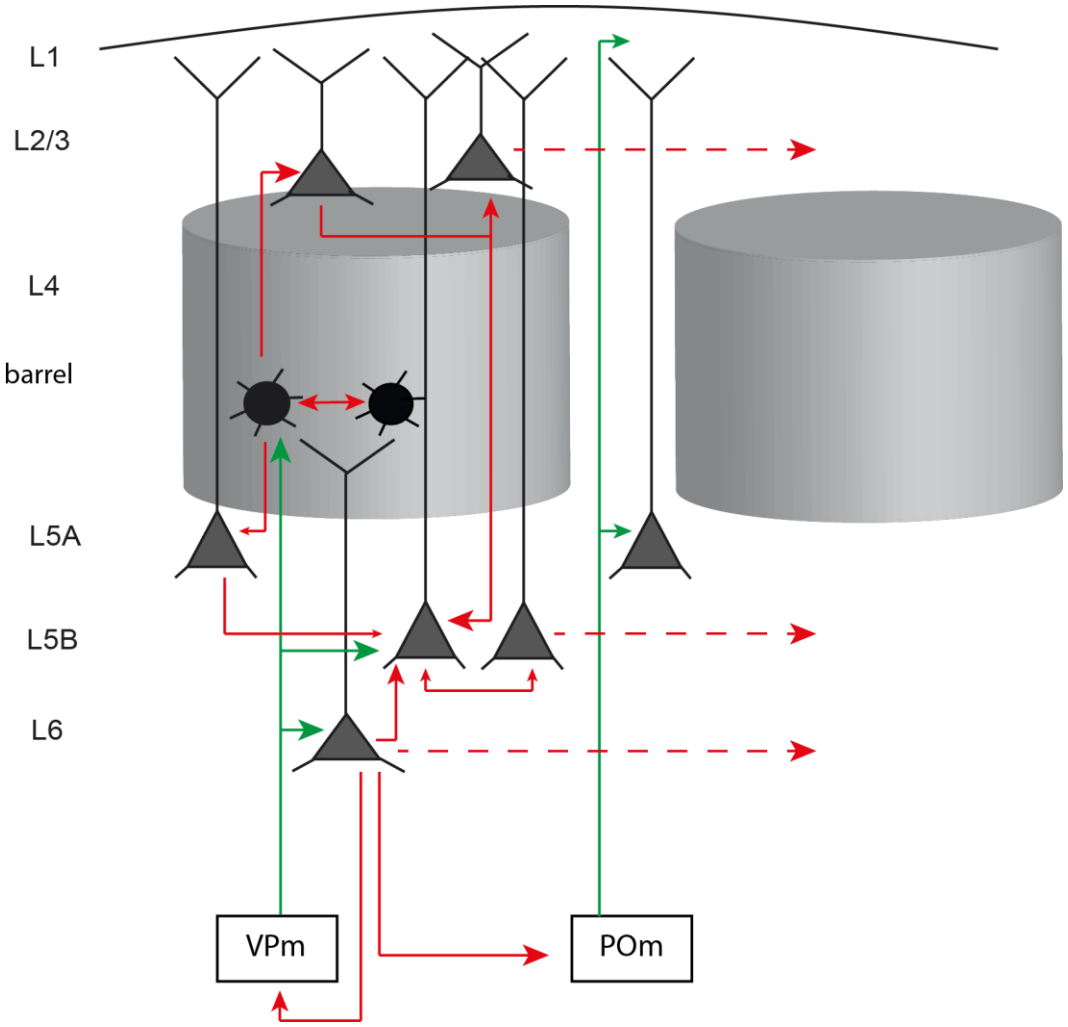

Figure 8: Excitatory intracortical paths: simplified scheme of the canonical microcircuitry. Thalamic inputs in green, excitatory projections in red. Note the LII/III, LV and LVI transcolumnar projections avoided by LIV neurons.

While LV is often referred to as the “cortical output layer”, LVI is considered to be the “cortico-thalamic” layer. About every second neuron in LVI projects to thalamic nuclei (GILBERT and KELLY, 1975; ZHANG and DESCHENES, 1997) with a preference of sublayer LVIa to VPm and LVIb to VPm and POm (ZHANG and DESCHENES, 1997). LVIa cortico-cortical projections reside in infragranular layers LV and LVI with a wide transcolumnar spread over several barrels and some long range collaterals to SII and M1 (ZHANG and DESCHENES, 1997; KUMAR and OHANA, 2008; PICHON et al., 2012).

2.3.3. Inhibitory columnar pathways

Like excitatory cells in LIV, inhibitory neurons also receive thalamic inputs from VPm, which subsequently establish feed-forward inhibitions to spiny LIV neurons (STAIGER et al., 1996; PORTER et al., 2001; BEIERLEIN et al., 2003; DAW et al., 2007). LIV interneurons either vertically project their axons to supragranular layers or reside within LIV (see 2.2.2).

Similar to excitatory LIV to LII/III pathways, LII/III interneurons also receive inputs from spiny LIV neurons implementing a further feed forward inhibition mechanism (HELMSTAEDTER et al., 2008b; XU and CALLAWAY, 2009). This parallel inhibition stream is also maintained in the projection from LII/III to LV: Bipolar LII/III interneurons receive intralaminar input from pyramidal cells and project to LV pyramidal neurons (PORTER et al., 1998; REYES et al., 1998; BAYRAKTAR et al., 2000). Overall, LII/III interneuron projections could be grouped into three categories (HELMSTAEDTER et al., 2009b): 1) local inhibition (within LII/III, mostly ‘barrel column confined”) 2) lateral inhibition (projections to neighboring barrel columns 3) translaminar inhibition (LII/III – LV, LII/III – LI).

Although paired recordings revealed the described parallel nature of inhibitory circuits in granular and supragranular layers, those of infragranular layers remain poorly understood with the exception of the known mediator role of Martinotti cells in LV pyramidal cell inhibition (SILBERBERG and MARKRAM, 2007; FELDMEYER et al., 2013).

3. Cortical feedback mechanisms

Although local top-down connections constitute most projections in a local cortical area, long range projections interconnecting different cortices seem to be functionally significant as well (DOUGLAS and MARTIN, 2007), suggesting that an integration mechanism between feed forward and feedback stream might be at the very fundament of cortical computations (CAULLER, 1995; MEYER, 2011; LARKUM, 2013).

Basic cortical functions like cognition and perception have been found to rely not only on the sensory feed forward stream but also on cortical feedback mechanisms (BULLIER, 2001; PASCUAL-LEONE and WALSH, 2001; SOLTANI and KOCH, 2010; BOLY et al., 2011). Long-range cortico-cortical projections (feedback stream) to S1 tend to terminate in Layer I (ROCKLAND and PANDYA, 1979; CAULLER et al., 1998) targeting interneurons (MARKRAM et al., 2004) and distal tufts of pyramidal cells, constituting the majority of synapses in LI (SHU et al., 2003; DOUGLAS and MARTIN, 2007). How such long-range projections are integrated into sensory feedforward streams resulting in cortical outputs remains unknown yet. LV pyramidal neurons carry several salient subsequently described features, potentially endowing them with the ability to act as such an integration hub (LARKUM, 2013).

3.1. Layer V pyramidal cells

LV is characterized by two major forms of pyramidal neurons appearing spatially separated with different morphological and intrinsic membrane properties. One major morphological difference has been briefly described in chapter 2.3.2.: the variation of their apical dendrites. While both forms of LV pyramidal neurons send an ascending main apical dendrite to LI, they differ in their ascending branching pattern and their termination morphology: slender tufted LVa pyramidal cells lack dendritic branching except for a few apical oblique dendrites before forming a slender apical tuft within LI. In contrast, LVb pyramidal cells branch within LII/III until they form a thick apical tuft in LI (LARKMAN and MASON, 1990; LARKMAN, 1991a).

When injected with somatic currents LV pyramidal neurons display different forms of spiking mechanisms: Intrinsic burst (IB) neurons respond with short, high frequency, repetitive bursts separated by hyperpolarizations, while regular

spiking neurons (RS) fire single long-lasting spikes (CONNORS et al., 1982; MCCORMICK et al., 1985; CONNORS and GUTNICK, 1990). It is important to point out that the bursts evoked in IB neurons correspond to their intrinsic membrane properties and not to the quality of the stimulus (in principle every neuron could fire bursts) (CONNORS and GUTNICK, 1990). Initially described in guinea pig cortex, IB neurons were found primarily in LIV and LVa (CONNORS et al., 1982; MCCORMICK et al., 1985). Yet in mouse (AGMON and CONNORS, 1989) and rat (CHAGNAC-AMITAI and CONNORS, 1989), IB neurons appear exclusively in sublayer LVb. Their somata seem relatively larger compared to RS neurons in LVb and their axons seem to reside within LV spreading mostly horizontally (with some exceptions: (STAIGER et al., 2016)) while in contrast, RS axon collaterals also ascend to supragranular layers mostly reaching LI and also spreading across columns (CHAGNAC-AMITAI et al., 1990).

3.2. Action potential initiation zones of LV pyramidal cells

A major finding around the question of how LV pyramidal neurons might integrate cortical feedback at the distal apical tuft was the discovery of a second action potential initiation zone (AMITAI et al., 1993; YUSTE et al., 1994; SCHILLER et al., 1997; STUART et al., 1997a). This calcium spike initiation zone is located in very close proximity to long range projections at the distal apical tuft in contrast to the axonal initiation zone. Distal dendritic current injections lead to long, plateau-type regenerative dendritic potentials causing high frequency bursts in the axonal initiation zone (KIM and CONNORS, 1993; WILLIAMS and STUART, 1999; LARKUM et al., 2001; LARKUM, 2013). Action potentials in the axonal initiation zone in turn have been shown to result in backpropagation to dendritic trees, obviously changing their membrane potential (FATT, 1957; STUART et al., 1997b). Although these back-propagating single Na^+ action potentials could not evoke a Ca^{2+} spike in the apical dendritic tuft (KIM and CONNORS, 1993; STUART and SAKMANN, 1994; SCHILLER et al., 1997), the interaction of these potentials (subsequently described in 3.3.) might be at the basis of signal integration.

3.3. Coincidence detection

While single distal apical tuft inputs appear mostly subthreshold to evoke calcium spikes (WILLIAMS and STUART, 2002; LARKUM et al., 2009), the combined occurrence of a back-propagating AP together with a subthreshold EPSP at the distal apical dendrite has been shown to trigger Ca^{2+} spikes, leading to multiple APs (2-3) in the axonal initiation zone (bursts) (LARKUM et al., 1999) (Fig.9). These back-propagating action potential evoked Ca^{2+} spikes (BAC) could be triggered with only half (or even 25% e.g. in the neuron shown in Fig.9) the current necessary to evoke such spikes at the distal apical dendrite without a back-propagating AP.

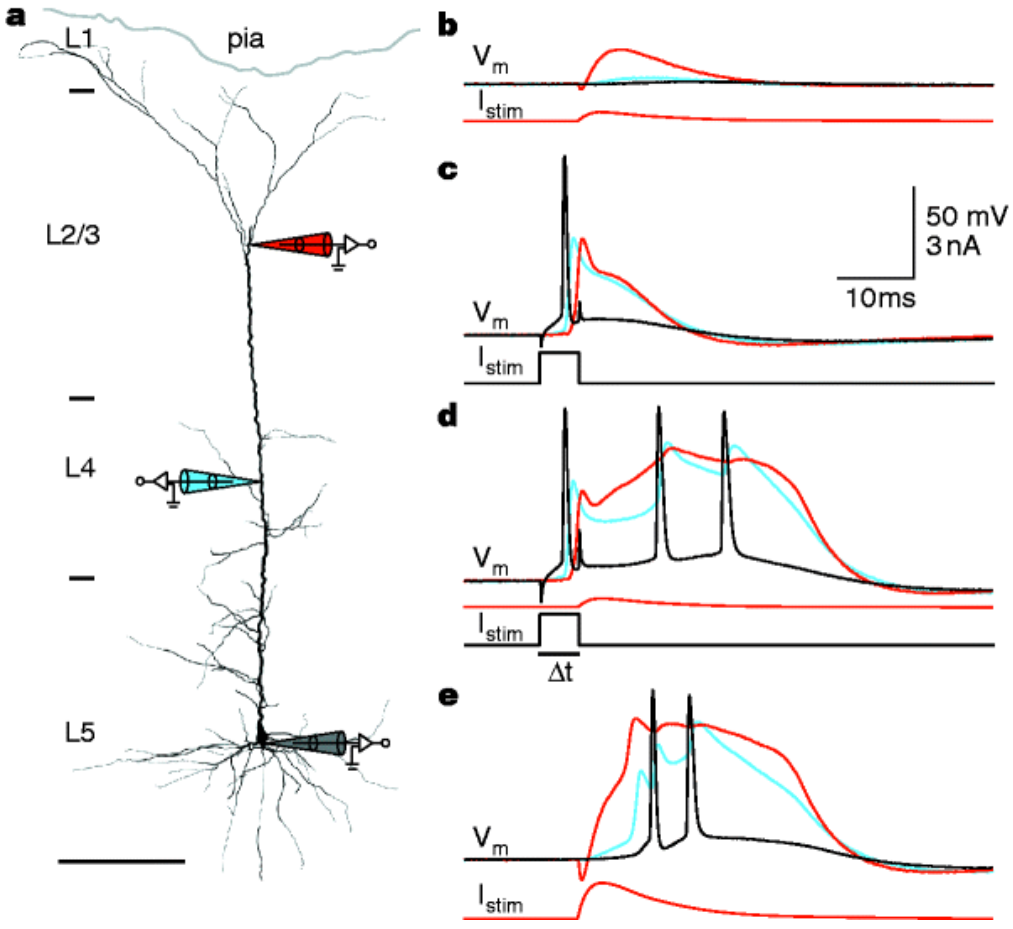

Figure 9: Coincidence detection. (a) Triple recording of a LV pyramidal neuron. (b) 0.3nA current injection at the distal pipette, no AP evoked in the soma. (c) Threshold current injection at the soma evokes AP in the dendrite. (d) Combination of the currents in (b) and (c) evoked Ca^{2+} spikes leading to AP bursts. (e) 1.2 nA current injection at the distal pipette evokes similar Ca^{2+} spikes resulting in AP bursts.

From: (LARKUM et al., 1999), reprinted with permission of the Nature Publishing Group

This salient mechanism potentially empowers LV pyramidal neurons to act as an integration hub, processing information of cortical feedforward streams and long range cortical feedback (LARKUM, 2013): BAC firing allows massive amplification of feed forward inputs at the soma compartment by relatively weak apical tuft stimuli (LARKUM et al., 2004). Thus, external sensory information e.g. could be associated with feedback information tuning the neuron's firing pattern accordingly.

Coupling (=relative threshold reduction for Ca^{2+} spikes) (SCHAEFER et al., 2003) of these active zone compartments can be abolished by inhibition in the intermediate apical dendrite zone (Fig. 9, a, cyan pipette). Unitary IPSPs could suppress BAC firing but not the back-propagating AP itself in vitro (LARKUM et al., 1999) and in vivo (PALMER et al., 2012). Hence, BAC firing is also suppressed during anesthesia (POTEZ and LARKUM, 2008).

Morphological alternations in this intermediate compartment have been shown to influence coupling: the fraction of proximal oblique dendrites positively correlates with coupling (=the more proximal oblique dendrites the lower the threshold for Ca^{2+} spikes in the distal tuft) (Fig. 10). On the other hand, larger fractions of distal oblique dendrites have a negative effect on coupling (SCHAEFER et al., 2003).

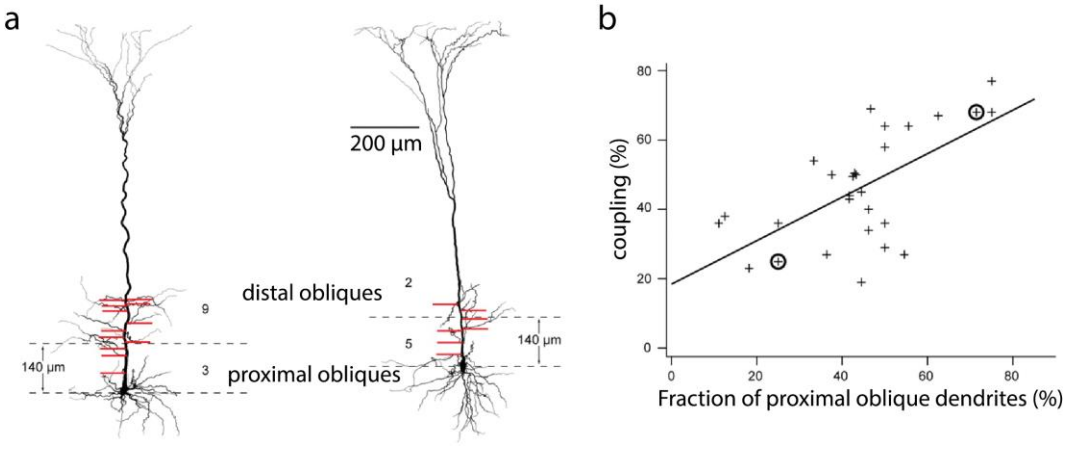

Figure 10: Coupling correlation with apical oblique dendrites. (a) Two LV pyramidal neurons with different apical oblique dendrite configuration. (b) Positive correlation of proximal apical oblique dendrites with coupling, circles indicate neurons depicted in (a).

From: (SCHAEFER et al., 2003), reprinted with permission of the American Physiological Society

The underlying mechanisms are currently interpreted as the following: 1.) While additional distal oblique dendrites increase the capacitive load for the back-propagating action potential, proximal oblique dendrites are pre-charged by current injection/stimulus. 2.) The initial threshold for somatic/axonal AP initiation is increased by proximal oblique dendrites. The additional charges present in the back-propagating APs increase coupling.

In this context, it is important to point out the existence of a LVb pyramidal neuron subtype, which is characterized by multiple apical oblique dendrites in LIV (> 4 apical obliques, > 1 mm dendritic path length in LIV) (Fig.11), considered to potentially collect additional VPm inputs (MEYER et al., 2010a).

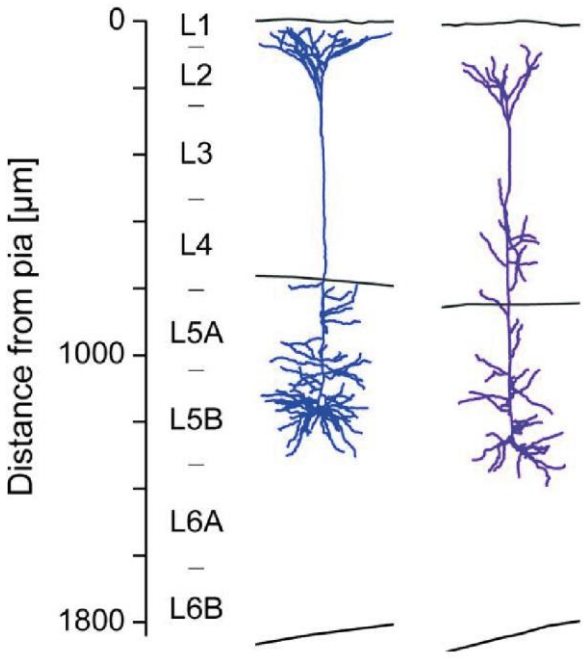

Figure 11: LVb pyramidal neuron subtype. "Regular" LVb pyramidal neuron in blue, LVb subtype with additional apical oblique dendrites in LIV in purple.

From: (MEYER et al., 2010a), reprinted with permission of the Oxford University Press

4. Wiring rules

One cubic millimeter of mouse brain tissue contains around four km of axons forming ~one billion synapses (BRAITENBERG and SCHÜZ, 1998; MERCHAN-PEREZ et al., 2014; STAFFLER et al., 2017). However, whether the organizing principle of these connections is based on randomness or on highly specified connections still remains unsolved.

4.1. Peters' rule

One hypothesis addressing this question is commonly known as "Peters' rule": It assumes synapses to form by chance in correlation with the spatial overlap occurrences between two given pre- and postsynaptic structures (PETERS and FELDMAN, 1976; PETERS and PAYNE, 1993; BRAITENBERG and SCHÜZ, 1998). In this sense the number of synapses formed by an axon on a given postsynaptic structure (e.g. axon initial segment, soma, dendritic shaft) could be predicted by the fractional availability of the respective target in apposition to the axonal tree. Stated in mathematical terms, connection strength between two given neurons correlates with the product of densities of axonal boutons and dendrites (BINZEGGER et al., 2004; SHEPHERD et al., 2005). Synaptic strength on a single synaptic level is considered homogeneously, also referred to as "function follows form".

$$\int_{volume} Psynapse(x,y,z)\ \alpha \int_{volume} D_{axon}(x,y,z) * \int_{volume} D_{dendrite}(x,y,z)$$

Equation 1: Simple form of Peters' rule. P=synapse probability, D=wiring densities.

Although geometrical proximity is obviously required for synapse formation, it is most certainly not the only predictor. In addition to highly specific synapse formation (discussed in 4.2.), it has been also shown that laminar and columnar positions of pre- and postsynaptic neurons influence connection strength, indicating location dependent circuit organization (SHEPHERD et al., 2005).

4.2. Wiring specificities

There are numerous examples of axonal wiring making exceptions to Peters' rule if not completely contradicting the circuit principle. The antitheses to Peters' rule would assume cortical connectivity to be driven rather by highly specific wiring principles over proximity clusters. One of such axonal wiring specificities is most commonly known in LII/III Chandelier cells (SOMOGYI, 1977). In fact, these neurons display wiring specificities on two postsynaptic features fundamental for their synapse formation: a) their primary postsynaptic target structure is an axon initial segment b) their primary postsynaptic target neuron is a pyramidal cell (SOMOGYI et al., 1982). A similar structural target specificity has been shown for basket cells preferentially targeting somata (JONES, 1984). Further, non-random circuits have been described for thalamo-cortical projections in V1 (REID and ALONSO, 1995) and S1 (WHITE and HERSCH, 1982; BENSHALOM and WHITE, 1986) as well as for cortico-thalamic (WHITE and KELLER, 1987) and retinal projections (BRIGGMAN et al., 2011).

These studies could be considered as direct contradictions to random wiring principles hypothesized by Peters' rule, implicating the complexity of circuit organization beyond geometrical motives. Although wiring diagrams for local or global circuits are very challenging and expensive, they may be crucial to fully understand the brain's circuits' wiring principles and hence its function.

III. MATERIALS AND METHODS

All animal experiments were carried out at the Max-Planck-Institute of Neurobiology, Martinsried. The dataset was acquired at the Max-Planck-Institute for medical research, Heidelberg.

1. Sample preparation

A 28-days-old wild type male mouse (C57BL/6N) was anesthetized and sacrificed by transcardial perfusion of cacodylate buffer and fixative. All experiments were carried out in accordance with the laws of animal experimentation issued by the German federal government and were approved by the local animal care and use committee (GZ: 55.2-1-54-2532.3-103-12, Regierung von Oberbayern).

1.1. Transcardial perfusion

The animal was placed in a box connected to an isoflurane vaporizer and was anesthetized with a 3% isoflurane (Baxter, Deerfield, USA) oxygen mixture (Fig. 12, a). As soon as the mouse had reached the surgical plane of anesthesia, it was subsequently placed on a custom built surgery stage which allowed maintaining Isoflurane inhalation. Anesthesia levels were controlled by checking the flexor reflexes and deep pain perception by compressing the paws and the tail with a forceps.

Once the reflexes were gone and the surgical plane of anesthesia assured, surgery was initiated with a ~3 mm long caudo-cranial incision through the integument and abdominal wall beneath the thorax. Next, the diaphragm was carefully ruptured with scissors and laterally cut along the rib cage in order to expose the pleural cavity (Fig 12, b). In order to properly access the heart, the sternum was lifted away with a hemostat and placed overhead. Small scissors were used to incise the right atrium, and a 21 G blunt end needle (B. Braun, Melsungen, Germany) was immediately placed into the left ventricle (Fig. 12, c).

The mouse was subsequently perfused (Harvard apparatus, Holliston, USA) with 15 ml cacodylate (Serva, Heidelberg, Germany) buffer (0.15 M, pH 7.4) followed by 25 ml fixative mixture containing 0.08 M cacodylate (pH 7.4), 2.5% paraformaldehyde (Sigma-Aldrich, St Louis, USA), 1.25% glutaraldehyde (Serva) and 2 mM calcium chloride (Sigma-Aldrich). The animal was then decapitated

and a ~5 mm caudo-rostral incision was made along the sagittal suture, stopping close before bregma (Fig. 12, d). After laterally flipping the skull bones in order to allow better immersion fixation, the skull with the exposed brain was placed in 50 mL Falcon tubes (Sigma-Aldrich, St.Louis, USA), containing the previously described fixative mixture and subsequently immersed overnight (at least 12h) at 4°C .

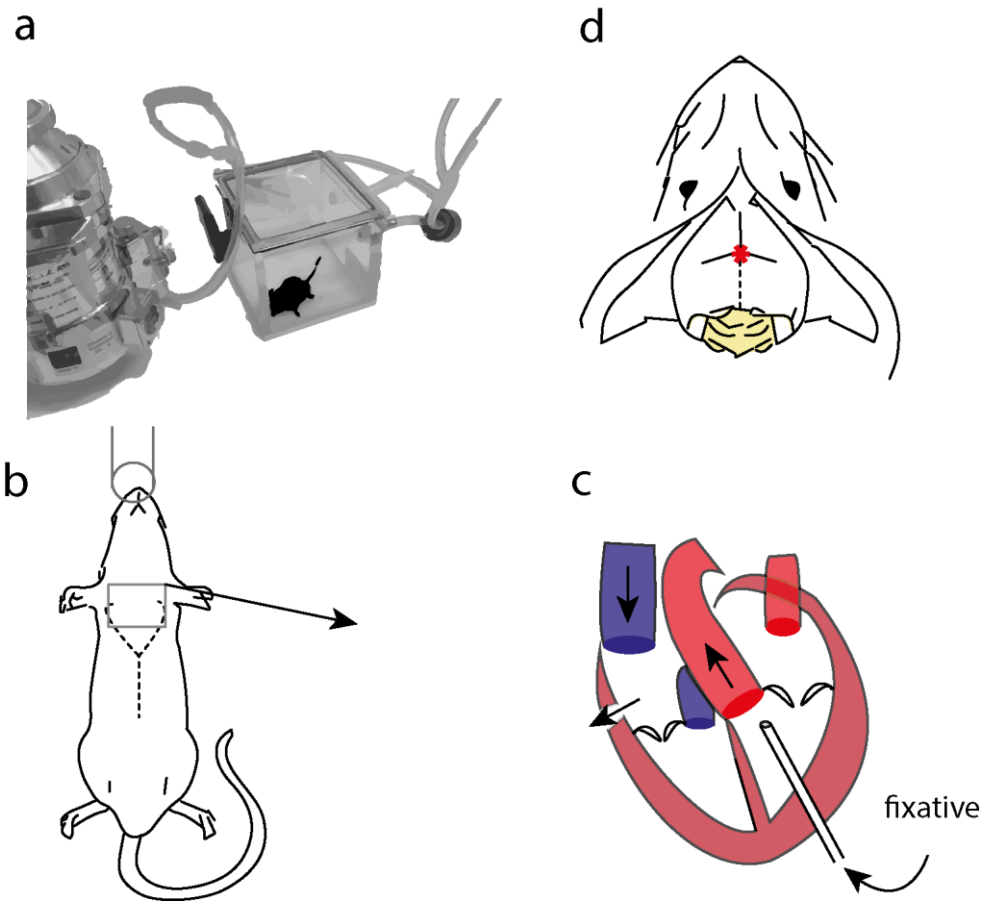

Figure 12: Transcardial perfusion scheme. (a) Mouse is anesthetized in an anesthesia box until surgical plane is reached. (b) Abdominal and thoracical incisions to access the heart, in order to perfuse the animal as depicted in (c)(arrows indicating fixative's flow direction). (d) After decapitation, a sagittal incision towards bregma (indicated as red asterisk) is performed and the skull bones are flipped aside.

1.2. Biopsy punching

The next day, the perfusion and immersion fixed mouse head was taken out of the Falcon tubes and glued (Locite 401, Henkel, Düsseldorf) on the inner side of a falcon tube lid. The lid was then placed in a stereotax (Kopf instruments, Tujunga, USA) and the setup was adjusted with a stereomicroscope (Leica microsystems,

Wetzlar, Germany) such that the biopsy device was orthogonal to the sagittal suture of the skull.

The used biopsy device was a custom modified rotating device driving a 1 mm diameter wide punch, designed for skin biopsies (KAI medical, Honolulu, USA), to maximally preserve the tissue's ultrastructure.

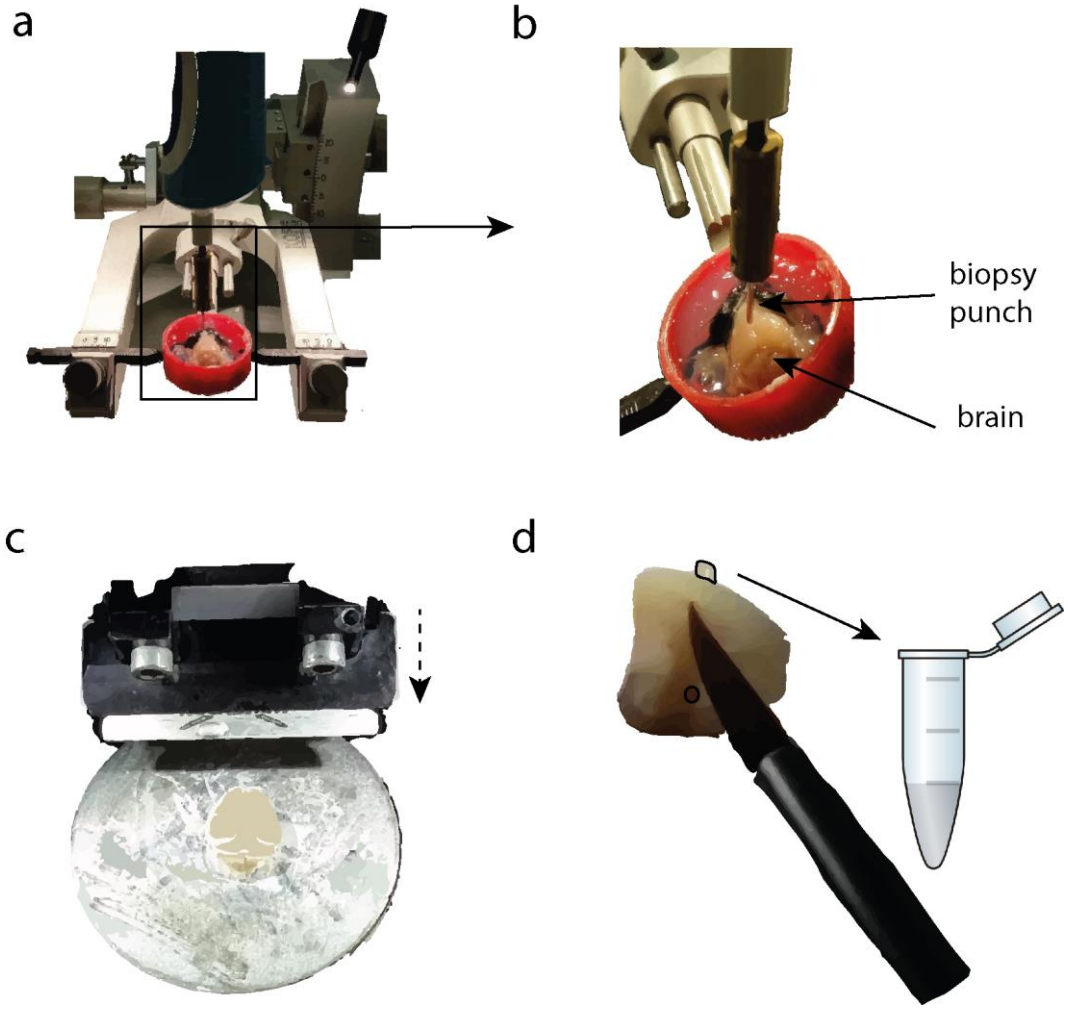

Figure 13: Stereotactic barrel field targeting & biopsy extraction. (a) Agarose fixed mouse head in a stereotax setup. (b) Custom built punching device to obtain EM samples with minimal mechanical damage. (c) Whole brain on a microtome stage (arrow indicates cutting direction). (d) 1 mm sample extraction with a brush (sample and punching location on the other hemisphere highlighted).

First, bregma was detected and approached with the biopsy punching device (Fig.13, a). In order to target S1 barrel cortex, the device was driven 2 mm in rostro-caudal direction and 2.8 mm in medio-lateral direction (coordinates based on prior personal experiments and observations). It was then carefully drilled 2 mm into the cortex tilted by thirty degrees in order to maintain the cortical axis

with a step size ~100 µm/second to avoid mechanical damage (Fig.13, b). After carefully retracting the punching device, the targeting procedure was repeated on the remaining hemisphere. As this procedure lacks any ventral sagittal incision, the hereby stamped biopsies remained within cortex and needed to be extracted subsequently. To obtain brain biopsies for high resolution EM, it is crucial to minimize any mechanically induced tissue damage, which required great care in all steps involved in the procedure. After the biopsies have been stamped in the stereotactic frame, all the remaining lateral parts of the skull were removed and the whole brain was carefully extracted with a sub-cranially moved spatula into a beaker containing cacodylate buffer (0.15 M, pH 7.4).

In the next step, the whole brain was ventro-dorsally glued on a vibratome stage (Leica microsystems) and a razor blade (Wilkinson sword, Chesterfield, USA) was carefully approached towards the pia mater (step size ~100µm) (Fig.13, c). A subsequent 1.5 mm thick section comprised a section spanning the entire cortical depth including the previously punched biopsies. The obtained section was flipped on the dorsal side (pia mater) allowing visualization of the sharp biopsy punch outlines with bare eyes. Finally a tiny brush (Zahn Pinsel, Bechhofen, Germany) was used to extract the biopsies by applying gentle pressure from the ventral side of the section (Fig. 13, d). The samples (1 mm diameter, ~1.0 – 1.5 mm length) were then transferred into Eppendorf tubes containing 2 mL of cacodylate buffer (0.15 M, pH 7.4) and stored at 4° C overnight (at least 6 hours). The remaining cortical slice was transferred into a 15 mL Falcon tube (Sigma-Aldrich) containing Dulbecco's Phosphate Buffered Saline (PBS) without Ca^{2+} & Mg^{2+} (Biochrom, Berlin, Germany) and kept at 4 °C overnight for Cytochrome C staining the next day.

1.3. Cytochrome C staining

In order to determine the exact barrel field location of the obtained biopsy punches, the remaining cortical slice was sectioned and subsequently counterstained. This slice was manually cut into half along the sagittal suture with a razor-blade (Wilkinson) (Fig.14, a) and the hemispheres were subsequently glued on a vibratome stage pooled in PBS with the pia mater towards the stage (Fig.14, b). 100 µm thick tangential sections were collected and stored in a well plate (Corning, Inc., Corning, USA) containing PBS. After double rinses with fresh PBS for one hour each, the buffer was replaced by a cytochrome C staining

solution made of 2 % Catalase, 0.1 % cytochrome C and 0.05 % Diaminobenzidine (DAB) (all Sigma-Aldrich) buffered in 0.1 M PBS (Fig. 14, c). The slices were subsequently immersed overnight at room temperature.

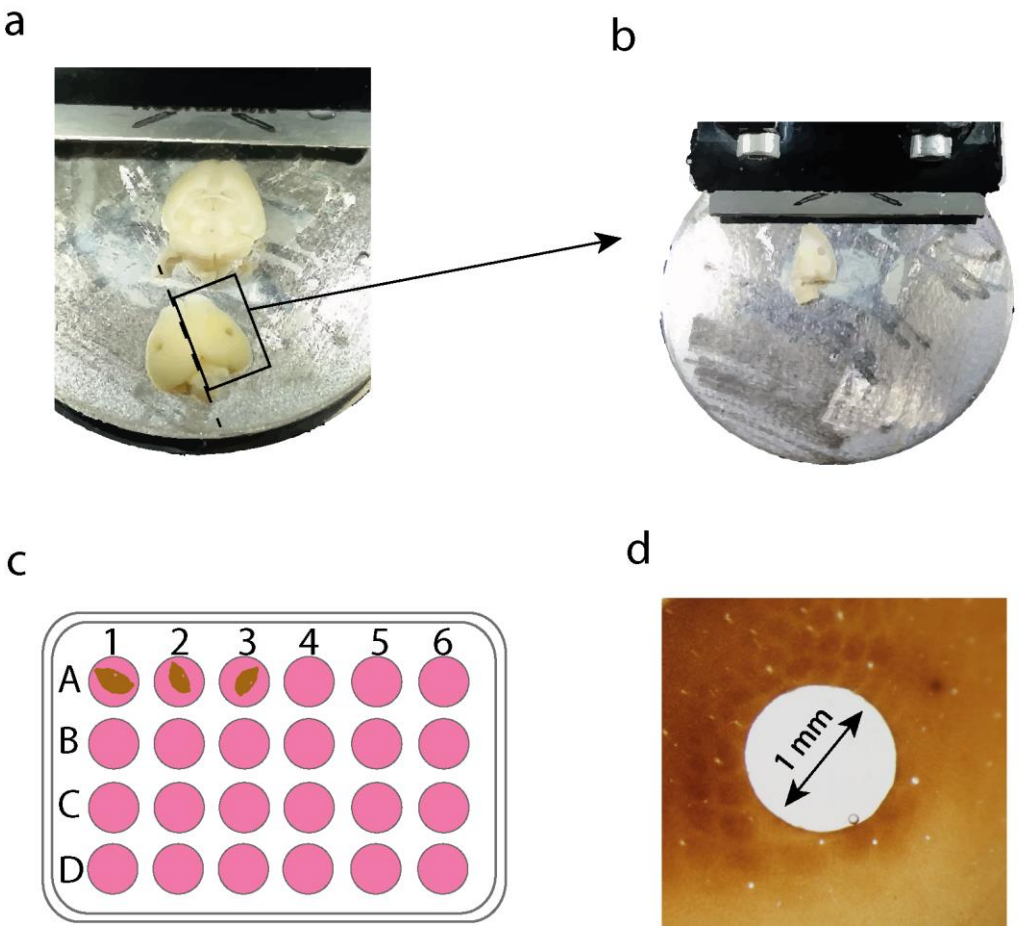

Figure 14: Cytochrome C counterstaining: (a) Remaining cortical section is cut into half, glued on a vibratome stage and subsequently sliced. (b) 100 µm slices obtained, collected and cytochrome C stained in well plates (c) (exemplary slices shown). (d) Cytochrome C counterstain of the obtained sample, 1 mm wide whole indicates biopsy punch location.

1.4. EM-staining

The samples obtained as previously described were then en-bloc stained following the protocol developed in the Helmstaedter laboratory (HUA et al., 2015). Initially the samples were transferred into fresh Eppendorf tubes containing 2% OsO_4 (Serva) buffered with cacodylate (0.15 M, pH 7.4). After 90 minutes incubation at room temperature, the samples were then transferred into Eppendorf tubes containing 2.5 % ferrocyanide in 0.15 M cacodylate buffer (pH 7.4) and incubated for 90 minutes at room temperature as well. The samples were then rinsed in nanopure filtered water twice for 30 minutes at room temperature and subsequently immersed with TCH (Sigma-Aldrich). After 45 minutes incubation

at 40 °C and two washing steps with nanopure filtered water, the tissue was stained with unbuffered 2% OsO_4 aqueous solution for another 90 minutes at room temperature. Once again, the tissue was rinsed in filtered nanopure water twice for 30 minutes and afterwards immersed in 1% Uranyl-Acetate (UA) (Serva) aqueous solution at 4 °C overnight. On the next day, the samples were incubated for another two hours at 50 °C. Subsequent rinsing in nanopure filtered water was followed by two hours immersion at 50 °C in a lead aspartate solution (pH 5.0) containing 0.066 % lead nitrate (Sigma-Aldrich) per mL 0.03 M aspartic acid buffer (Serva). (Fig. 15, a)

1.5. Sample embedding

After two final rinses in nanopure filtered water for 30 min, the samples were dehydrated in a graded series of ethanol (50, 75, 100 %, 30 minutes each, at 4 °C) followed by incubation in 100 % acetone thrice, 30 minutes each. Subsequently, the tissue was infiltrated in an open Eppendorf tube containing a 1:1 mixture of Spurr's resin (4.1 g ERL 4221, 0.95 g DER 736 and 5.9 g NSA; Sigma-Aldrich) and acetone overnight on a rotator.

The next day, samples were incubated in pure Spurr resin containing 1 % DMAE for 6 hours in closed Eppendorf tubes. Finally the samples were transferred in embedding molds (Polyscience, Eppelheim, Germany) and placed in an oven at 70 °C for three days. (Fig. 15, b)

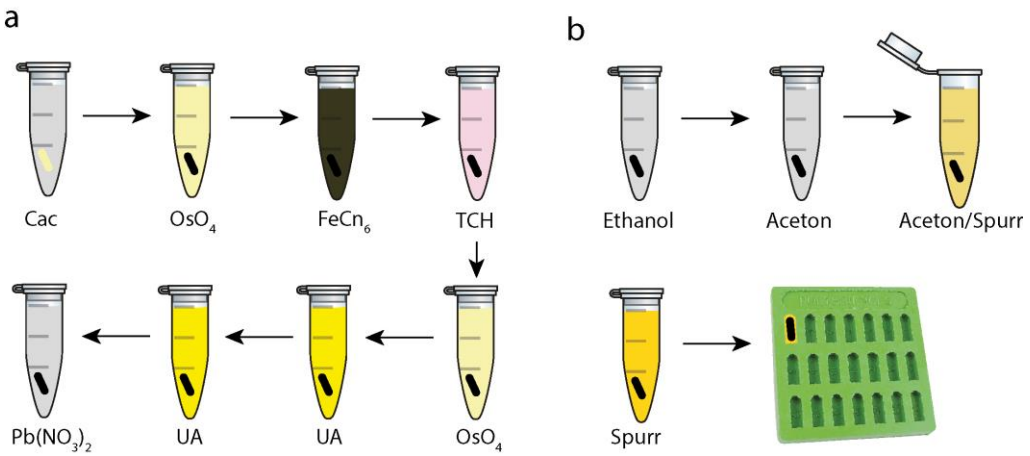

Figure 15: Staining and embedding. (a) Staining sequence, indicating sample and chemical color after each incubation. Rinses with nanopure filtered water after OsO_4, Ferrocyanide, TCH, UA, and lead aspartate step not shown. (b) Dehydration and embedding.

1.6. Sample trimming and screening

In order to prepare the obtained samples for the SBEM setup (courtesy of W. Denk, MPI of neurobiology, Munich), the cured sample block was first trimmed with a EM-Trim2 (Leica Microsystems) (Fig. 16, a) and the sample was subsequently extracted from the resin block in order to mount it on an aluminium pin suitable for the setup (Fig. 16, b). As soma densities and soma sizes on overview EM images allowed cortical layer detection and therefore field of view determination, the sample was mounted with the pia mater orthogonal to the aluminium pin's surface using electrically conductive epoxy (Henkel). The sample's surface was polished with a diamond knife (Diatome, Biel, Switzerland) mounted in a UC7 (Leica Microsystems).

Subsequently, the sample was imaged in a field emission gun scanning electron microscope Quanta FEG200 (FEI company, Hillsboro, OR, USA) to control the staining quality. The sample was scanned with an electron beam at a pixel dwell time of 3.2 µs with a spot size of 2.9 and an energy of 2.8 keV. For overview images (Fig. 16, d) the pixel size was 720 nm x 720 nm, for high resolution images 6.0 nm x 6.0 nm or 12.1 nm x 12.1 nm, respectively. A custom designed detector (AXUV, International Radiation Detectors) in combination with a custom-built current amplifier (courtesy of W. Denk, MPI of neurobiology, Munich) was used to detect backscattered electrons (BSE).

The sample of choice (scPL115) displayed good membrane integrity and contrast and was sufficiently good for synapse identification (Fig. 17, b, c).

Once the field of view (Fig. 16, d) was determined, the sample was trimmed down to facilitate cutting in the SBEM setup (Fig. 16, e, f).

As the sample gets exposed to high electron doses for SBEM dataset acquisition, the sample was coated with a 200 nm thin gold layer with a sputter coater (Leica Microsystems) providing sufficient electrical conductivity (Fig. 16, e).

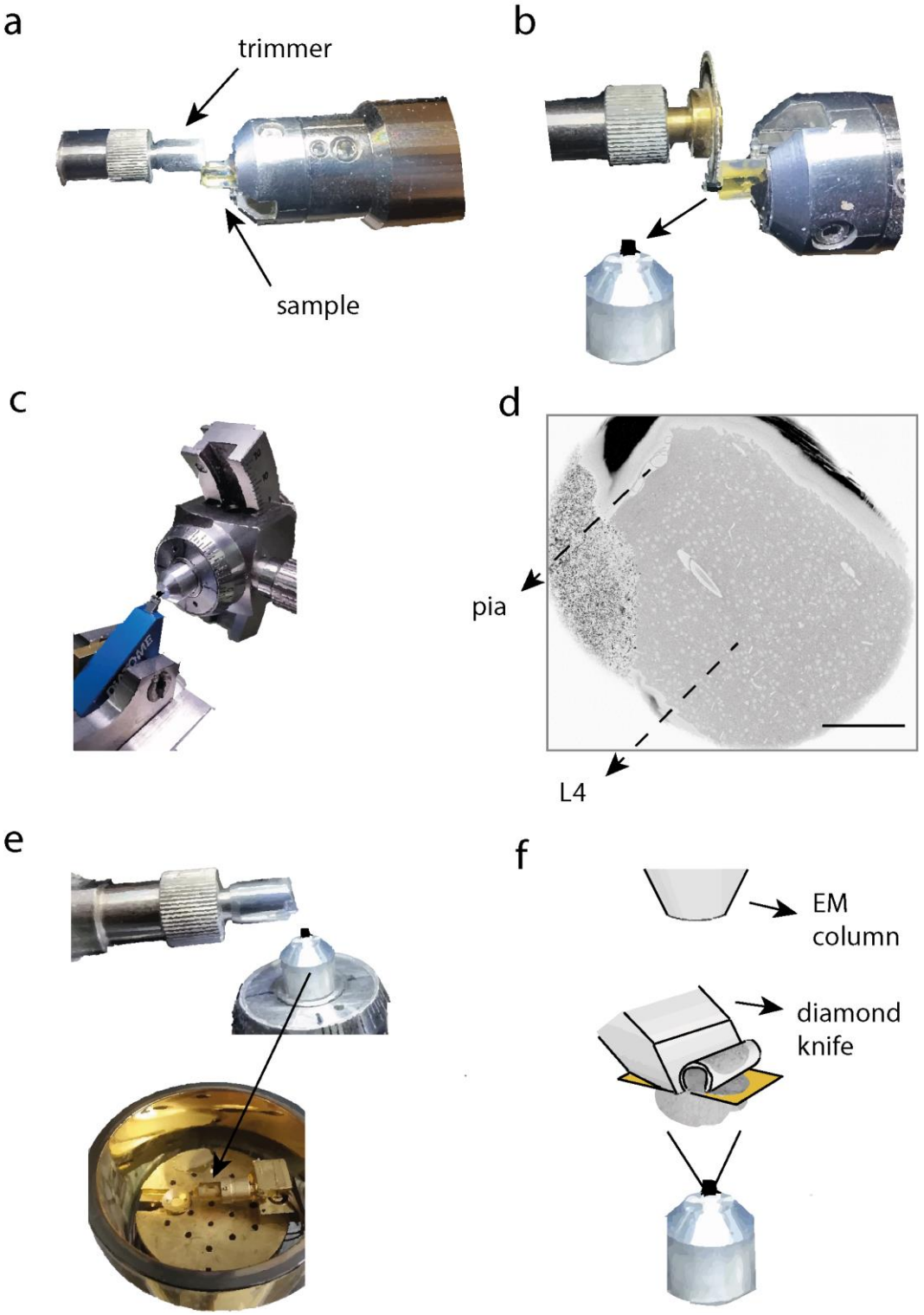

Figure 16: Sample trimming and screening: (a) Sample gets trimmed down to smaller block-face and extracted from Resin block (b). (c) Surface gets smoothed in order to obtain overview EM images as in (d) (scale bar = 250 µm). (e) Sample gets retrimmed and gold coated for SBEM setup (f).

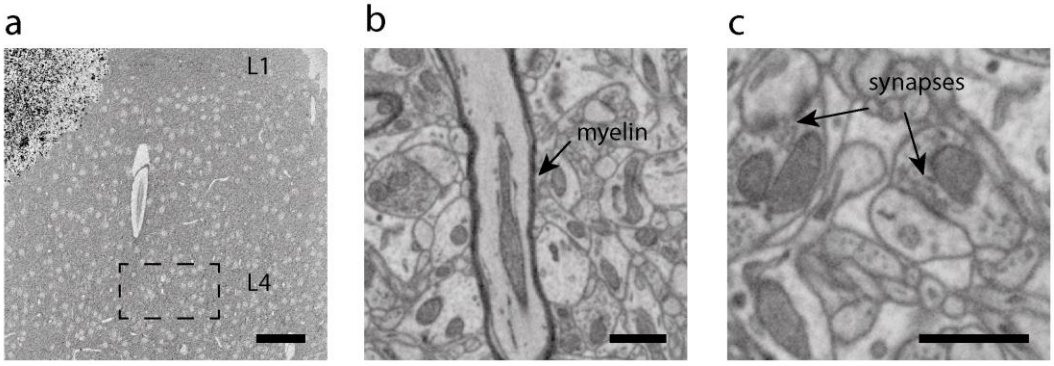

Figure 17: Sample screening scPL115. (a) Overview, screening area and cortical layers indicated, scale bar 100 µm. (b) High resolution image from L4, pixel size 12,1 x 12,1 nm, scale bar 1 µm. (c) High resolution image from L4, pixel size 6,0 x 6,0 nm, scale bar 1 µm.

1.7. Sample approaching

The cutter motor (Physik Instrumente, Karlsruhe, Germany) and the cutter piezo (Physik Instrumente) were moved to the backwards position (maximal relative distance from the knife to the sample). Then the sample was placed into the microtome's sample holder. While the z-motor's position was monitored with a mirror, the z-motor was moved backwards until the range was sufficient to move the motor at least 700 µm forward. Then the sample was further lowered by turning the z-screw of the sample holder anti-clockwise until the sample was substantially lower than the knife. Subsequently, the cutter motor and cutter piezo were moved in forward position.

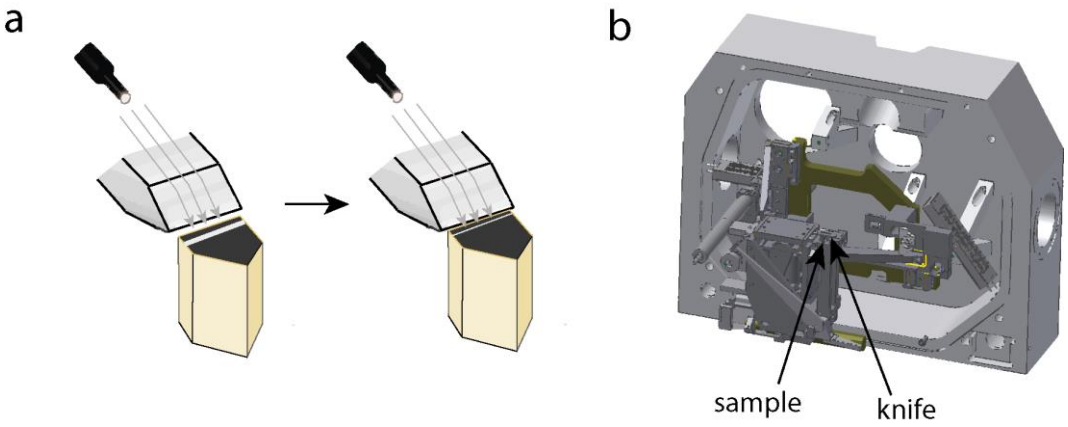

Figure 18: SBEM sample approaching. (a) Approaching sample with diamond knife, light reflections help estimating the distance. (b) Custom designed microtome fitting into a Magellan scanning electron microscope (FEI company).

While monitoring the relative distance between sample and knife by estimating the width of the light bar reflected by the diamond knife with a stereomicroscope (Leica Microsystems) attached to the microscope chamber, the sample was approached first with coarse 10 µm z-motor steps and then with 100 nm step size cutting cycles (Fig.18, a).

As soon as the diamond knife was cutting the entire block-face, the microscope chamber was closed and pumped overnight (at least 8 hours) until a sufficiently stable vacuum ($<10^{-5}$ mbar) and temperature (20 °C, oscillations < 0.1 °C) were reached.

2. Data acquisition

Acquiring 3D SBEM datasets is associated with certain challenges that need to be properly faced. Data quality needs to be focused and maintained over usually several dozen days. Moreover, data acquisition time could easily explode for large scale projects making them unfeasible if not reduced by customization and improvement of SBEM setups. Total acquisition time of a SBEM dataset depends on four factors: a) EM scanning time b) cutting time c) movement time d) cool down time. Although the latter effect is almost invariant, recent developments (Boergens et al, unpublished), substantially decreased factor a) and c).

2.1. Continuous imaging

The dataset stPL115 was acquired with a Magellan scanning electron microscope (FEI company) and a SBEM microtome (DENK and HORSTMANN, 2004) advanced with two piezo actors (P-602, Physik Instrumente) for high precision linear xy movements (imaging plane) (Boergens et al, unpublished).

As the field of view provided by the EM is less than 100 µm, the microtome's motors (M-230, Physik Instrumente) were used to execute larger stage movements in order to tile the field of view into four overlapping regions (motortiles), spanning 217 µm in x and 216 µm in y (Fig. 19, a). Stage movements within each motortile were performed by using the xy piezo actors. Instead of alternating imaging (beam on) with motor movements (beam off), the electron beam was continuously switched on, while the y-piezo accelerated the stage to 34,2 µm/s. After each linear stroke (piezo column), the x piezo shifted the stage by 31,4 µm (1.08 seconds pause) and the y-piezo was subsequently accelerated in the opposite

direction, resulting in 7 piezo columns with 10 images (2048 x 3072 pixel) each (Fig. 19, b). Neighboring piezo column overlap was set to about 9 % in x direction. Acquisition of 70 images per motortile was alternated by large xy movements with the geared motors, followed by continuous image acquisition of the subsequent motortile. Motortile overlap was set to about 5.5 µm in x and about 8 µm in y, in order to maintain continuity throughout the field of view. (Boergens et al., unpublished).

A current of 3.2 nA, a landing energy of 2.8 keV and a dwell time of 100 ns (~16 electrons/nm²) were applied, the effective data acquisition speed was 5.9 MVx/s (including all movements). Backscattered electrons were detected with a commercial CBS detector (FEI company) and amplified with a customized amplifier (Jürgen Tritthardt and Winfried Denk)

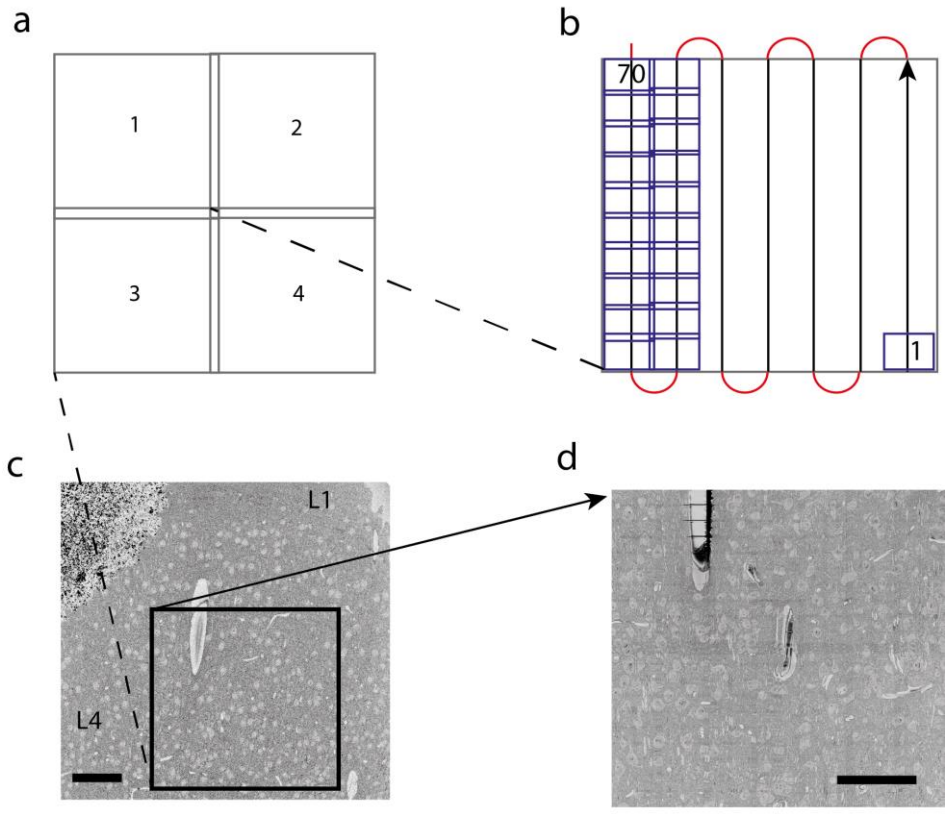

Figure 19: Continuous imaging and field of view. (a) Field of view divided into four motortiles, 217 x 216 µm each. (b) Continuous imaging mode, exemplary for motortile two (x piezo movements in red, y piezo movements in black, acquired exemplary images in green). (c) Field of view in low resolution acquired while screening the sample. (d) Field of view stitched with downsampled images from stPL115 (several approaching sections between c and d), scale bars 100 µm.

The field of view was centered on L4 based on soma sizes, soma densities and distance to pia mater on low resolution images (Fig. 19, c). 2815 consecutive planes were imaged, each altered with a 30 nm cut in between, resulting in a dataset sized 424 µm x 428 µm x 84.45 µm.

2.2. Stack monitoring

Maintaining constant data flow with sufficient quality to trace even the smallest axons and spine necks is one of the major challenges of taking 3D SBEM datasets. Focus and astigmatism instabilities could easily destroy continuity within a stack and have to be managed thoroughly. The most likely cause for those image aberrations are debris particles accumulating around the sample and micro debris contaminating either the detector or even the electron column. Moreover, inhomogeneous cutting or total lack of cutting leads to multiple electron exposure of the sample surface, which entails charging. Custom-written autofocus and astigmatism scripts were used to monitor and compensate for image aberrations. In order to judge the acquired data quality, small subsets of images from each motortile were stitched in order to check axon traceability every day.

2.2.1. Electron column protection

As previous experiments (Schmidt, personal communication) had encountered issues with micro debris contaminating the electron column, a device minimizing the physical opening of the electron column to prevent contaminations was developed and tested for the first time (Thomas Olstinski, Meike Schurr et al.). The device (“detector cap”) was a small piece of Titanium fitting underneath the CBS detector narrowing the pole piece for circulating debris particles. (Fig. 20, a-c)

First, a detector cap with an opening of 500 µm was tested. When this turned out to be too small and caused interactions with the electron beam (Fig. 20, d), a 1000 µm wide detector cap was tested instead which caused neither image aberrations and appeared to prevent electron column contaminations.

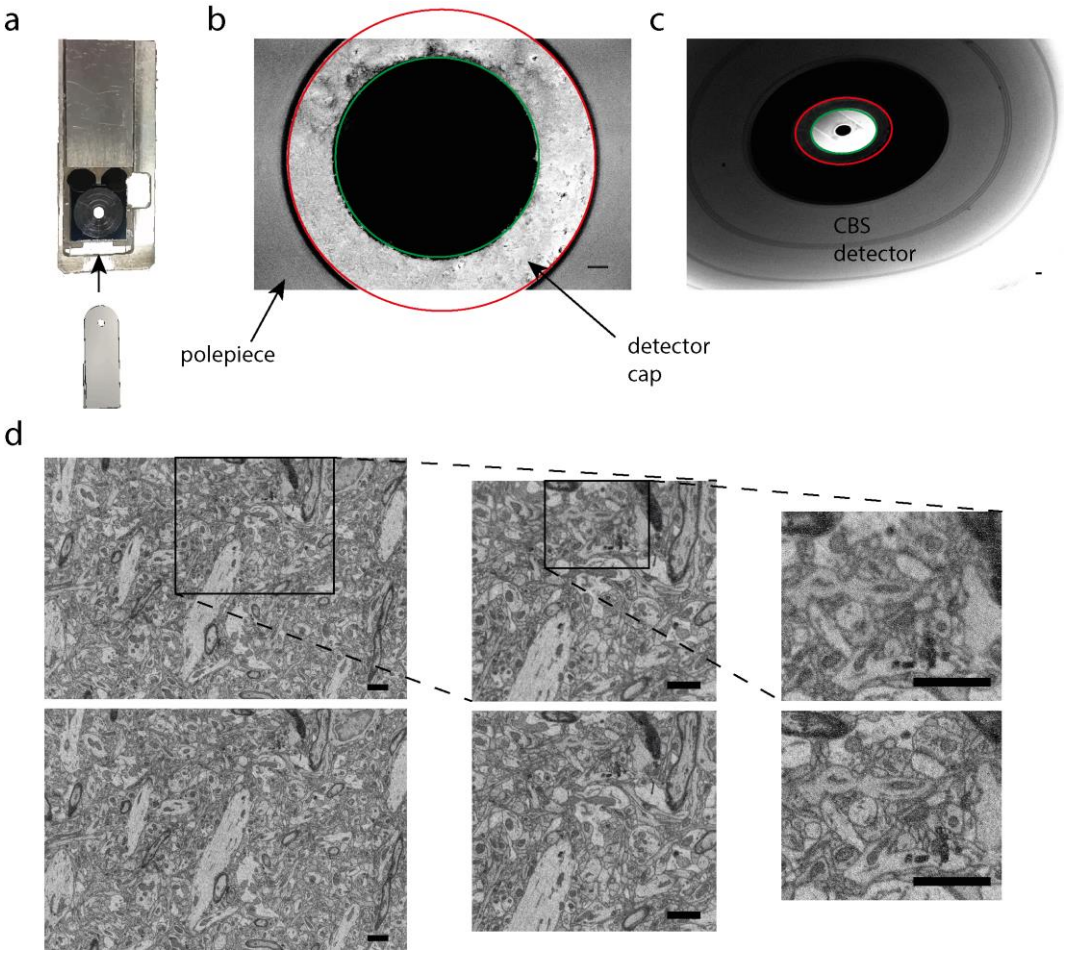

Figure 20: EM column protection. (a) CBS detector (FEI company) with custom designed detector cap, arrow indicating position of attachment. (b) Low magnification EM image, the detector cap clearly reduces the detector opening towards the pole piece (red = detector opening, green = detector opening with detector cap). (c) Mirror image of the column, showing the detector surface and detector cap (same color code as in (b)) Scale bars 100 µm. (d) Top image taken with 500 µm detector cap, showing defocused areas, bottom image taken without detector cap, crisp image (also applies for 1000 µm detector cap). Scale bars 2 µm.

2.2.2. Focus monitoring

Prior to data acquisition, a tool which allows focus monitoring for each plane on a single image basis (every image per plane gets checked) was developed. The code was written in Matlab. Basically, the tool is based on autocorrelation. Every image gets cross correlated with itself (=autocorrelation). Images with poor focus quality are represented with lower frequency levels in Fourier space. Therefore, Gaussian fit was applied on the autocorrelation (one dimensional) and focus as well as astigmatism quality were judged based on the main axes' length of an ellipse approximated with the radii from mean (spot peak) (Fig.21, a, c) to the standard deviations. Images with good focus resulted in high mean peaks and

smaller standard deviations making the approximated ellipse axes smaller, leading to a larger arbitrary value defined as “focus quality” (mean ellipse axis diameter^{-1}) (Fig.21, b, c).

As structures with less details and contrast like blood vessels and somata are primarily represented by lower frequencies after fast Fourier transformations (FFT) and would therefore cause many false positive data issues, those structures were masked by using Matlab’s built in edge detection and image processing functions (Fig 21, b). In order to identify even small onsets of defocus and astigmatism within a single image (see very local aberrations in Fig. 20, d), the algorithm was applied on 4 randomly sampled subimages (200 px x 200 px) within every image. If subimages contained more than 50 % masked structures, the algorithm was supposed to resample from another area. After 10 unsuccessful resampling procedures (e.g. blood vessel on the entire image), the value for the subimage region was set to NaN (not a number) and hence not taken into account for the data quality judgement.

While the overall image quality was primarily monitored manually by constantly checking the overviews provided by the algorithm (sent via E-mail) (Fig.21, b), automatic acquisition stops if image quality exceeded a certain threshold were implemented. In order to determine the threshold of minimal required image quality (axons and spine necks to be traceable), two members of the laboratory judged image quality of 50 randomly picked images. After comparing the binary decisions (1=image has sufficient quality, 0=image quality is too bad) with the values calculated by the algorithm for the respective images, a threshold for focus quality was set in the script, automatically stopping data acquisition in case the threshold is exceeded (Fig. 21, d).

In case the script stopped due to blurry images, focus and astigmatism were manually corrected for each motortile and the values committed as new “start points” for the autofocus script.

Although the applied heuristics were sufficiently good to detect severe image aberrations caused by catastrophic events such as column contamination, it still happened that some defocused images were undetected. Machine learning algorithms might improve the sensitivity in the future. Furthermore, integration of the focus quality detection into the script correcting for focus and astigmatism

(different algorithm) will most likely increase general data quality for future experiments.

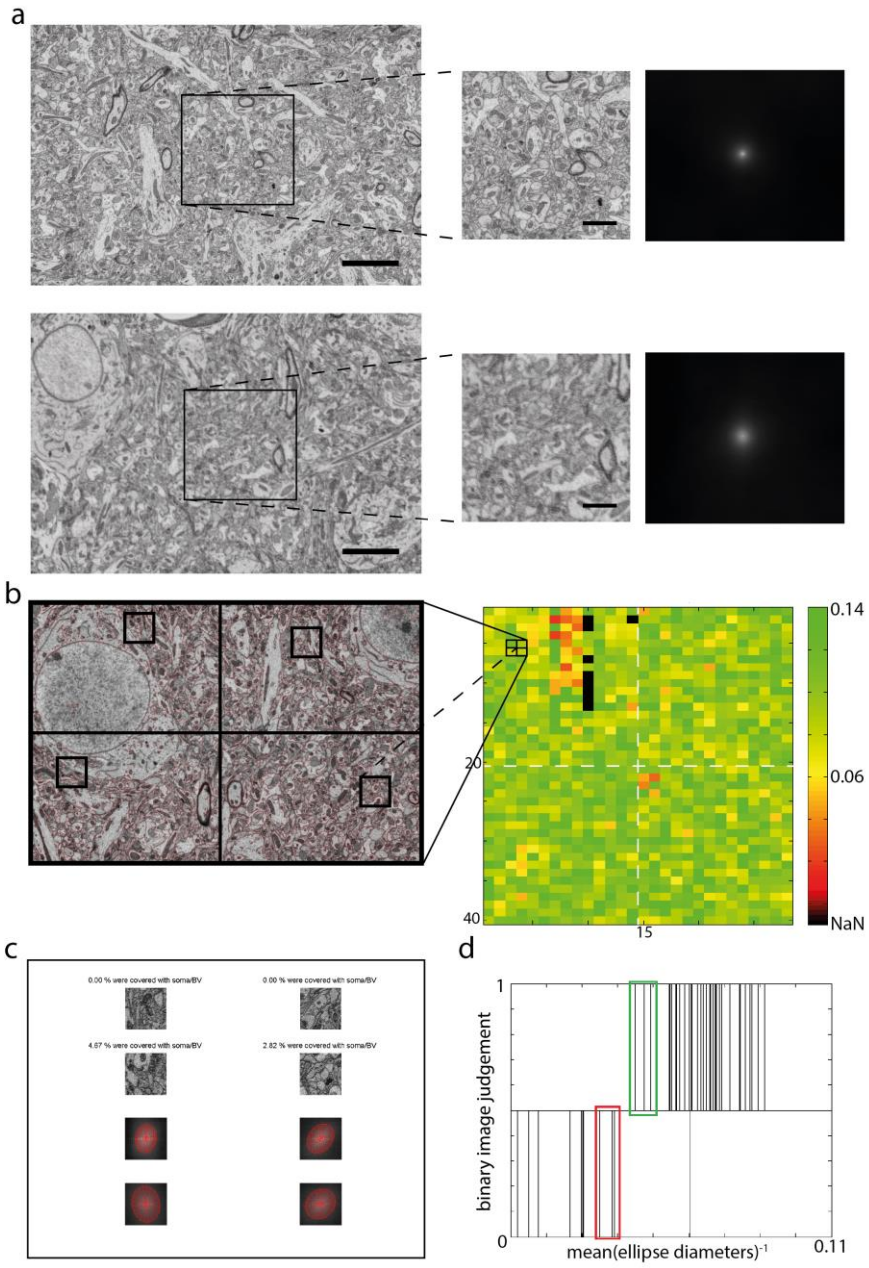

Figure 21: Focus monitoring. (a) Crisp image with its autocorrelation (top). Blurry image with its autocorrelation (bottom), note the less distinct peak in the bottom autocorrelation. Scale bars 5 µm, 2 µm, respectively. (b) Masked image (red = unmasked), quarters with random subimage sampling indicated (left). Calculated image quality overview on subimage resolution (1120 values), black spots mark large blood vessel within the dataset. (c) Ellipsoid approximation of the gaussian fitted autocorrelation of subimages (d) Threshold determination for autostop. Red and green rectangles indicate the transition zone from acceptable data quality to blurry images.

2.2.3. Reapproaching

If focus and astigmatism became too bad, data acquisition was paused (or it was stopped automatically). In case of such an event, it sometimes happened that the last triggered cut was performed several hours before (e.g. data acquisition gets automatically paused during the night). As temperature and humidity fluctuations could easily change the sample volume and hence the height of the sample by several hundreds of nanometers (or even µm), one has to take great care when reapproaching the knife towards the sample.

The sample was usually lowered by 5 µm and reapproached with 30 nm step size. After every cut an image outside the field of view region (to prevent sample charging in the region of interest) was acquired and the inter-image difference was manually checked. These reapproaches were performed three times, in all cases the sample was at least 100 nm lower (mean 150 nm) compared to the z position before the acquisition pause. As soon as the first cut was triggered, data acquisition was continued.

2.3. Image alignment

Image alignment was done in three steps. First, all images within one piezo column (10 images, 28 columns) were aligned using Speeded Up Robust Features (SURF) on the overlap areas (Fig.22, a1). The resulting image columns were subsequently aligned to their neighboring image columns within the same motortile using the same algorithm (Fig.22, a2)

Once, in plane alignment for each motortile was done, a region spanning 152 µm x 108 µm from the center of each plane was matched with its consecutive z slice using cross-correlation and the translation vector between the cross-correlation peaks to the subsequent image was applied (Fig.22, a3).

The so obtained 3D image stacks (four “sub-stacks”, referred to as MT1 to MT4) were finally converted into smaller UINT8 data cubes (128 x 128 x 128 voxels) (KNOSSOS data format (HELMSTAEDTER et al., 2011; BOERGENS et al., 2017)) and uploaded to the in browser online data annotation tool webKnossos (BOERGENS et al., 2017) for neurite reconstruction and synapse annotation.

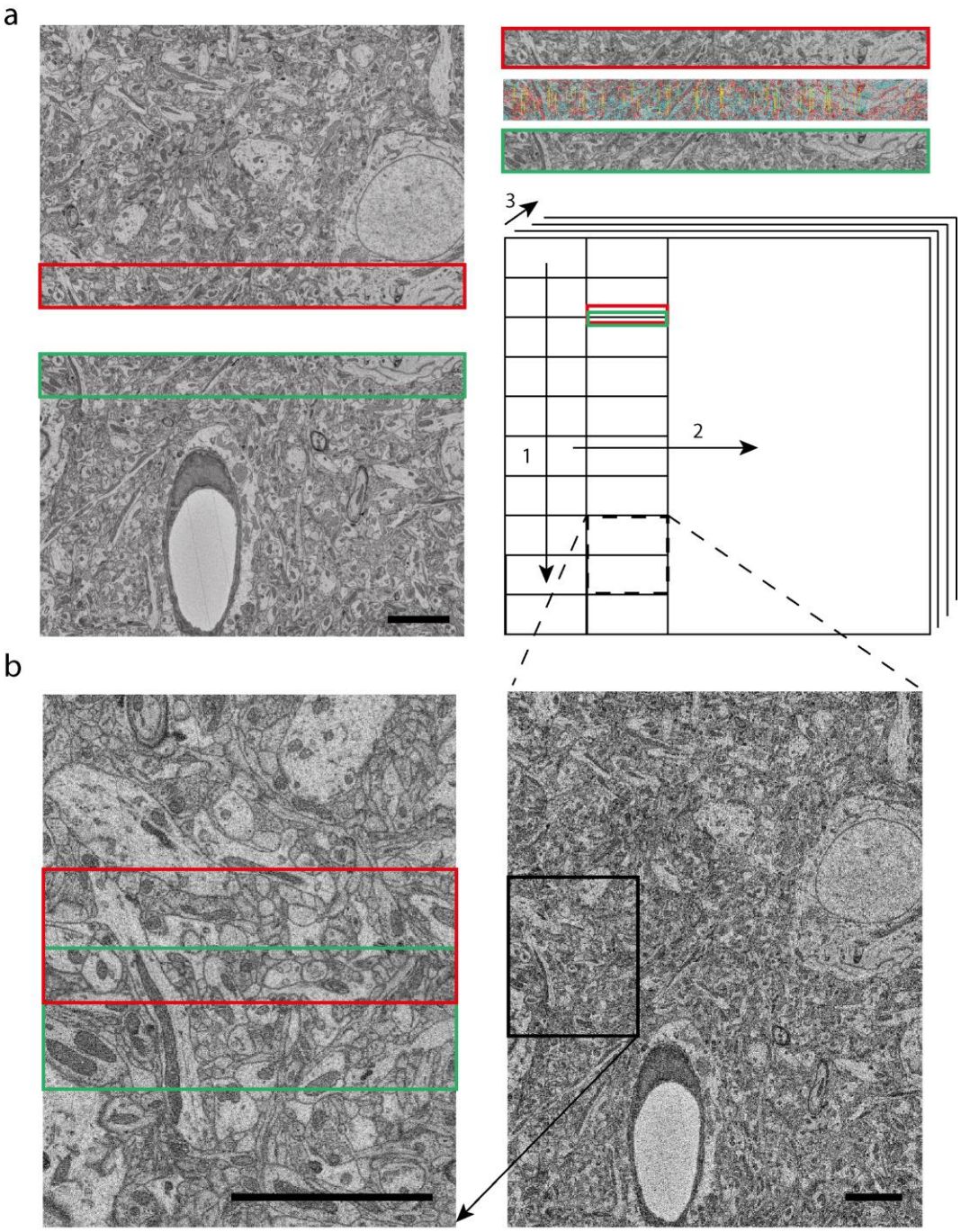

Figure 22: Image alignment. (a, left) Two neighbouring images within one piezo column. Red and green indicate area for SURF matching. (a, right) margins with SURF matching points plotted, scheme of image alignment, numbers indicating chronological order (1 = in column stitching, 2=in motortile stitching, 3=z-alignment). (b, left) Magnified stitching result in the overlap area between red and green rectangle. (b, right) Result of in column stitching exemplified with the two images from (a). Scale bars 5 µm.

3. Reconstructions

Although some visualizations are based on automated segmentations (BERNING et al., 2015), all analyzed reconstructions in this work are based on manual skeleton tracings in webKnossos (Fig. 23) and described subsequently.

To continue skeleton tracing across different motortiles, the neurite was identified in the adjacent motortile's overlap area (somata and myelinated axons were used as helpful landmarks) and a "node" (mark) was set as starting point at the exact same spot as the endpoint in the other motortile (Fig. 24, b). The difference between the end- and start point was subsequently used as a translation vector for a larger matrix (Fig. 24, c, d).

Once several translation vectors were calculated, the mean vector was used to reduce the search window and the skeletons in the adjacent motortiles were subsequently identified much faster (search window range of 2 µm, see Fig. 24, c).

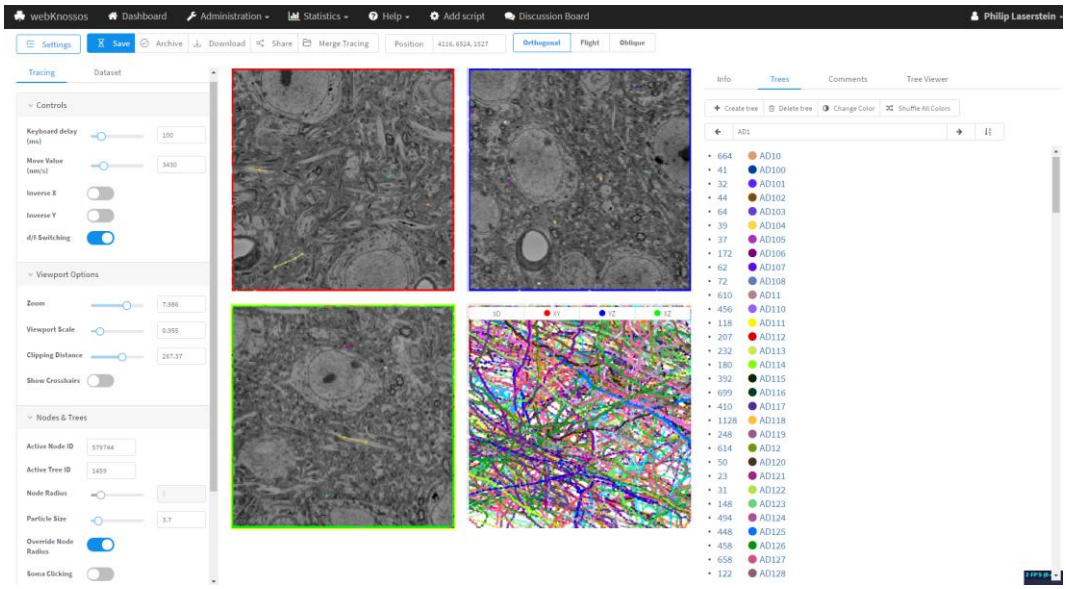

Figure 23: webKnossos. Snapshot of the webKnossos online annotation tool (BOERGENS et al., 2017). Red viewport = orthogonal view, blue and green viewport = resliced data. Bottom right viewport = nodes plotted as skeleton Trees.

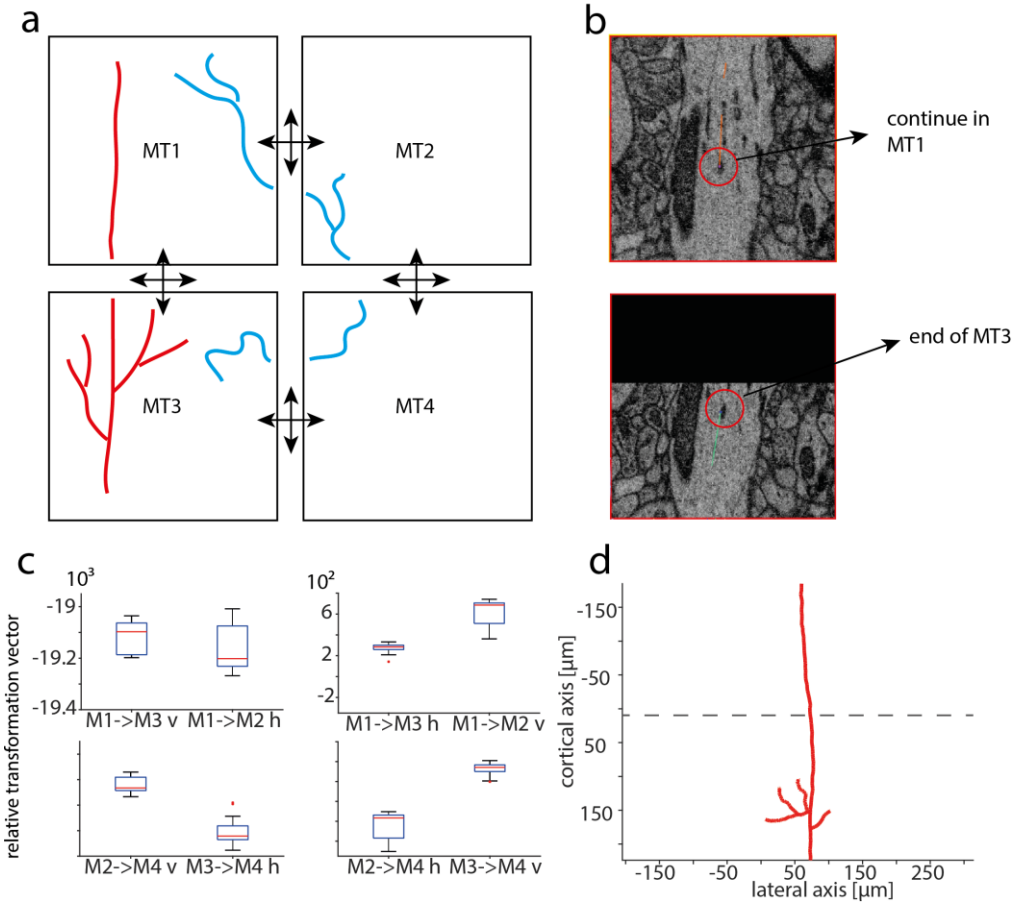

Figure 24: Skeleton translation across motortiles. (a) Motortiles with exemplary apical dendrite (red) and axon (blue) traveling across motortiles, 8 translation vectors indicated as arrows. (b) Example of how skeleton tracing was continued across motortiles. (c) Relative translation vectors (n=30) as indicated in (a), 2 µm range due to motortile based z alignment, h=horizontal, v=vertical. (d) Example of apical dendrite stitched across MT1 and MT3, dashed line indicates border.

3.1. Soma annotation

Two trained undergraduate students were asked to identify and mark all somata in MT1 – MT4 (Fig. 25). Two laboratory members revised the annotation, removed all glia cells and removed double annotations from the overlap area.

In total 1933 cell bodies were identified.

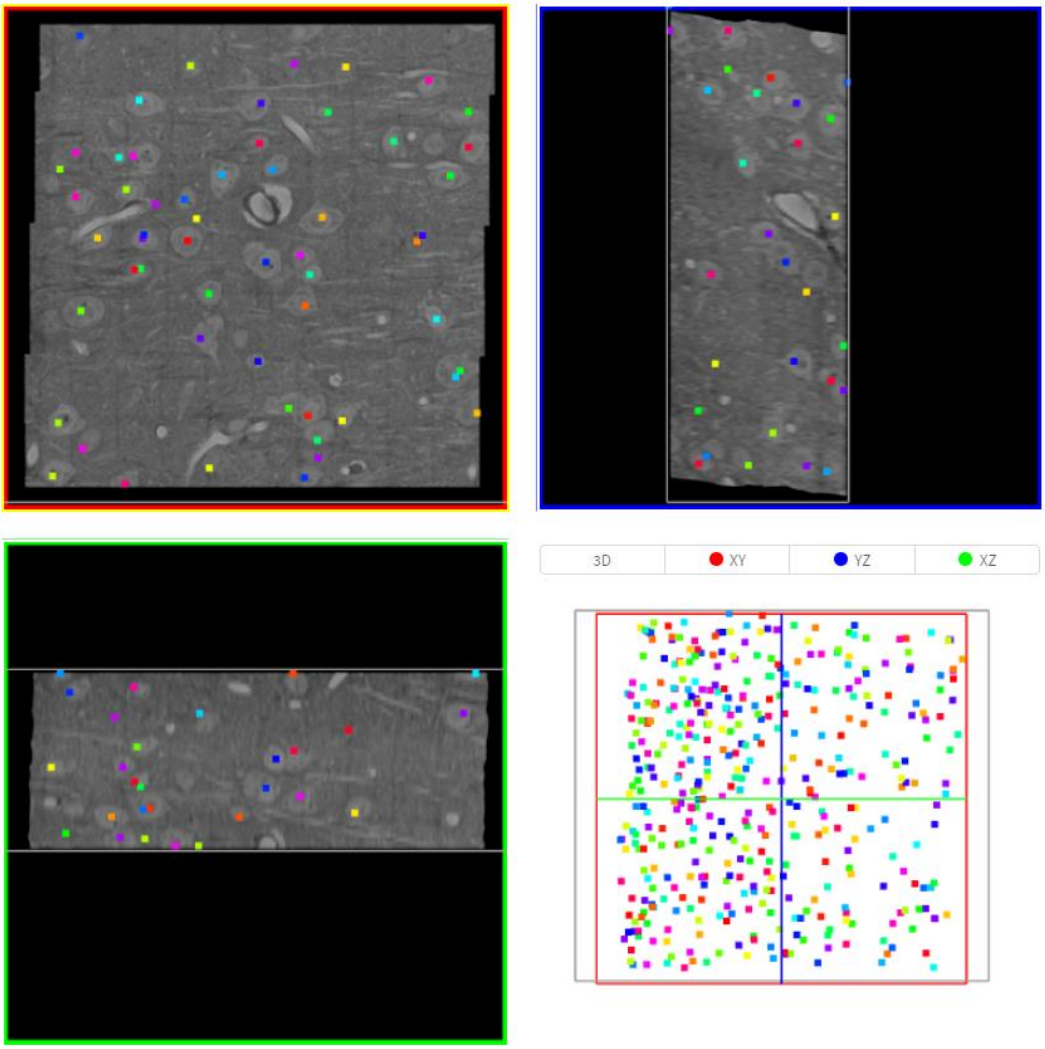

Figure 25: Soma annotation. Example of soma annotation within one motortile. Two undergraduate students placed nodes at the center of all somata within the dataset.

3.2. Apical dendrite reconstructions

In order to detect and reconstruct apical dendrites, large dendritic processes running along the cortical axis were first identified on low magnifications throughout the dataset and used as seed points (= start points for manual reconstruction). These dendrites were either reconstructed by the author himself or by three undergraduate students (per task). In case students did the reconstruction, the result was consolidated in order to obtain one correct tree. All dendritic trees were finally reviewed whether they matched the following criteria: 1) orientation along the cortical axis 2) mean diameter (>~1.0 µm). The initial pool of approved apical dendrites was extended when axons were reconstructed as described in 3.3 which were targeting other apical dendrites.

In total 238 apical dendrites accounting for 128.60 mm dendritic path length were reconstructed.

3.3. Axon reconstructions/Connectomical pheonotyping

The approach to identify axonal wiring specificity was based on the following procedure: a random synapse on a distinct neuronal structure (e.g. apical dendrite, apical oblique dendrite) was identified (synapse annotation, see 3.4.) (Fig. 26, a) and the synapse was used as a reconstruction seed node. Subsequently, the entire axon was reconstructed and all synapses annotated (Fig. 26, b). Then, the seed synapse was excluded and it was analyzed to what fraction the axon innervated different neuronal structures (Fig. 26, c). By reconstructing several axons seeded from synapses on a given postsynaptic target, the innervation profile of a given axon class was mapped (Fig. 26, d).

Postsynaptic targets were classified as: a) dendritic spine head b) dendritic shaft c) apical dendrite (shaft) d) apical dendrite (spine) e) apical oblique dendrite (shaft) f) apical oblique dendrite (spine) g) soma h) axon initial segment i) glia (Fig. 26). In order to clarify the identity of dendritic spine head targets, the spine neck was traced to reach the dendritic shaft. ~17 % of the spine necks could not be attached to their dendritic shaft and were accounted as “normal” dendritic spine heads (non- apical/apical oblique spine head). Dendritic shafts were classified as apical oblique dendrites if they clearly belonged to an apical dendrite (some false negatives as apical obliques could run out of the dataset). Axon initial segments were identified either by myelinization within the dataset or synapse formation.

In total 129 axons accounting for 57.75 mm axonal path length and 4979 synapses were annotated.

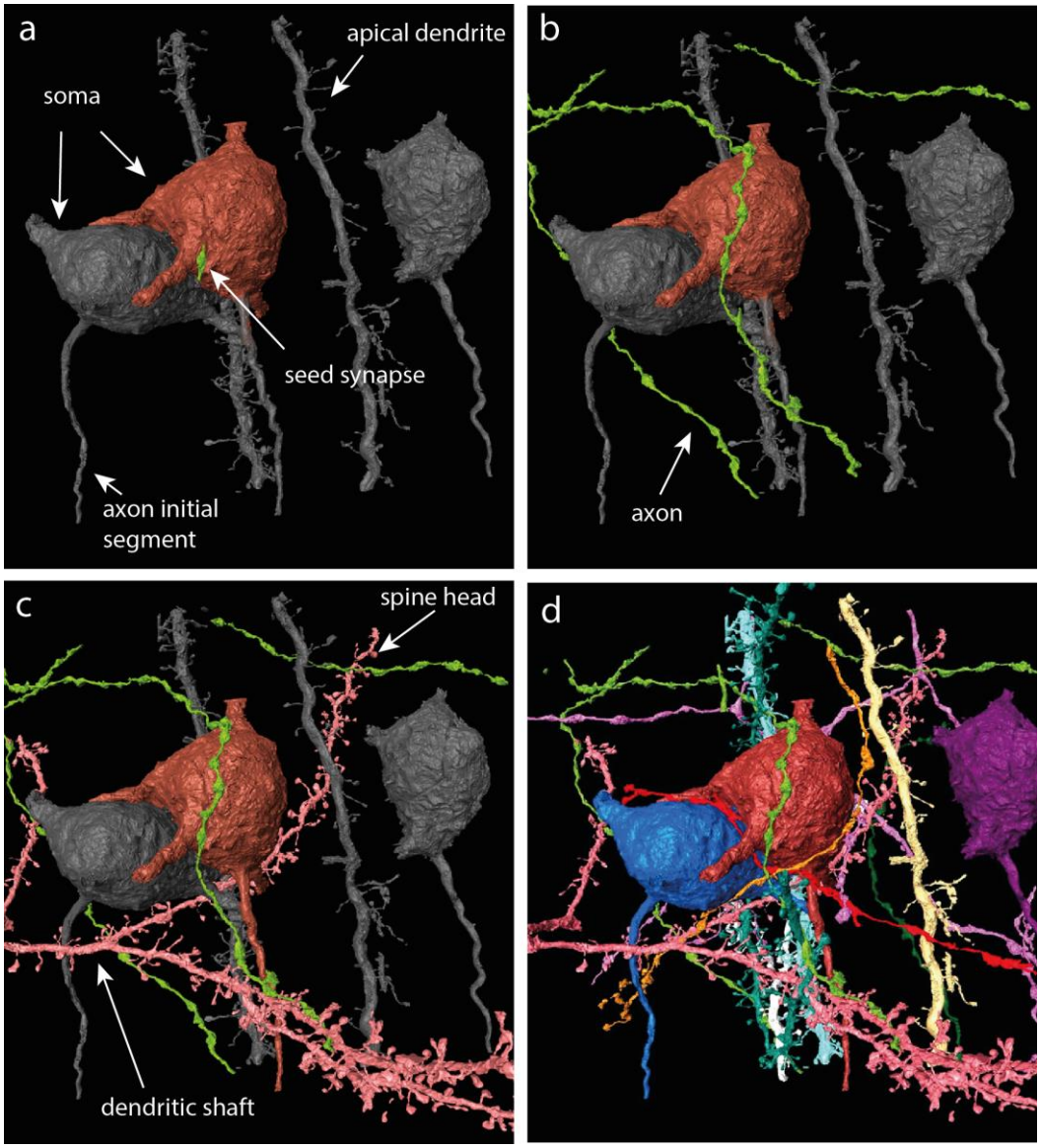

Figure 26: Connectomical phenotyping. (a) Synapse (green) seeded on a soma. (b) Presynaptic axon gets reconstructed (c) all output synapses and their postsynaptic targets get analyzed (spiny dendrite in pink as example for postsynaptic target other than the seeding target). (d) More axon reconstructions extend the connectomical phenotype of an axon class seeded from a given neuronal structure. Isosurfaces kindly provided by Anjali Gour and Heiko Wissler.

3.4. Synapse annotation

Output synapses were identified and annotated during axon reconstruction. Accumulations of synaptic vesicles were taken as evidence for a chemical synapse. In order to identify the postsynaptic target, the following criteria were applied: close proximity of pre- and postsynaptic membrane over a certain volume; vesicles close to potential synaptic cleft; presence of postsynaptic density (PSD) = dark and broad postsynaptic membrane (Fig. 27).

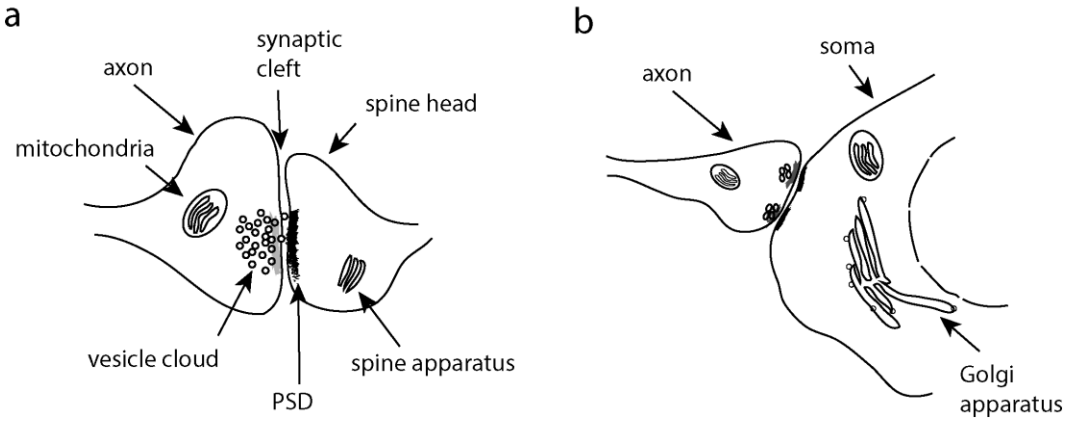

Figure 27: Synapse annotation scheme. (a) Excitatory synapse on dendritic spine head, broad and distinct PSD, also referred to as "asymmetric synapse/Gray type I" (GRAY, 1959). (b) Inhibitory axo-somatic synapse. Note two small and less distinct active zones, also referred to as "symmetric synapse/Gray type II" (GRAY, 1959).

While excitatory synapses appeared with broad and clear vesicle clouds and PSDs, inhibitory synapses on dendritic shafts and somata were more difficult to identify (Fig. 27, 28, 29, 30). Even though, TEM images with higher xy resolution clearly facilitate symmetric synapse visualization, the acquired SBEM images showed clear synaptic symmetry in many cases (e.g. Fig. 30).

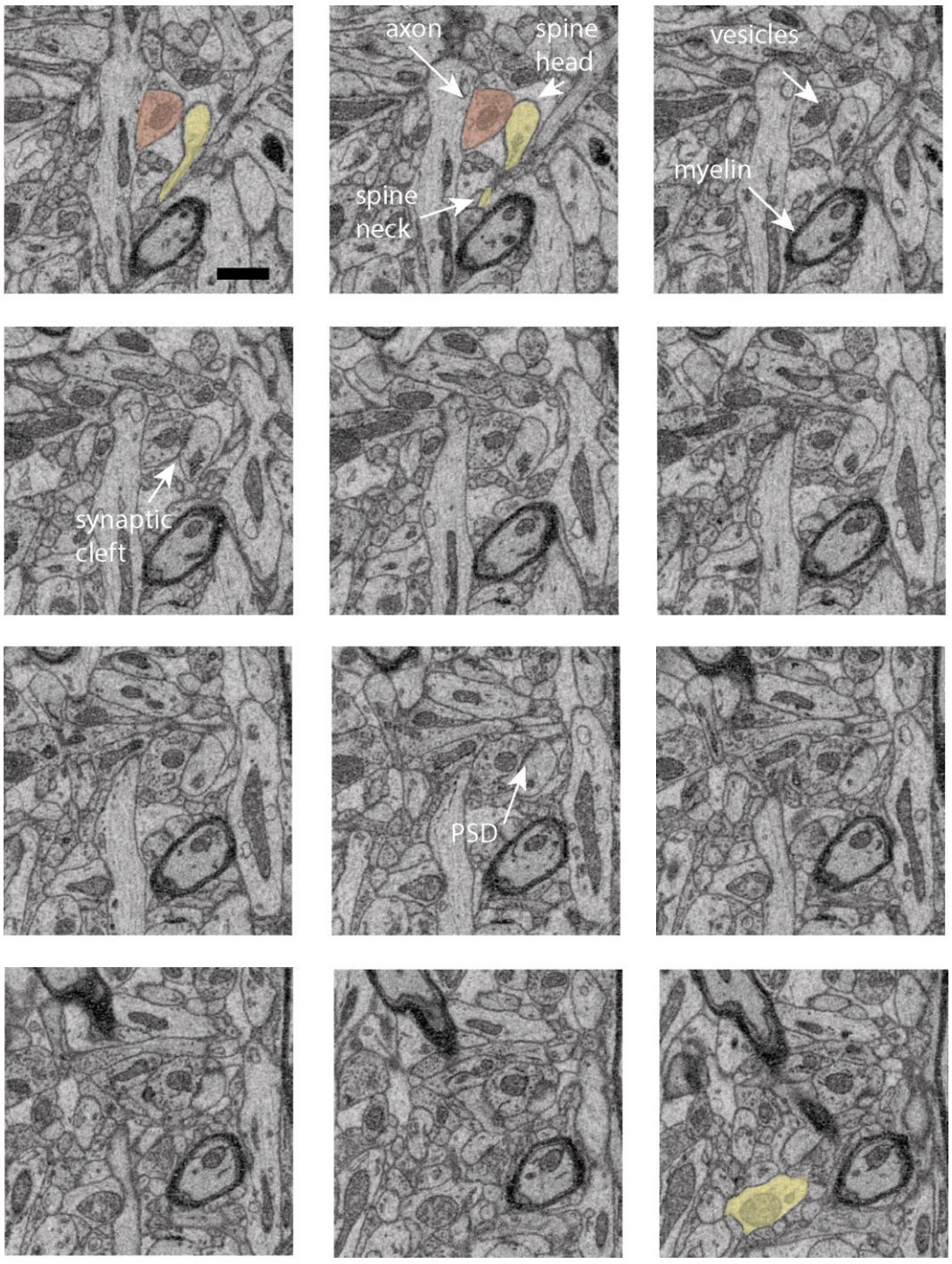

Figure 28: Excitatory synapse gallery. 501 x 501 pixel example image series, 660 nm tissue sectioned between first and last image (every 2nd plane shown). One exemplary synapse marked, annotation criteria indicated. Spine head originated from dendritic shaft indicated in yellow in the last image. Scale bar 1 µm.

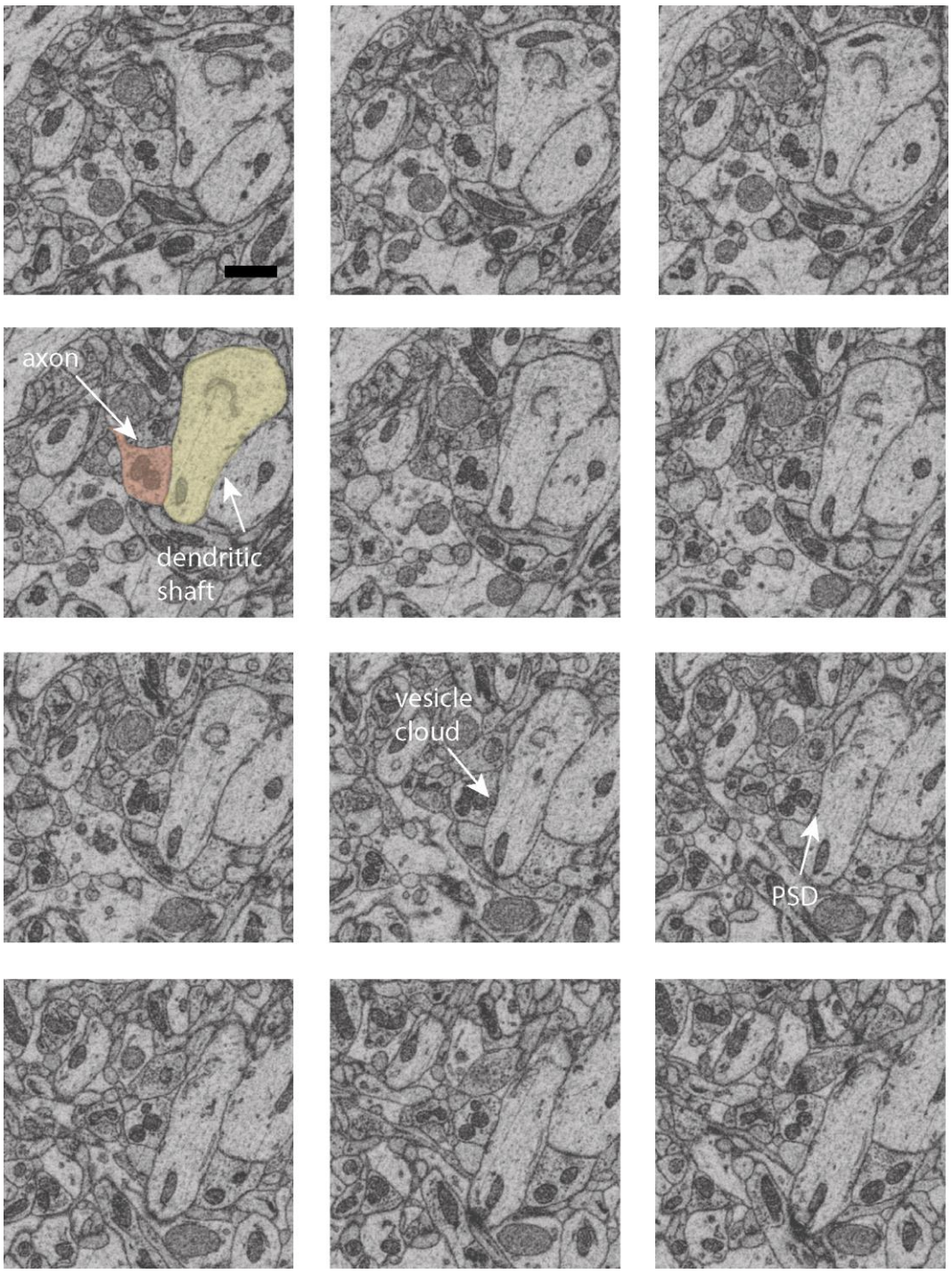

Figure 29: Inhibitory synapse gallery. 501 x 501 pixel example image series, 660 nm tissue sectioned between first and last image (every 2nd plane shown). One exemplary synapse marked, annotation criteria indicated. PSD less distinct compared to excitatory synapses. Scale bar 1 µm.

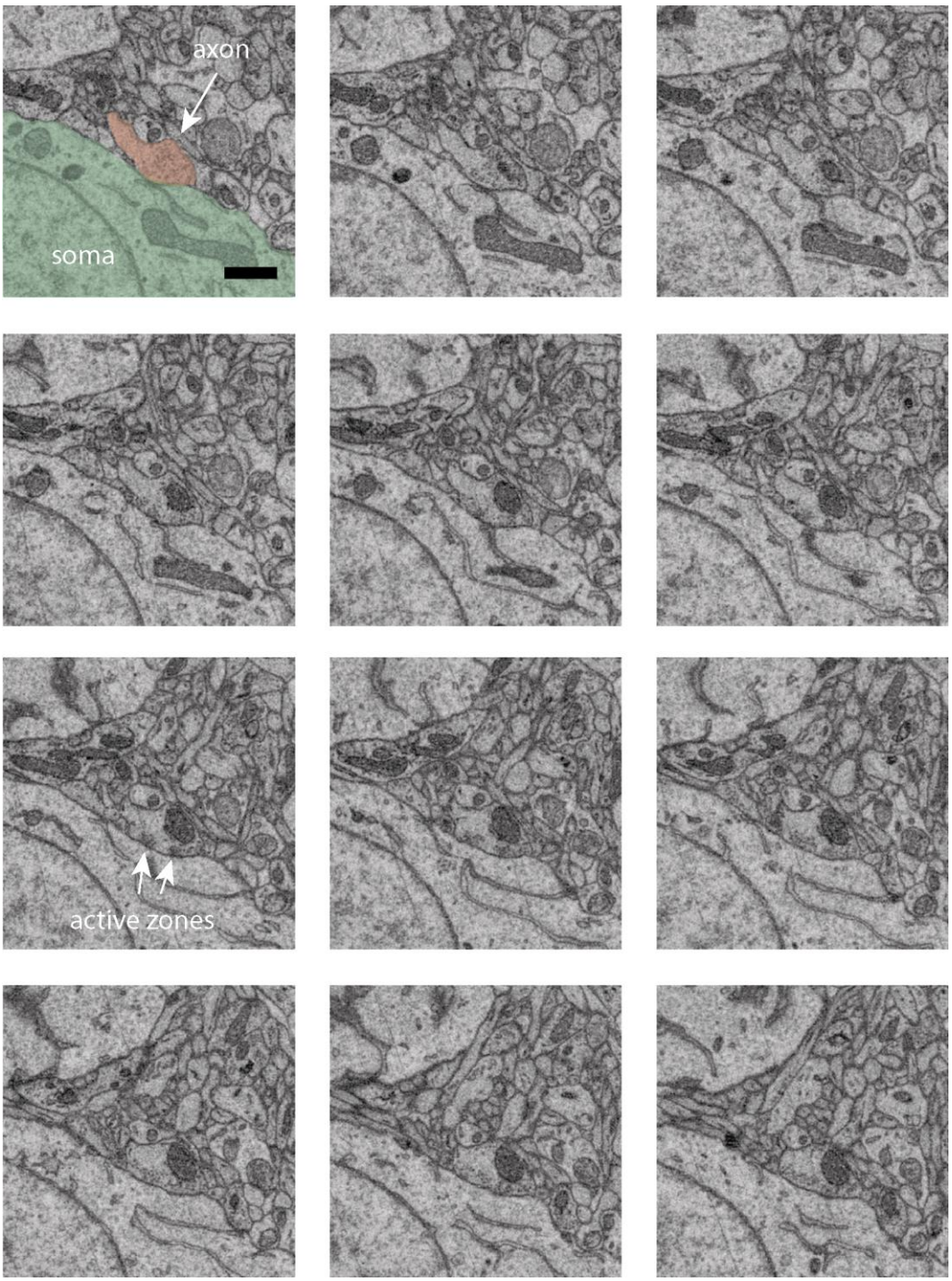

Figure 30: Axo-somatic synapse gallery. 501 x 501 pixel example image series, 660 nm tissue sectioned between first and last image (every 2nd plane shown). Symetric synapse (Gray Type II) with two less distinct active zones and minor PSD. Scale bar 1 µm.

3.5. Segmentation

In order to obtain volume reconstructions for visualizations and further analysis, an automated volume segmentation algorithm developed in the Helmstaedter laboratory was applied (BERNING et al., 2015).

Briefly, the algorithm is based on a convolutional neural network classifier, identifying membrane borders and therefore distinguishing intracellular from extracellular space. Subsequently the intracellular space gets segmented with a watershed based algorithm (Fig. 31, a). In order to minimize merger rates, a very small segmentation threshold resulting in rather over segmented data was used. All segments were marked with a unique segment ID and the segmentation was finally imported into webKnossos as a segmentation layer (visualization could be switched on/off).

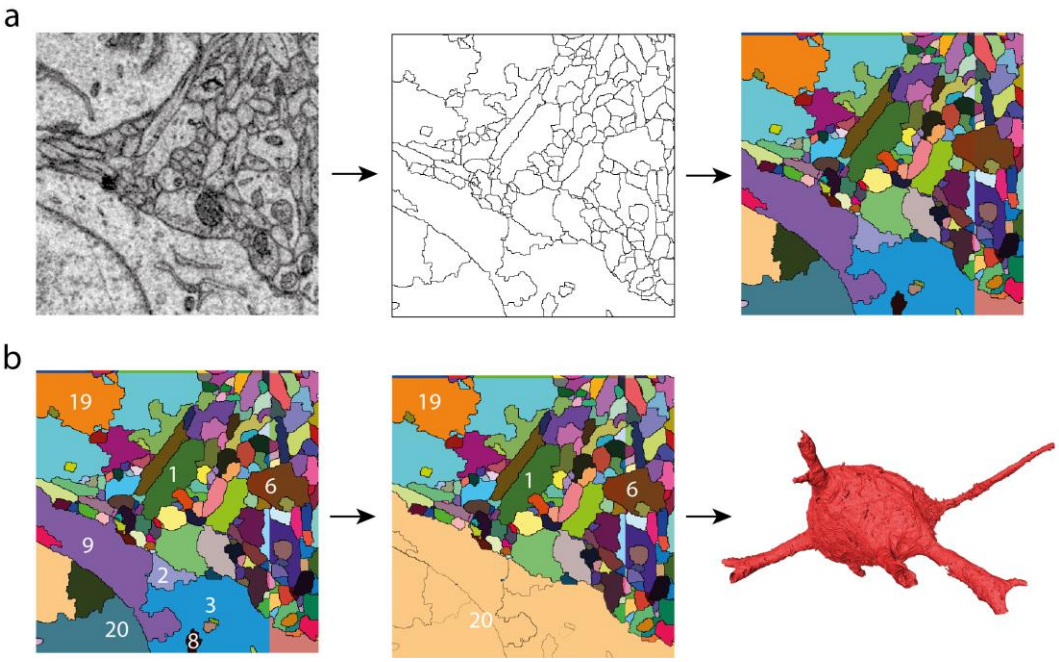

Figure 31: Segmentation for volume reconstruction. (a) Raw EM data (left) gets classified into binary data (middle) and subsequently colored with a watershed based algorithm (right). (b) Each segment is uniquely numbered (left), these IDs could be merged together as shown for an exemplary soma (middle). This pipeline allows 3D volume visualizations as exemplified for a soma (right).

Next, the segments belonging to the same cells were merged in order to obtain neuronal volume reconstructions from the over segmented data. A custom written script (by Kevin Boergens, Alessandro Motta et al.) was used which allows to mark all segments belonging to the same cell (merging segment IDs, “merger

mode"). Finally, the merged segments could be subsequently visualized with isosurface functions in Matlab and Amira (Fig. 31, b).

As generating segmentation data is very time consuming and costly in terms of computational power and storage (~6 TB/motortile), initially only MT3 was segmented for testing. The field of view for segmentation was sized 165 µm x 187 µm x 69 µm. It turned out that the merger rates were sufficiently good to use the segmentations for semi-automated volume reconstructions of larger dendrites (merger mode), but not sufficient for longer axonal and spine head reconstructions, most likely due to insufficient z-alignment and signal to noise ratio of the raw data.

4. Statistics

All axonal and dendritic measurements were considered as independent, normally distributed variables as they were individual neuronal processes. The results were considered significant if the null hypothesis was rejected at the 5 % significance level. This means that data in vector x and data in vector y come from populations with unequal means. If not indicated otherwise, mean values are given ± standard error of the mean (SEM).

IV. RESULTS

1. Dataset Overview

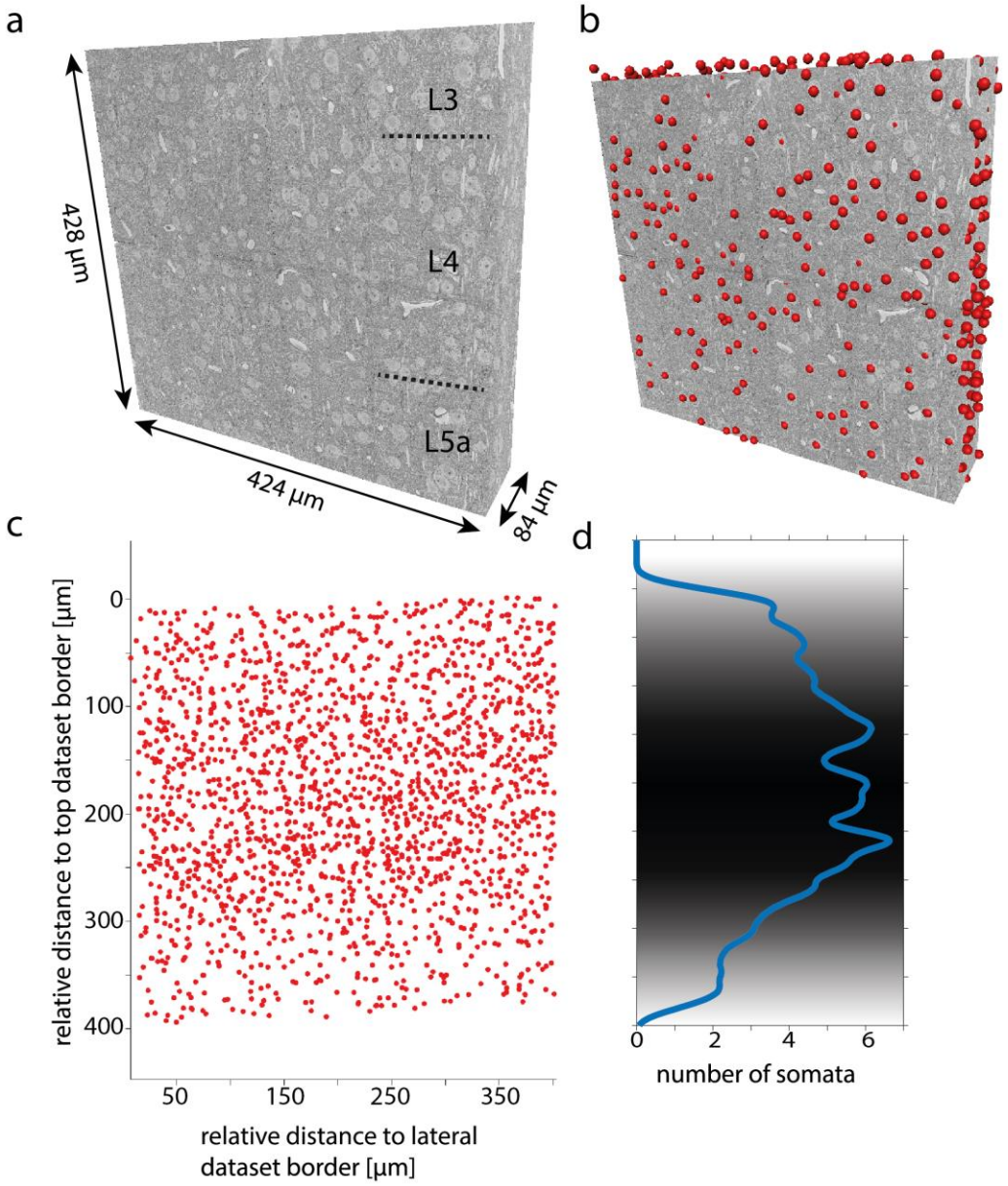

Figure 32: Dataset overview. (a) EM dataset with dimensions and layers indicated. (b) Dataset with soma somata plotted. (c) 2D projection of all somata, note the density differences. (d) Soma densities plotted as a Gaussian fitted curve, color gradient indicates density differences.

The 4.2 Mio megavoxel dataset was obtained in approximately 10 days continuous imaging time. Cytochrome C staining was used to assure and determine barrel location (LAND and SIMONS, 1985), the 1933 somata subsequently annotated by undergraduate students (see III. 3.1.) aided cortical layer detection.

The dataset was well centered in LIV barrel cortex, containing lower parts of LIII and upper parts of LV. The lower boundary of LIV was identified by the sharp drop in soma density and the occurrence of large LVa pyramidal neurons (MEYER et al., 2010b)(Fig. 32, 33). The upper boundary of LIV was determined via a) the occurrence of spiny stellate cells and their dendritic ends (LUBKE et al., 2000) b) increase in cell density (MEYER et al., 2010b) c) absence of large LIII pyramidal neurons (Fig.32,33).

Soma sizes were approximated by a 3x2 node annotation: two connected nodes at maximal diameter were placed in each webKnossos viewport (Fig.33, a). Each soma size was calculated as the mean path length of the three measured diameters. In this way, ten soma diameters were exemplary approximated for LIII-LVa each (Fig. 33, b).

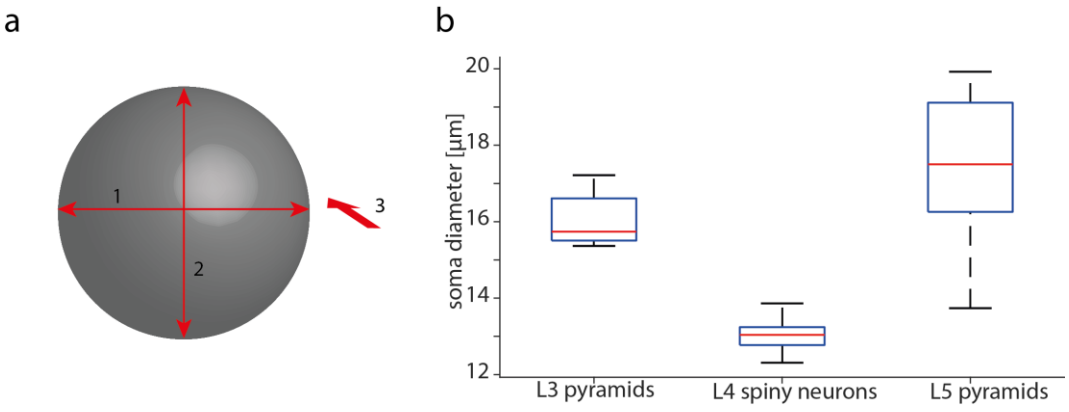

Figure 33: Soma diameter. (a) 6 point approximation of soma diameter. (b) Boxplot of mean diameters measured in (a), median indicated as red line, minimum and maximum indicated with bars. (n=10) each.

On average, L4 spiny stellate cells were sized 13.06 ± 0.44 µm (=SD), which was significantly smaller than L3 pyramids with an average soma diameter of 16.05 ± 0.69 µm (SD) (two sample t-test, $p=1.02*10^{-9}$) and L5 neurons with an average soma diameter of 17.45 ±1.93 µm (SD) (two sample t-test, $p=1.58*10^{-6}$).

In order to determine the relative fraction of excitatory sub cell types, another set of 40 excitatory neurons was sampled and the existence of apical dendrites was checked by tracing in order to determine the L4 excitatory cell type fraction. The relative fraction of L4 star pyramidal neurons was 14 %, which was smaller than what has been previously reported with light-microscopy (~20 - 25 %, rat) (LUBKE et al., 2000; STAIGER et al., 2004). The average diameter measured for L4 star pyramidal neurons was 14.56 ± 1.24 (SD). Two of the star pyramidal neurons were located at the edge of the dataset, such that only two diameters could be measured appropriately. In these cases, the mean of two measurements was calculated.

Table 4: L4 excitatory cell type species/method comparison. Diameters from references were given as vertical and horizontal diameter, calculated as in this dataset (mean of the two values). References apply for rat column.

	This dataset (=mouse)	Rat	Reference
L4 spiny stellate diameter	13.06 ± 0.44 µm	16.4 ± 2.1 µm	(STAIGER et al., 2004)
L4 spiny stellate fraction	86 %	75-80 %	(LUBKE et al., 2000; STAIGER et al., 2004)
L4 star pyramid diameter	14.56 ± 1.24 µm	17.4 ± 2.4 µm	(STAIGER et al., 2004)
L4 star pyramid fraction	14 %	20-25 %	See L4 fraction

1.1. Axon classification

All subsequently analyzed axons were classified either as inhibitory or excitatory axons. In case the soma was located within the dataset, this differentiation was rather obvious due to different dendritic and somatic morphologies (see II.2.2.2.). In all other cases the axon was classified based on its output synapses.

It is known that excitatory neurons primarily target dendritic spines (PETERS, 2002), while inhibitory neurons also target sub-cellular domains like somata, AIS and dendritic shafts in addition to dendritic spines (MARKRAM et al., 2004).

In order to double check these classification features, a set of three excitatory and inhibitory neurons with somata located within the dataset were reconstructed (Fig. 34).

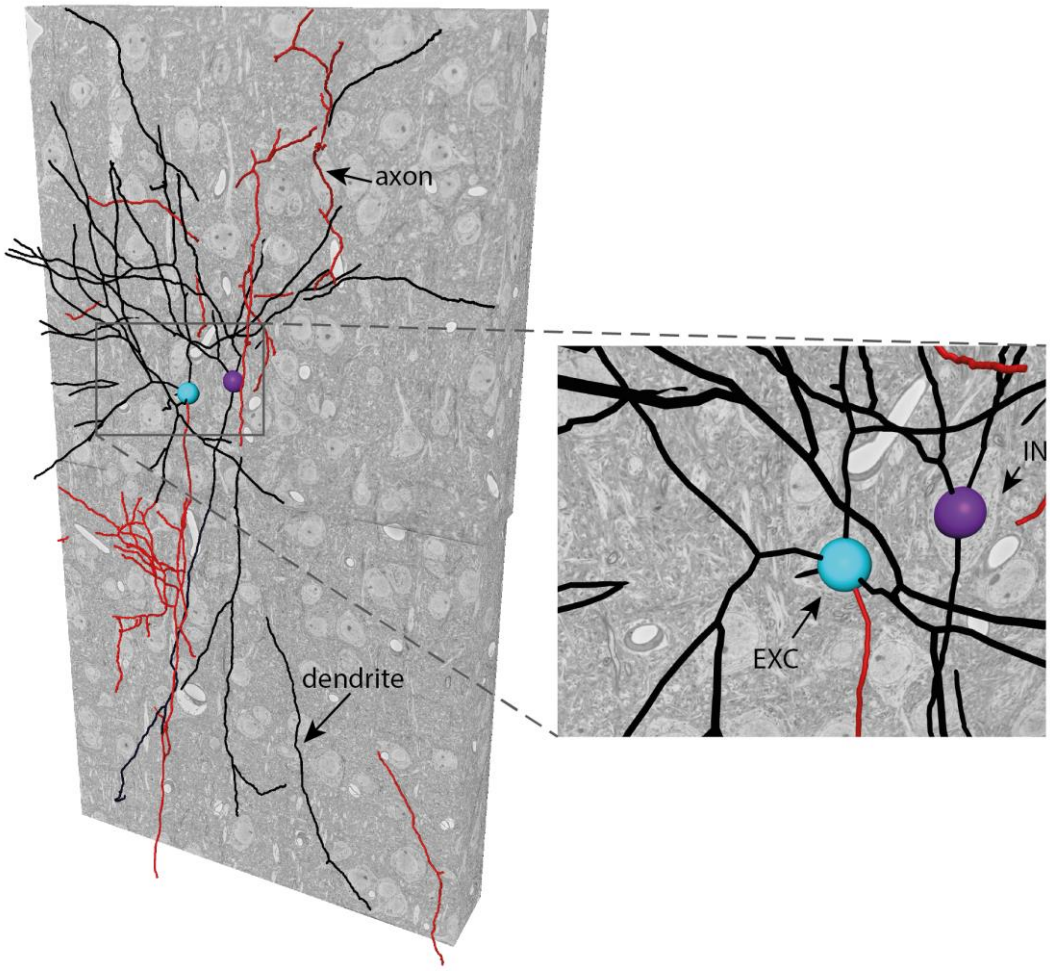

Figure 34: Excitatory and inhibitory cell morphology. One exemplary excitatory L4 spiny stellate cell (cyan soma) and one exemplary inhibitory L4 neuron (purple soma). Dendrites plotted in black, axons in red. Note the excitatory axon descending to infragranular layers while the inhibitory axon ascends to supragranular layers. Zoomed image (right) shows different soma morphology and size of the two neurons. Soma sphere diameter = 10 µm.

Table 5: Test set excitatory vs. inhibitory output fractions. Number of annotated synapses = 229 and 525 for excitatory and inhibitory population respectively.

Cell type	Target fraction Dendritic spine	Target fraction Dendritic shaft (+other targets)
Excitatory I	70.13 %	29.87 %
Excitatory II	81.42 %	18.58 %
Excitatory III	81.08 %	18.92 %
Inhibitory I	8.60 %	91.40 %
Inhibitory II	5.92 %	94.08 %
Inhibitory III	3.88 %	96.12 %

The reconstructed test set of axons totaled the axonal path length of 10.527 mm constituting 754 synapses. The reported output synapse fractions (Table 5) were corresponding to the previously described features, allowing axon classification of the two axon populations.

2. Apical dendrite innervation

2.1. Apical dendrite classification

238 apical dendrites were reconstructed with a total path length of 128.60 mm (Fig. 35) as described in III 3.2. and classified based on the following criteria: 1) soma located within dataset? If that was the case – 2) soma located in LIV/LVa? 3) Apical dendrite terminating in LIV?

By applying these criteria, apical dendrites were grouped in four classes 1) LIV star pyramid apical dendrites (soma within dataset) 2) LVa pyramid apical dendrites (soma within dataset) 3) deeper layer apical dendrites (unclear origin, LV-LVI) 4) LVI apical dendrites (terminating in LIV).

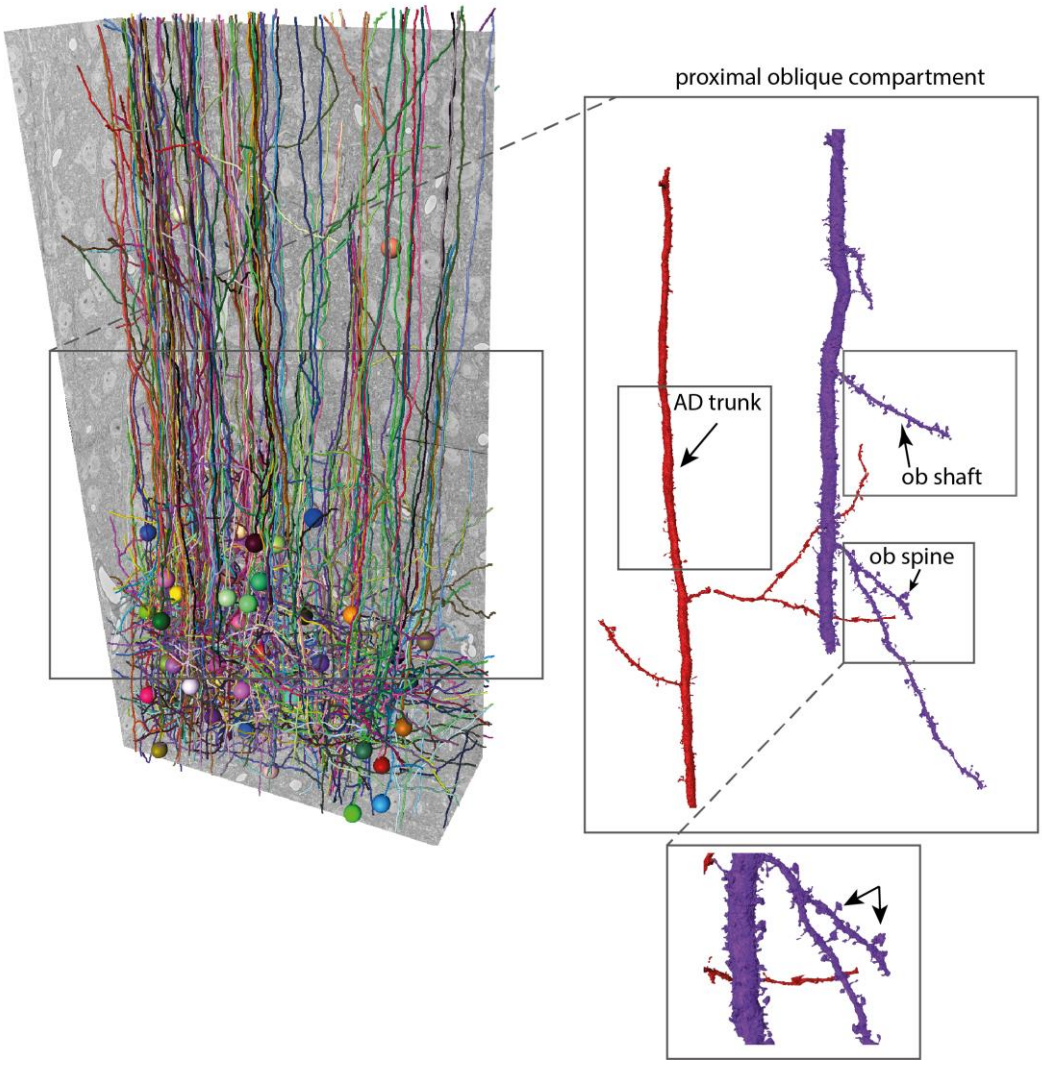

Figure 35: Apical dendrites. Left: plot of all reconstructed apical dendrites with their respective somata (if located within the dataset). Right: isosurfaces of two exemplary volume traced apical dendrites, spots of subsequent analyses/seeding spots indicated with arrows.

32 LIV star pyramid, 38 LVa pyramid, 27 LVI and 141 “deeper layer” (soma not present in dataset, apical dendrite not terminating in dataset) apical dendrites respectively were classified. In order to determine further distinguishable features, the diameter of 10 apical dendrites was measured for each group. Each diameter was measured at three different spots along the apical dendrite, each separated from each other by at least 50 µm dendritic path length and at least 50 µm away from the soma (if present, in case of L6 pyramids 50 µm from the lower dataset border)(Fig. 36, a).

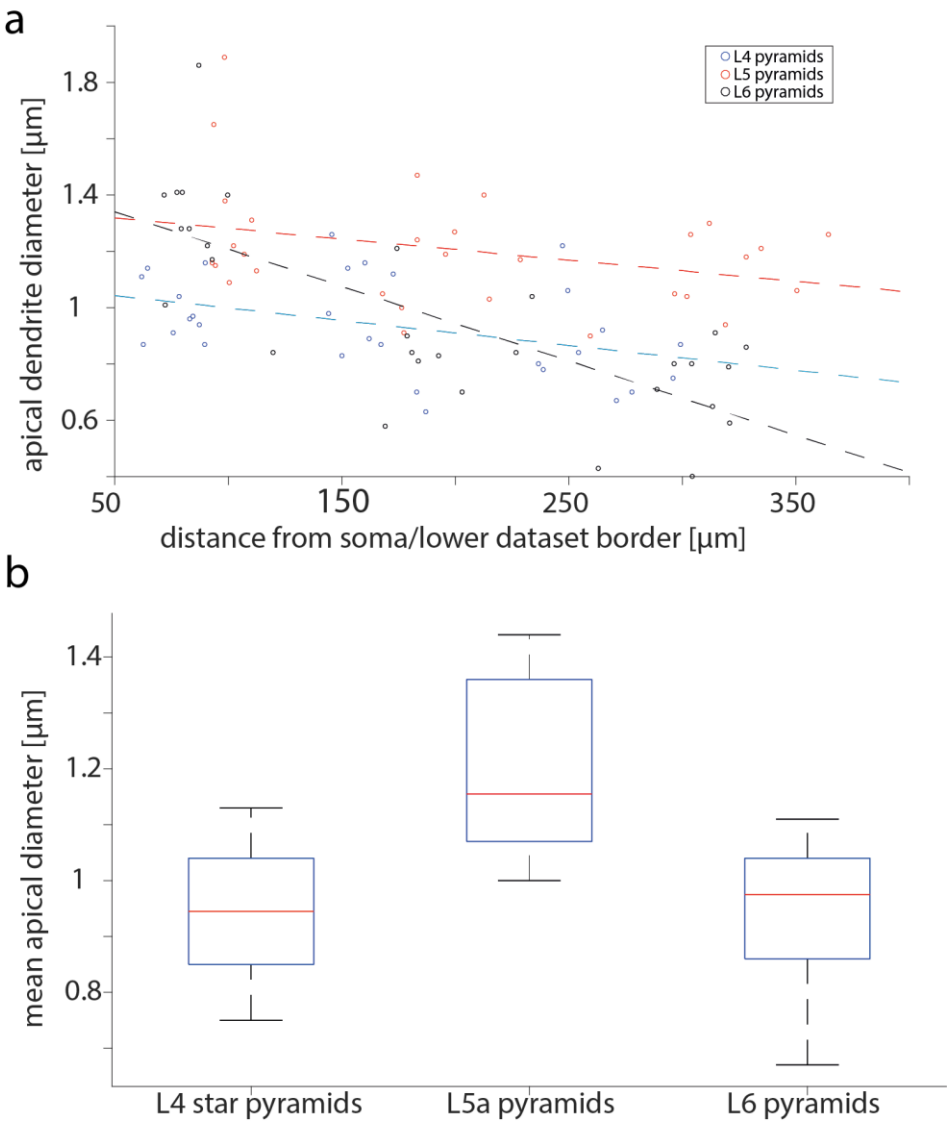

Figure 36: Apical dendrite diameters. (a) Apical diameters measured at three spots each, dashed line = least square line for each apical dendrite class. (b) Mean apical diameter for each cell type, red bar=median, black bars=min/max.

At each spot the diameter was approximated with two orthogonal lines, the mean path length of these lines was taken as diameter for this measurement spot. The mean diameter for each apical dendrite was then averaged over the three measurements (Fig. 36, b).

The mean apical dendrite diameter was 0.94 ± 0.125 µm (SD), 1.20 ± 0.156 µm and 0.95 ± 0.128 µm (SD) for LIV star pyramids, LVa pyramids and LVI pyramids respectively. Hence, apical dendrites originating from LIV star pyramidal and LVI neurons were significantly smaller than apical dendrites originating from LV pyramids (two sample t-test, $p=6.12*10^{-4}$ and $p=1.1*10^{-3}$). The difference between LIV and LVI apical dendrites was not significant (two sample t-test, $p=8.07*10^{-1}$). Although all apical dendrites decreased in size while ascending towards pia (Fig. 36, a), the effect was most visible for LVI pyramidal neurons due to their termination zone in LIV (see black dashed line in Fig. 36, a).

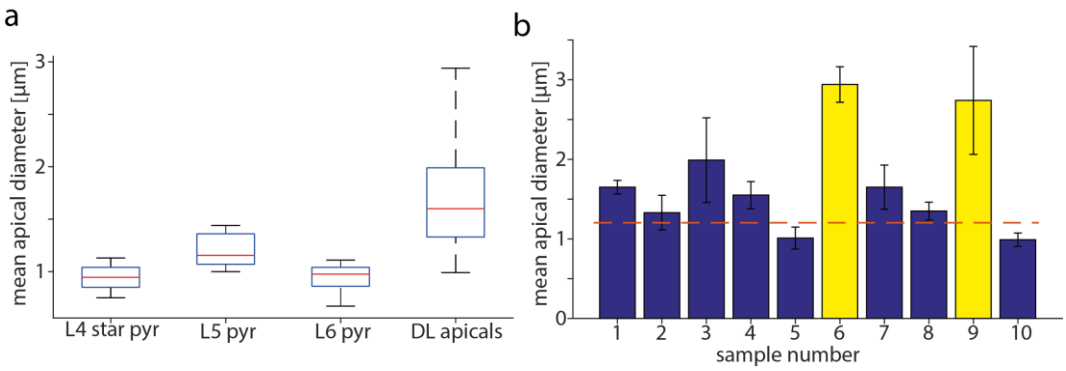

Figure 37: Deeper layer apical dendrites diameter. (a) Apical diameter boxplot including unspecified "deeper layer" apical dendrites, note the large range indicating inhomogeneous population. (b) Apical diameters of DL apicals in (a), red line indicates mean diameter of L5A pyramidal neurons, error bars = SD. Yellow bars indicate potential L5B or other L5 subpopulation (>2 SDs from mean diameter of L5A population measured).

In an attempt to further classify the "deeper layer" apical dendrites, which were neither terminating nor had a soma within the dataset, 10 apical diameters of this population were measured as well (same measurement method applied as for the other groups). This population turned out to be rather inhomogeneous (Fig. 37, a) most likely containing LVb and LVb pyramidal neurons (and potentially a couple of slightly oblique running LVI apical dendrites). The mean diameter for deeper layer apical dendrites was 1.72 ± 0.664 µm (SD). It appeared that at least 2 apical dendrites were much larger (2.94 ± 0.223 µm and 2.74 ± 0.678 µm) (SD) than the others and the mean diameter of the previously measured LVa apical dendrites

(max LVa = 1.44 µm) (Fig. 37, b).

2.2. Apical dendrite innervating axons

As described in chapter II 3.2., LV pyramidal neurons carry the salient feature of a calcium spike initiation zone at their distal apical dendrite. The intermediate compartment of those apical dendrites was considered to most likely receive inhibitory inputs tuning the calcium spikes and the back-propagating action potentials (see chapter II 3.2, 3.3.). In order to investigate whether those predicted inhibitory inputs exist and are originating from a certain type of axons, preferentially innervating certain cell types (e.g. exclusively infragranular apical dendrites), 47 axons with a total path length of 24.88 mm which were seeded (see chapter III 3.3. for more detail) from 14 different apical dendrites were reconstructed and all 2254 established synapses were annotated.

Initially, 30 axons from 9 different infragranular apical dendrites (DL + LV, subsequently referred to as “DL ADs”) and 17 axons from 5 different LIV star pyramid apical dendrites were seeded in order to investigate cell type specific innervations (do axons preferentially innervate one AD class over another?) (Fig. 39, d). However, after profiling the axonal path length relative to cortical depth it turned out that 10 out of 30 DL AD seeded axons do not innervate LIV ADs due to absence of axonal structures within the corresponding cortical depth and were therefore excluded from the analysis.

The remaining 20 axons seeded from 9 different deeper layer apical dendrites accounted for 10.258 mm axonal path length (mean = 512.92 µm) and formed 779 synapses on identified postsynaptic targets. The axon population seeded from LIV pyramidal neurons totaled 13.068 mm axonal path length (mean = 768.73 µm) and established 1212 synapses on identified postsynaptic targets (Fig. 38, b).

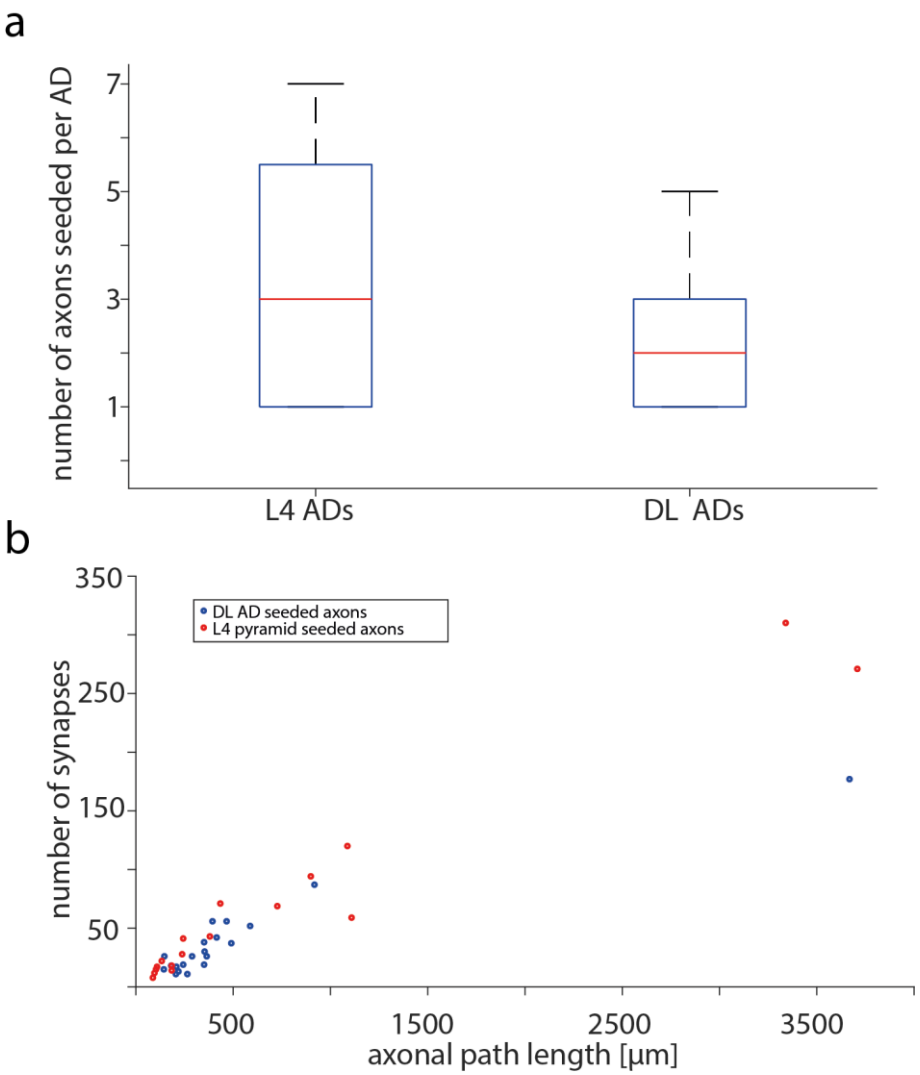

Figure 38: Apical dendrite innervating axons. (a) Number of sampled axons per apical dendrite (AD n=5 and AD n=9, respectively). (b) Number of synapses relative to axonal path length (n=37 axons, 1991 synapses).

On median, three axons per LIV AD (max: 7) and two axons per DL AD (max: 5) (Fig. 38, a), were sampled within the LIV compartment of the apical dendrite.

In both classes the axonal path length correlated with the number of output synapses (Fig. 38, b), indicating similar synapse density. This positive correlation was weaker in one of the DL AD seeded axons due to extensive axon myelinization.

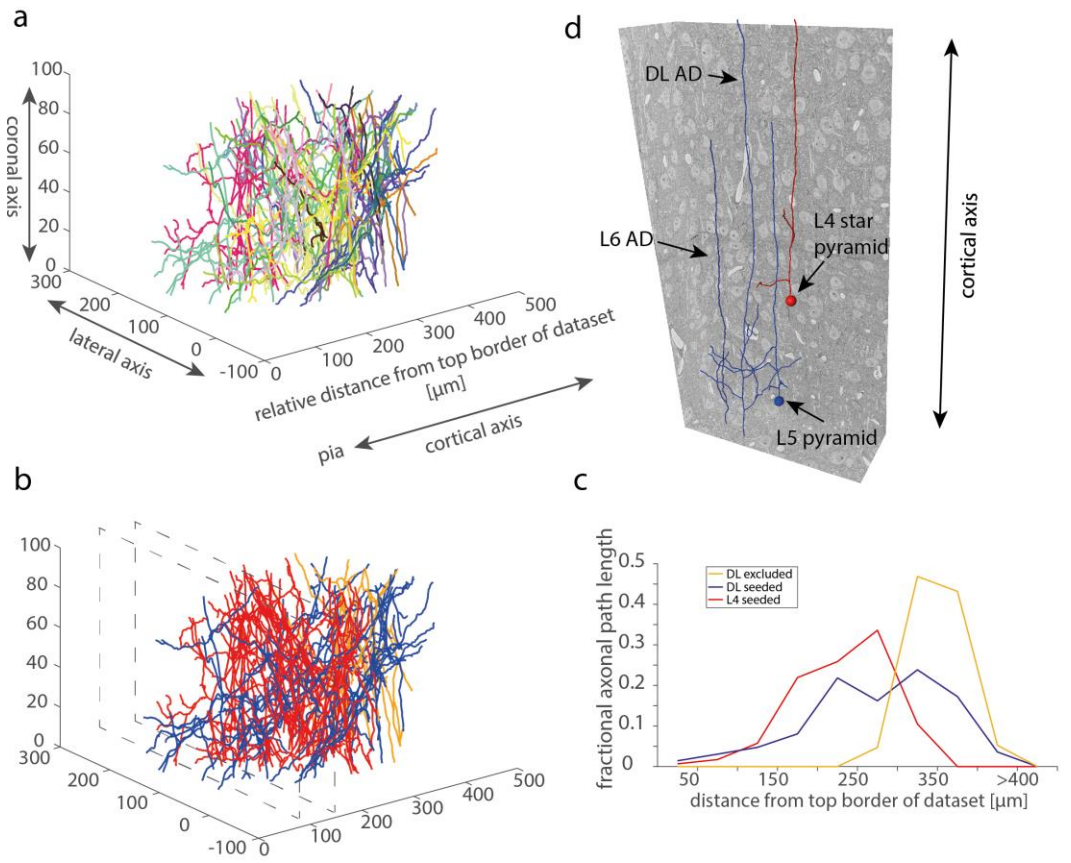

Figure 39: Apical dendrite innervating axons, seeding and path length. (a) 3D plot of all seeded axons. (b) 3D plot of all seeded axons, color coded with respect to their seed type (as in c). (c) Mean fractional axonal path for each seeded axon population, measurement indicated as dashed frame in (b). (d) Plot of different apical dendrites present within the dataset. DL ADs plotted in blue, L4 AD in red.

2.3. Apical trunk innervation

The reconstructed axons formed synapses onto 89 individual apical dendrites, of which were 20 LIV ADs, 12 LV ADs, 7 LVI and 50 unclassified DL ADs. The other postsynaptic targets were classified as a) AIS b) soma c) shaft d) spine e) oblique f) glia.

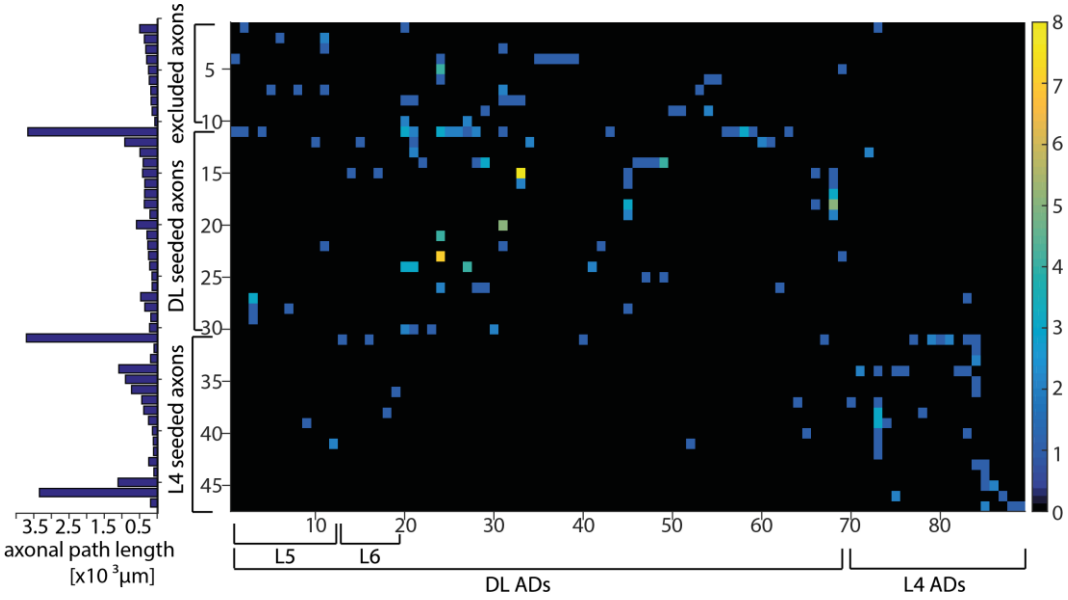

Figure 40: Apical dendrite connectome. Right: 47x89 matrix with all presynaptic, AD innervating axons on the y axis vs all apical dendrite targets on the x-axis, seeding synapses shown. Color bar indicates number of synapses per target. Left: corresponding axonal path lengths.

The connectivity matrix of all presynaptic axons vs. all postsynaptic apical dendrites (=Connectome, see Figure 40), shows the absence of connections between DL AD seeded axons and L4 ADs and L4 AD seeded axons and DL ADs, suggesting specific innervation profiles of these two axon classes.

In order to quantify that finding, all synapses formed by each of the 37 axons (10 removed but included in Figure 40, see IV 2.2.) were summed up and the relative fraction of synapses on each postsynaptic target was calculated (Fig. 41) (see III 3.3. for cortical phenotyping method).

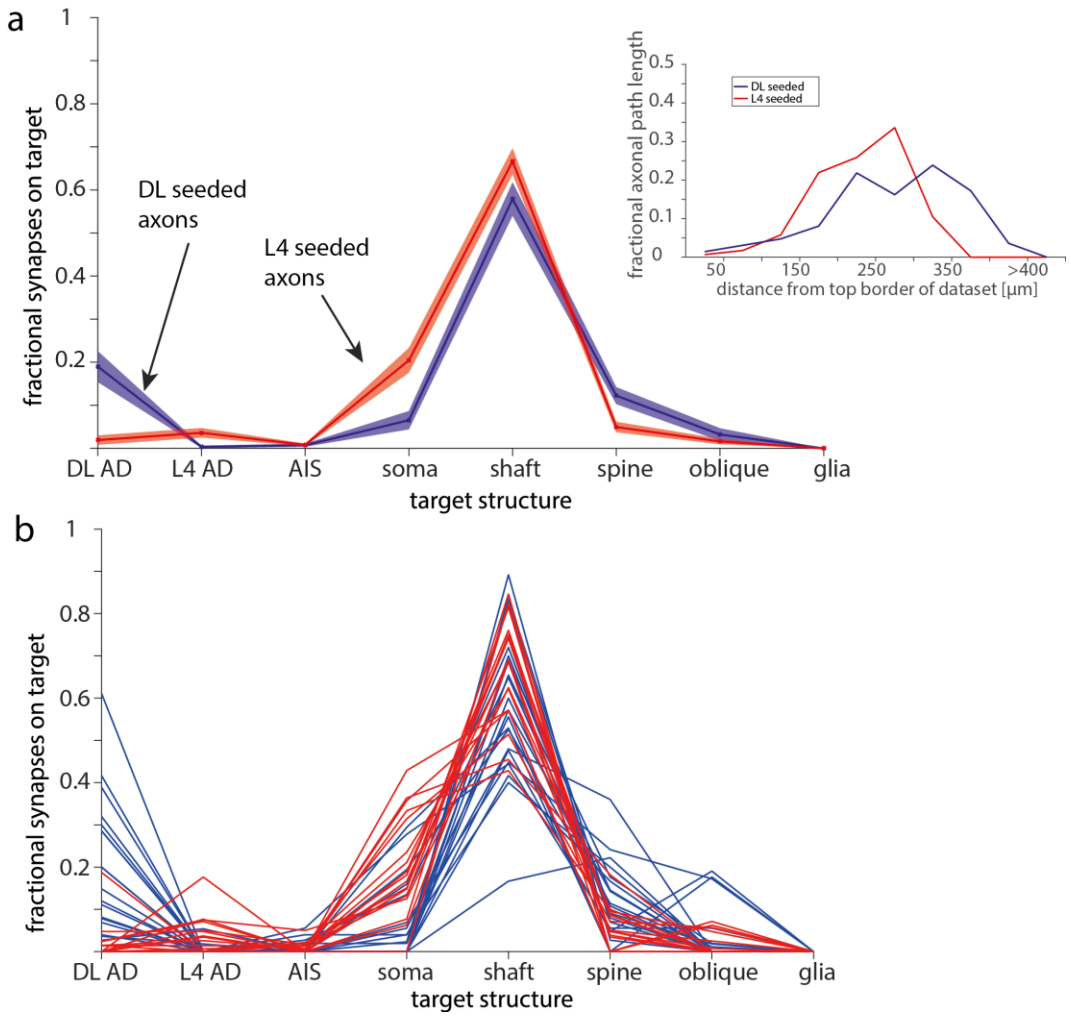

Figure 41: Axonal apical dendrite target fraction. (a) Mean target fraction over all reconstructed axons, SEM indicated as shading. Small plot = fractional path length for both axon populations. (b) Single target fractions of the axon population plotted in (a), same color code applies, seeding synapses removed in both plots.

The axon population seeded from deeper layer apical dendrites, kept innervating these structures with an average synaptic ratio of 19.01 % ± 3.58, while sparing LIV star pyramidal apical dendrites (mean fractional innervation = 0.36 % ± 0.28 (Fig. 41, a). Only one out of the twenty axons did not form any further synapses on deeper layer apical dendrites.

Only two of these axons innervated any LIV star pyramidal apical dendrite at all (2 synapses and 1 synapse, respectively) (Fig. 40). When binarizing the connections between axon classes and ADs (=multiple innervations of the same apical dendrite get accounted as 1), the fractional innervation of DL ADs dropped to 9.85 % ± 2.16 (two sample t-test: $p=3.5*10^{-2}$), indicating that DL AD targeting axons run along a few ADs innervating them twice on average rather than

innervating multiple ADs a single time. The maximum number of synapses formed on a single AD was 8 (mean=2.14 ± 0.26, the maximum number of different ADs innervated by a single axon was 17 (mean=3.7 ± 0.80) (Fig. 42).

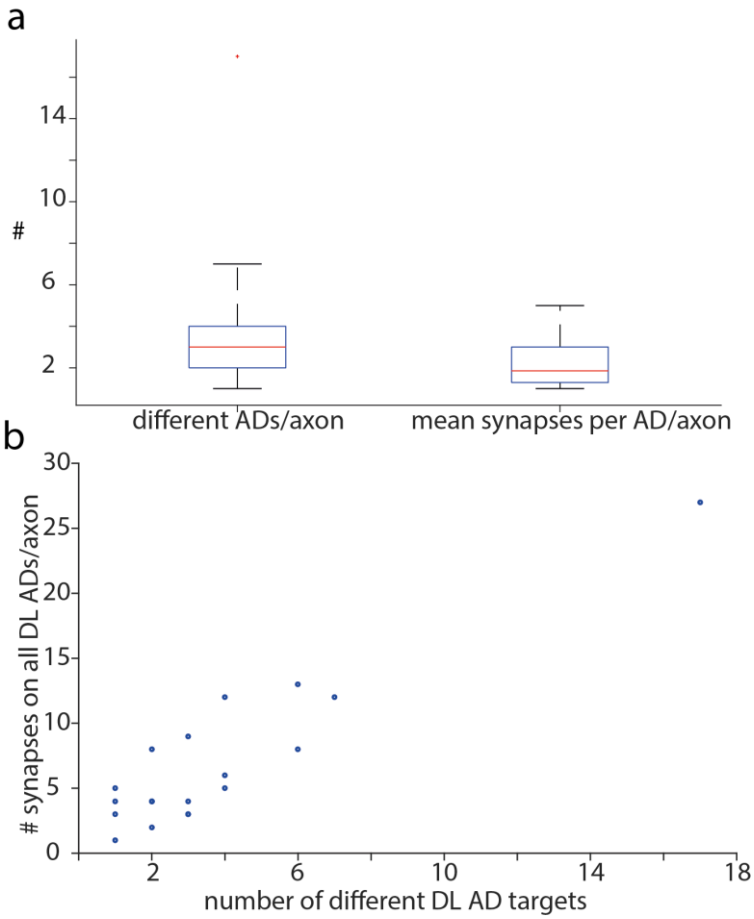

Figure 42: DL AD innervation numbers. (a) Number of different DL ADs innervated by pool of axons seeded from DL ADs, mean number of synapses formed on a single DL AD/single axon. Red dot = outlier. (b) Total number of synapses formed on DL ADs/single axon vs. number of different DL AD targets.

Synapses on ADs were formed throughout all cortical depths with a slight increase in the center part of LIV (Fig. 43, a, Fig. 44, d). The (output) distance between multiple AD innervations was rather small, on average 28.097 ± 5.709 µm (Fig. 43, b).

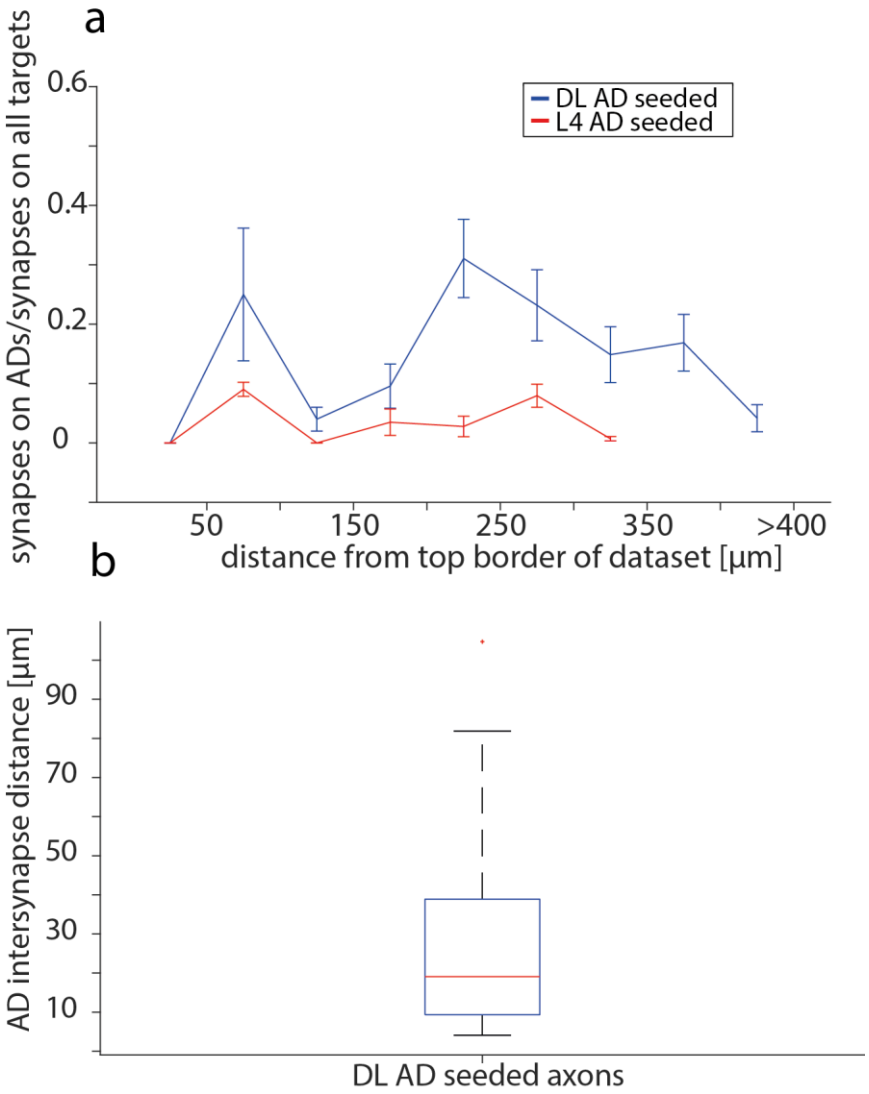

Figure 43: AD innervations relative to cortical depth. (a) Fractional synapses on ADs relative to cortical depth, errorbars = SEM. (b) Axonal path length distance between multiple synapses on the same DL AD target formed by DL AD seeded axons.

Axons that were seeded from LIV star pyramidal apical dendrites poorly innervated any other apical dendrites (mean fractional innervation = 3.62 % ± 1.11 and 1.93 % ± 1.10 for LIV ADs and DL ADs, respectively), but were preferentially targeting somata (mean fractional innervation = 20.45 % ± 2.89) which was not at all the case for the other axon population (mean fractional innervation = 6.54 % ± 2.13).

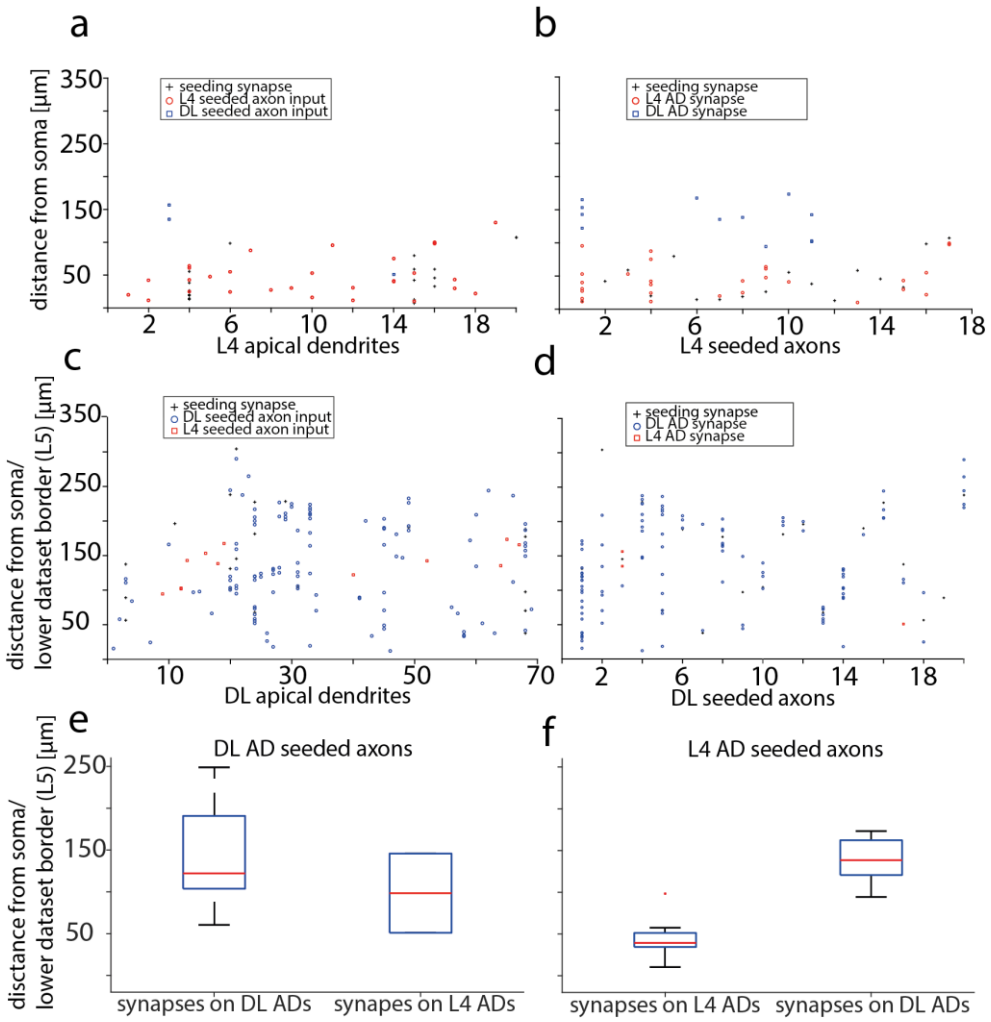

Figure 44: AD innervations relative to soma location. (a) Scatter plot with all synaptic inputs on L4 apical dendrites. (b) Scatter plot with all synaptic outputs formed by axons seeded from L4 apical dendrites, same y-axis scale as in (a). (c) Scatter plot with all synaptic inputs on DL ADs. (d) Scatter plot with all output synapses formed by axons seeded from DL ADs, same y-axis scale as in (c). (e) Mean distance to soma/lower dataset border of all output synapses (n=19, n=2). (f) Mean distance to soma of all output synapses formed by the other axon population (n=11, n=7).

In order to quantify whether apical dendrites receive synaptic inputs at different locations, the relative path length distance of synapses to the soma was measured. In case, the soma was not located within the dataset, the relative distance to the lower dataset border (L5A) was measured. DL ADs got on average targeted by both axon populations at similar locations (mean DL axons = 121.74 ± 10.459 µm, mean L4 axons = 139.85 ± 7.726 µm (Fig. 44, c). L4 ADs got on average targeted more proximally by both axon populations (mean DL axons = 98.39 ± 47.433 µm, mean L4 axons = 50.01 ± 7.927 µm (Fig. 44, a). When considering the output distributions of single axons of both populations (Fig. 44, b, d, e, f),

this result maintained. This was not surprising if one compared the sample geometry with the fractional axonal path length distribution (Fig. 32, Fig. 39, c), as L4 ADs were located in the middle and upper parts of the dataset and hence also comprise limited path length.

Next it was controlled whether fractional innervation preference was really specific or only related to fractional geometrical occurrence of certain structures as claimed by Peters' rule (see II, 4.1). In order to address this question one needs to measure the availability of different postsynaptic targets around these axons. In order to approximate these volumes, five axons preferentially innervating DL ADs and five axons preferentially innervating somata but sparing ADs were picked. Virtual cylinders (r=3 µm) around these axons were created and nodes within the cylinders' volumes were randomly seeded (Fig. 45). The number of sampled nodes was chosen relative to the axonal path length (on average, one node every 5 µm of axonal path length). Then the nodes were uploaded to webKnossos and the structures were classified as we did for the postsynaptic targets of the apical dendrite innervating axons (see IV. 2.2.) (additional structure class: myelinated axon, axon). In case that the random node was located within the axonal volume or a blood vessel, that node was resampled.

In total, 2325 potential postsynaptic targets, of which 902 were axons/myelinated axons, were classified. Similar to the way the fractional output synapses formed by an axon population (see Fig. 41 and III, 3.3.) were analyzed, the fractional availability of targets around an axon population were measured. The number of nodes located within a given postsynaptic target was divided by the total number of nodes sampled (minus the nodes located within an axon). This volume approximation was then compared with the actual output synapses on a given target. As none of the axons established any synapses on glia, but glia appeared to account for a large fractional volume (mean = 25.23 % ± 1.06), glia was considered to be not a real potential target and it was therefore excluded from the availability graph (Fig. 46, black line).

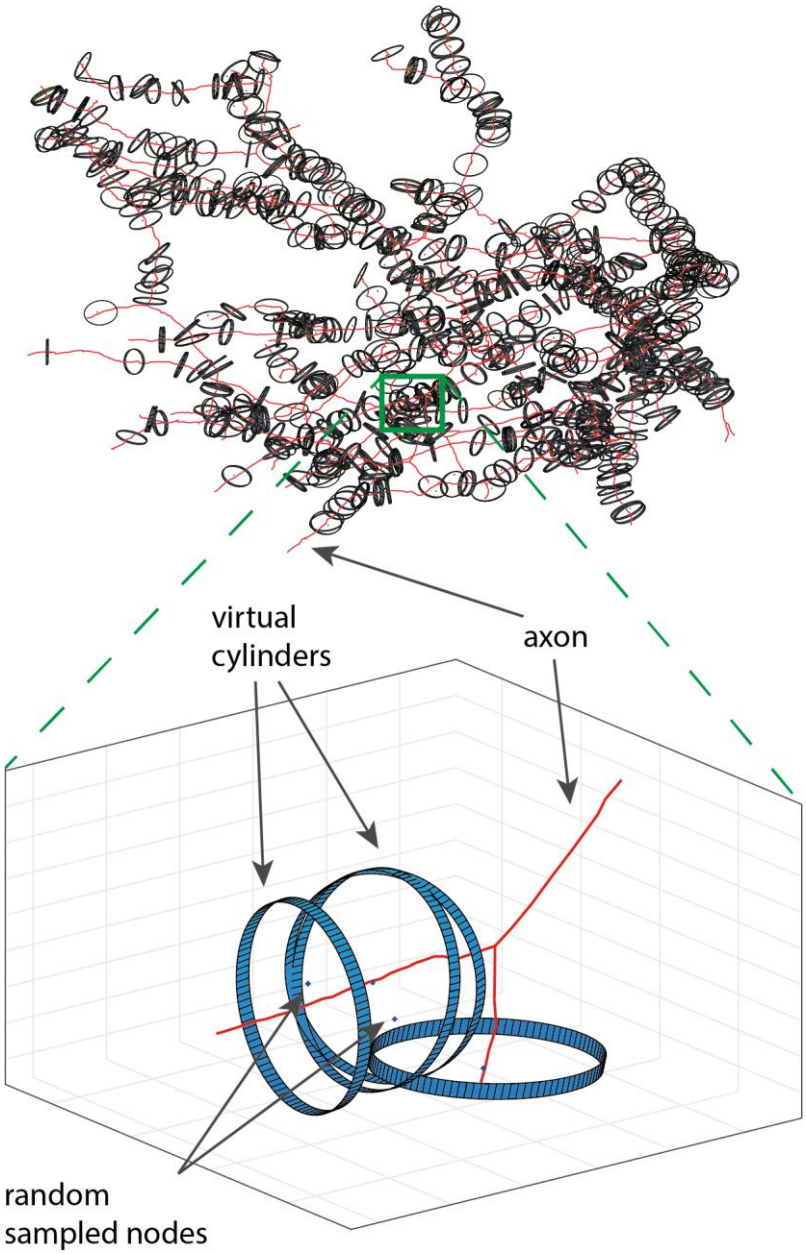

Figure 45: Fractional availability of postsynaptic targets, sampling. Example axon with large fraction of soma targets (=red), surrounded by cylinders along its path (r=3 µm) serving as a random sampling volume.

On average, the five axons that were seeded from DL ADs innervated DL ADs ~double as frequently as target availability/proximity would predict (36.11 % ± 6.95 vs 16.38 % ± 3.65) (Fig. 46, a). In contrast, the availability of somata was higher than the actual synapse formation (11.27 % ± 4.04 vs. 1.91 ± 1.20), indicating potential avoidance of soma innervations, but this difference was statistically insignificant (two sample t-test, $p = 5.71*10^{-2}$).

A similar but less distinct phenomenon was discovered for the five axons that were seeded from L4 ADs which had displayed innervation preference for somata: on average, they innervated somata more frequently as target availability/proximity would predict as well (25.51 % ± 2.95 vs. 16.53 % ± 2.14) (Fig. 46, b). Although, this axon population established less synapses on DL ADs as proximity would predict (1.53 % ± 0.87 vs 6.86 % ± 2.54 %), this difference was insignificant (two sample t-test, $p = 8.31*10^{-2}$).

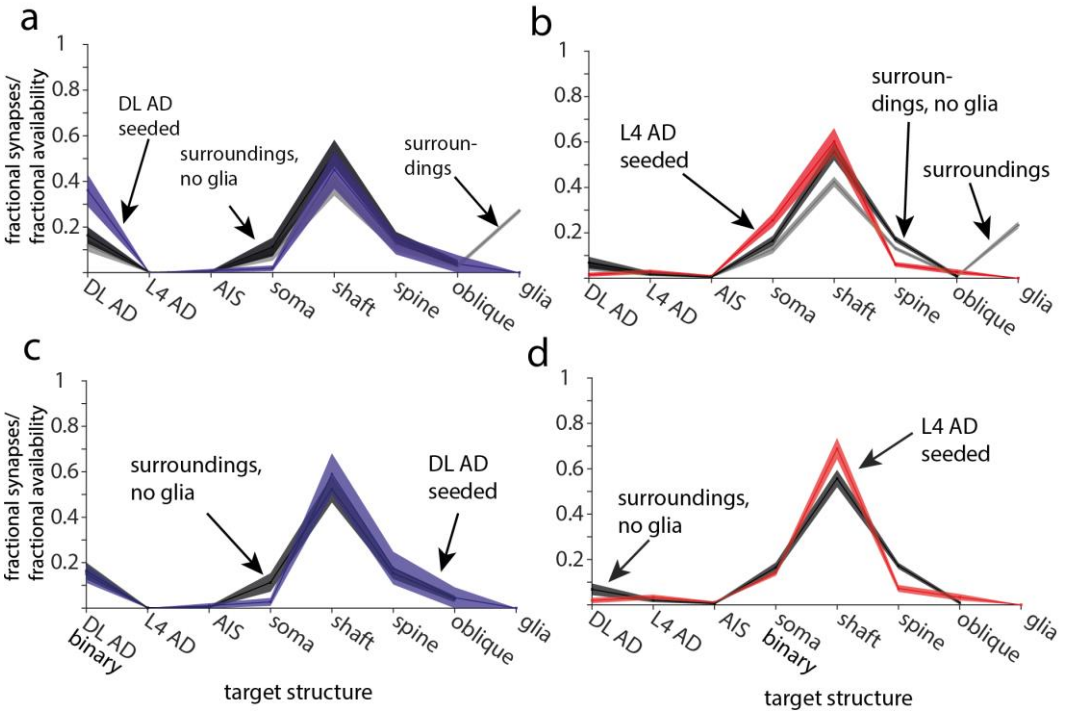

Figure 46: Fractional availability of targets vs synapse formation. (a) Output synapse fraction of five axons seeded from DL ADs (blue) vs their fractional availability (grey/black). (b) Output synapse fraction of five axons seeded from L4 ADs (red) and their fractional availability. (c) Same as (a) but multiple synapses on the same DL AD ignored. (d) Same as (b) but multiple synapses on the same soma ignored. Mean = solid line, shading = SEM.

When the fractional synapses on DL ADs (multiple synapses on the same DL AD/soma accounted as one) were binarized, the fractional availability/proximity matched the measured fractional output synapses (16.38 % ± 3.65 vs. 15.03 % ± 3.87) (Fig.46, c), indicating that binary connections from these axons could be predicted by geometric proximity. Similarly, when the fractional synapses on somata were binarized for the other axon class (multiple synapses on the same soma accounted as one synapse), the fractional availability/proximity also matched the fractional output synapses (16.53 % ± 2.14 vs. 14.03 ± 1.13) (Fig. 46, d).

These different wiring patterns of the two axon classes were also displayed in their axonal morphologies. While trajectories of DL AD seeded axons followed the vertical orientation of the apical dendrites, the other axon class was much more locally and horizontally wired within L4. In this context, it is less surprising that reconstructions lead to the somata for 2/5 axons from this class, while the somata of the DL AD innervating axons were most likely not located within L4.

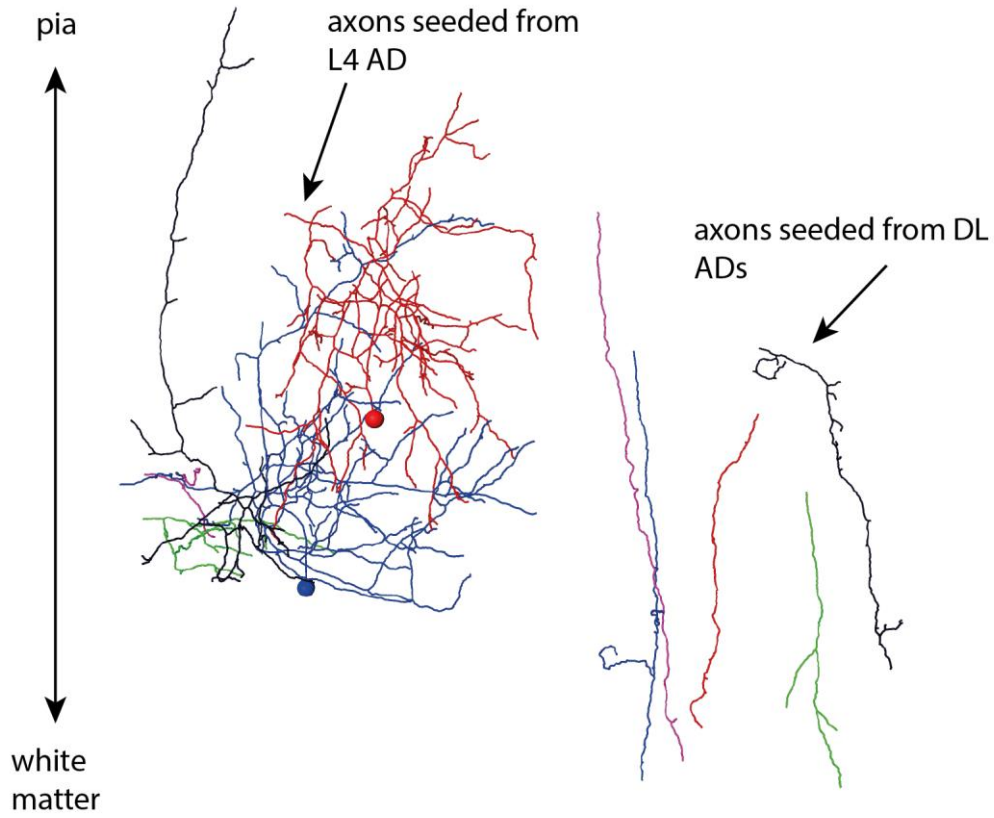

Figure 47: Morphology of 5 soma innervating and 5 DL AD innervating axons. Soma diameter = 10 µm.

3. Soma innervations

As this strong bias towards soma innervation in the L4 AD seeded axon population was rather surprising, the postsynaptic soma targets were investigated and a soma connectome as for the AD innervation (see Fig. 40) was mapped for all previously analyzed 37 axons in order to check whether there might be some underlying soma cell type specificity.

All postsynaptic somata were classified based on their location within the dataset (L3 – L5) and their axonal fiber quality (IN vs EXC). The differentiation between L4 spiny stellate and star pyramidal neurons was achieved by tracing the only potential apical dendrite ascending towards upper layers. IN neurons were identified by their larger and more asymmetric soma shape, as well as their different cytoplasmatic appearance and their usually ascending axon (Fig. 34, 50).

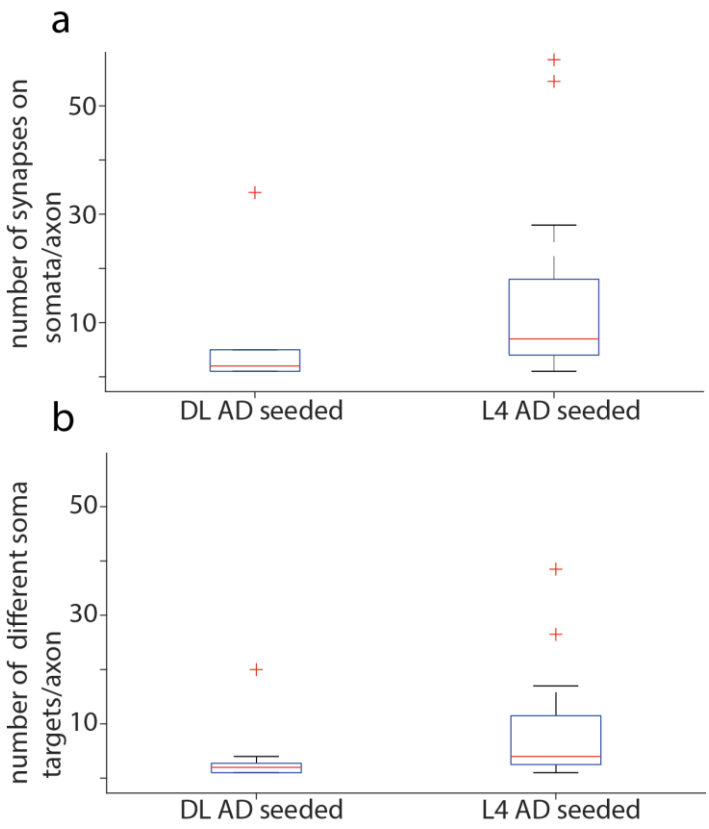

Figure 48: Soma innervation numbers. (a) Number of soma synapses/axon for each axon population. (b) Number of different somata targeted by each axon from each group, red crosses = outliers in both plots.

Unfortunately, 22 excitatory L4 neurons could not be classified as either star pyramidal or spiny stellate cell as they were located at the border of the dataset and/or the potential apical dendrite was running out of the dataset after a very short path length (subsequently referred to as “spiny neuron/L4 sn”). Thus, the 154 identified postsynaptic somata were classified as three L3 pyramidal neurons, 25 L4 star pyramidal neurons, 80 L4 spiny stellate cells, 22 L4 spiny neurons, eleven L5 pyramidal neurons, five L5 inhibitory Interneurons and seven L4 inhibitory Interneurons (Fig. 49, a).

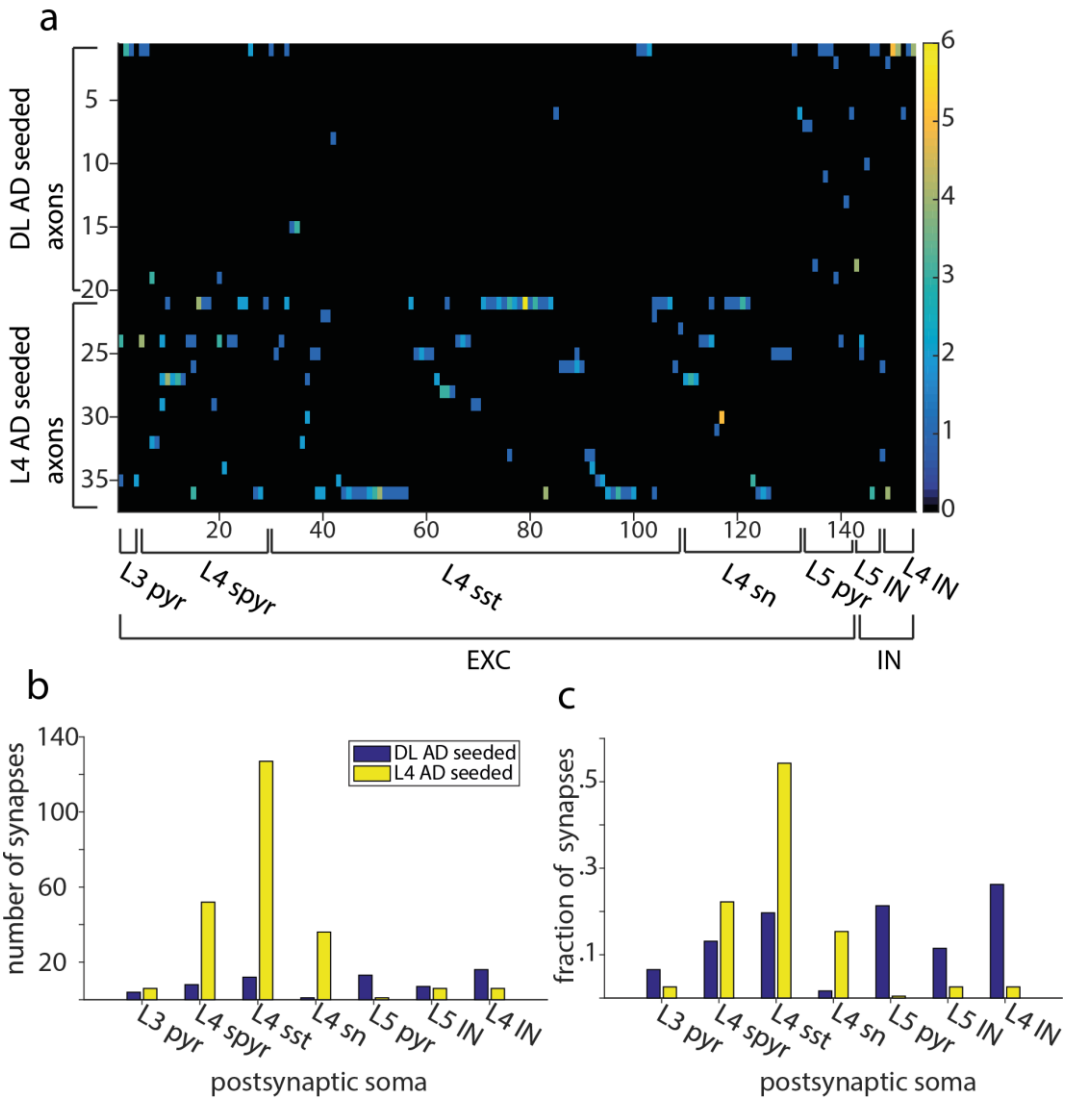

Figure 49: Soma connectome. (a) Connectome of all 37 AD seeded axons vs. all 154 postsynaptic soma targets, grouped for cell type and axonal fiber quality. (b) Absolute distribution of synapses on different soma targets. (c) Relative distribution of synapses on different soma targets, same color code applies as in (b).

While 94.12 % (16/17 axons) of all L4 AD seeded axons were targeting somata, this was the case for only 55 % (11/20 axons) of the DL AD seeded axon class. On average, the L4 AD seeded axons formed 1.68 ± 0.08 synapses on 8.88 ± 2.57 different soma targets. Similarly, the DL AD seeded axon population established 1.56 ± 0.18 synapses, yet on only 3.54 ± 1.67 different somata (Fig. 48,b). This implies that both axon populations usually formed 1-2 synapses per soma and innervated multiple somata (if they innervated somata at all).

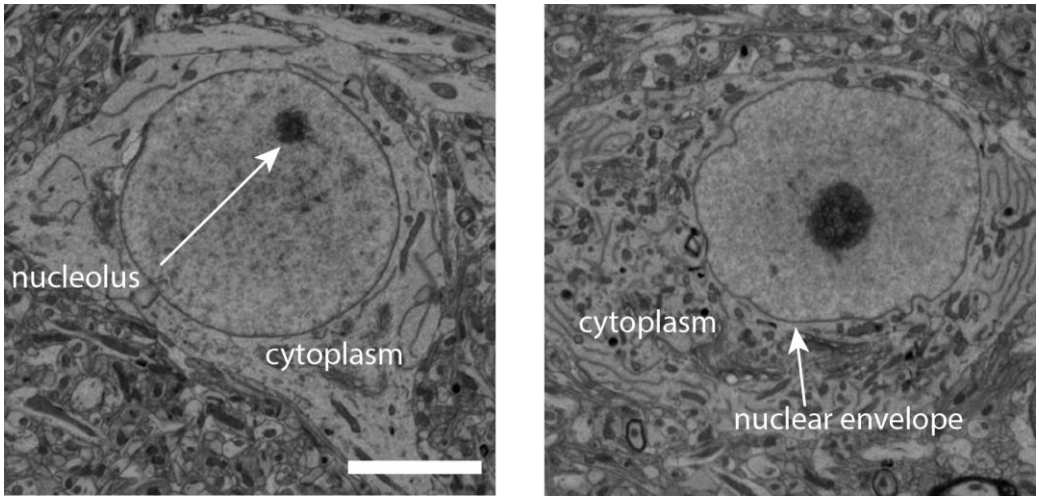

Figure 50: L4 sst and L4 IN example somata. Left: L4 sst soma, right: L4 IN soma, note the very different cytoplasm and somatic shape. Scale bar = 5 µm.

When analyzing the soma connectome (Fig. 49, a) with respect to the postsynaptic soma classes, it appeared striking that the DL AD seeded axon class seems to avoid L4 EXC soma innervation almost completely while the other axon class established many synapses on these cell types. DL AD seeded axons (mainly driven by 1 axon, see first row in Fig. 49, a) seem to target L4 and L5 interneurons much more frequently compared to the other axon group (Fig. 49, b). The lack of L5 pyr and L5 IN innervations in the L4 AD seeded axon population was biased due to missing axonal path length in infragranular layers (see Fig. 39, c). Both axon groups targeted L4 spiny stellate cells more frequently than star pyramidal neurons, which was rather expected, taking into account the numerous distributions of these cell types (86 % to 14 %, see IV 1.). However, L4 star pyramidal neurons were targeted more often than expected by their frequency of occurrence (40.00 % and 29.05 % of the synapses on excitatory L4 neurons, for DL AD seeded and L4 AD seeded axons respectively) (Fig. 49, b). Even if all of the unclassified L4 spiny neurons were spiny stellate cells, the fractional innervation (of all L4 excitatory neurons) for star pyramidal neurons would still

overcome random synapse fraction expected by cell type distribution (38.10 % and 24.19 % for DL AD seeded and L4 AD seeded axons respectively).

4. Apical oblique dendrite innervations

As apical oblique dendrites have been shown to modulate compartment coupling (SCHAEFER et al., 2003), the underlying innervation mechanisms were questioned. Axons innervating apical oblique dendritic shafts and spines were reconstructed and all their output synapses mapped.

4.1. Apical oblique spine innervations

In order to map synaptic inputs onto apical oblique spines, 42 axons were seeded from spine heads belonging to 5 different apical oblique dendrites originating from 2 different apical dendrite trunks. All axons accounted for 12.783 mm path length and established a total of 938 synapses. As it was unclear whether the axons would target any specific spine heads, all postsynaptic spine heads were classified as “oblique spine”, “ad spine” (apical dendrite trunk spine) and “spine” for spine heads either belonging to “regular dendrites” such as spiny neuron dendrites or in case the spine head could not be assigned to its respective dendritic shaft.

All reconstructed axons were identified to be excitatory based on their fractional output synapses (see Table 5, Fig.51, c, d). Postsynaptic targets typical for INs such as soma, ADs, AIS were completely spared (Fig. 51, c, d). On average, this axon population kept innervating its seed structure (apical oblique spine head) with 7.77 % ± 1.28 of all established synaptic contacts. However, the fraction of output synapses formed on apical trunk spines was considerably higher (16.69 % ± 1.74). Eighteen axons established more than every 5^{th} synapse (fractional innervation > 20 %) on a spine head originating from an apical trunk (max = 45 %) (Fig. 51, d). Surprisingly, all of these axons were seeded from oblique dendrites originating from the same apical trunk (subsequently referred to as AD2), while the 5 axons that were seeded from apical obliques belonging to another trunk (subsequently referred to as AD1) did not show this targeting preference (mean = 5.64 % ± 1.63, max = 10.81 %). The 37 axons seeded from oblique spines originating from AD2 alone established 18.18 % ± 2.0 of its synapses on apical trunk spines and 8.63 % ± 1.51 of its synapses on apical oblique spines.

Accumulative, these axons formed 26.81 % of their synapses on apical trunk or apical oblique related spine heads. Taking into account that ~17 % of the spine heads could not be classified as the spine necks could not be traced in some cases, implying that the actual fraction of synapses on these structures might be even higher, this finding indicates a previously not yet discovered excitatory wiring specificity.

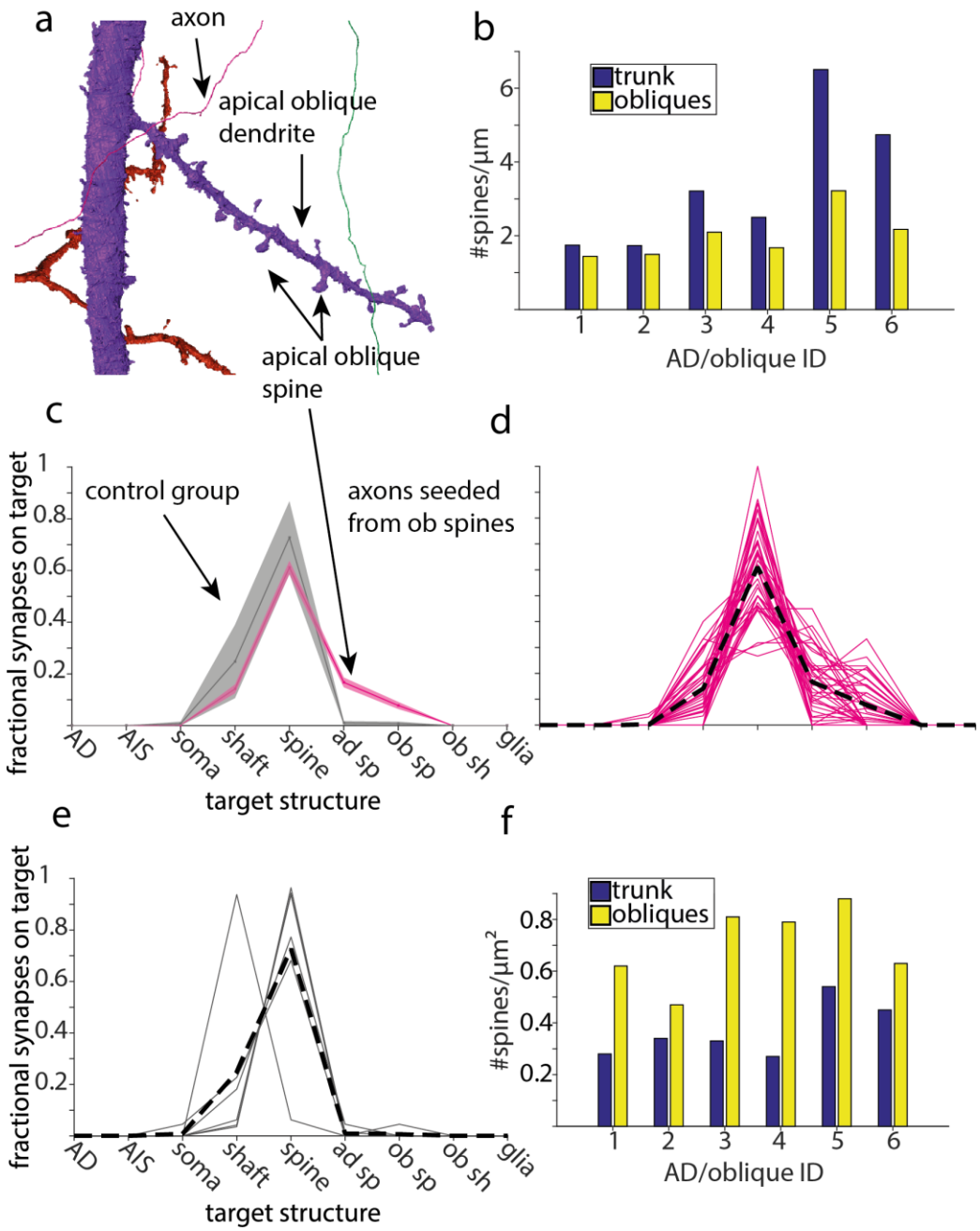

Figure 51: Apical oblique spine innervation. (a) Isosurface of merger mode (III 3.5) traced apical dendrites and obliques, seeding from spines indicated. (b) Spine densities measured for 6 exemplary apical dendrites and their respective obliques. (c) Connectomic phenotype of axon population seeded from apical oblique dendritic spines (magenta) and control group (grey = axon population seeded from L4 sst dendritic spines), solid line = mean, shading = SEM. (d) Single output fractions of the axons in (c), mean indicated as black dashed line. (e) Single output fractions of the axons seeded from L4 sst dendritic spines. (f) Spine density per surface.

As for the inhibitory DL AD specificity, the actual availability of postsynaptic targets was analyzed in order to confirm the excitatory innervation preference for AD related spine heads. The volumes around 10 axons primarily targeting AD trunk spines were approximated.

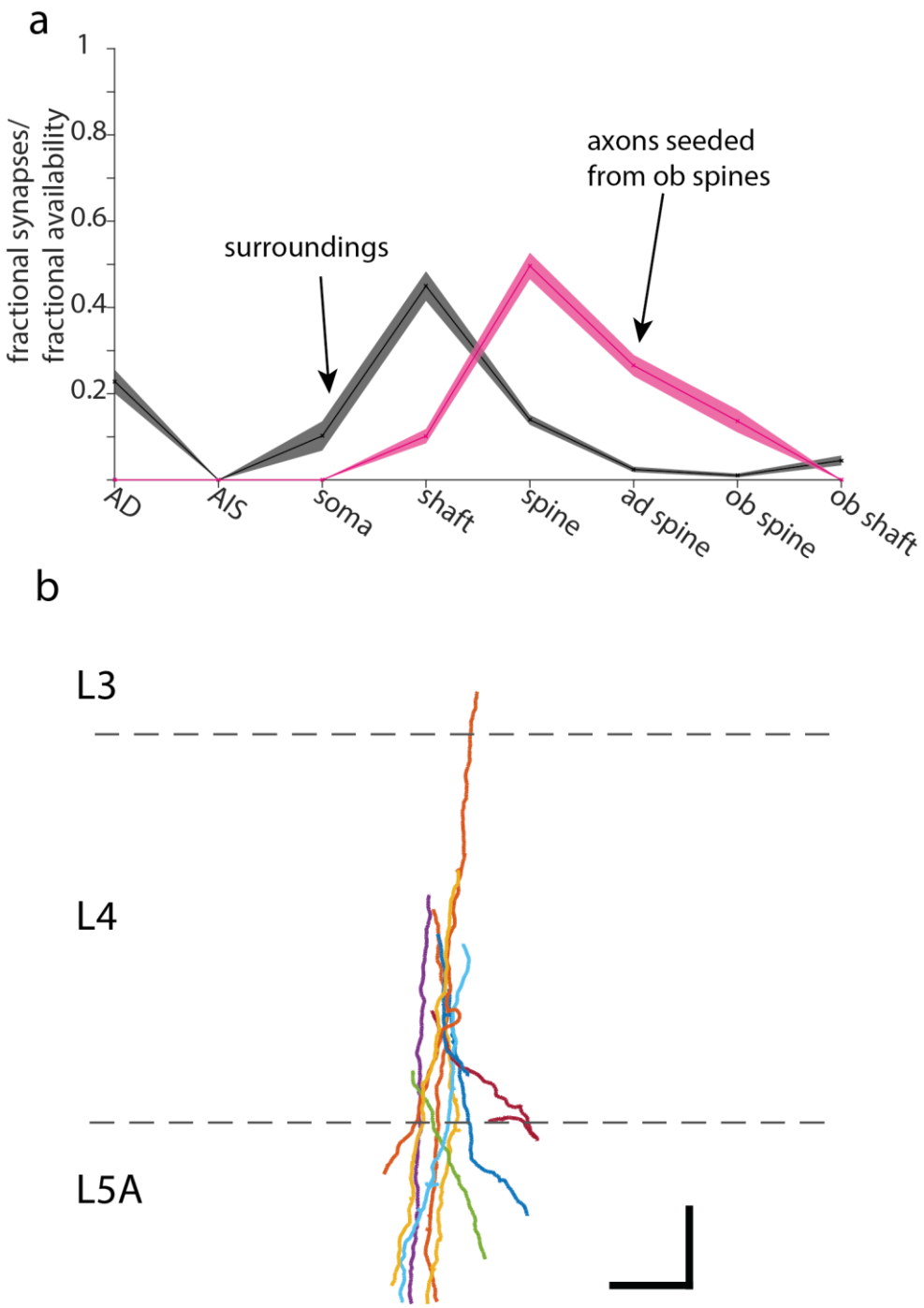

Figure 52: Fractional availability of targets vs synapse formation, excitatory axons. Output synapse fraction of 10 axons seeded from ob spines (magenta) vs. the occurrence of potential postsynaptic targets around these axons. (b) Morphology of the 10 axons. Scale bar = 50 µm.

The 10 axons innervated AD spines on average with 26.54 % ± 2.45 of their synapses. This was ~ 10 times more than the approximated availability of these structures around the axons (on average: 2.44 % ± 0.61) (Fig. 52, a), suggesting that geometric proximity could not predict the excitatory synaptic connections on apical trunk spines. The morphology of these axons (Fig. 52, b) revealed trajectories parallel to apical dendrites, which was also displayed by the large fraction of ADs measured in the availability graph (but not innervations!) (Fig. 55, a). Overall, the volume approximation around these ten axons did not even come close to predict the actual innervation fractions. Hence, it appears that geometric proximity is an unsuitable predictor for excitatory synapse formations.

As these axons appeared to specifically innervate AD trunk spines, it was next controlled whether there might be differences in spinyness of apical trunks and their respective oblique dendrites.

Spines were annotated along six exemplary apical trunks for at least 20 µm dendritic path length and along three oblique segments per trunk for at least 10 µm dendritic path length each. It turned out that AD2 (Fig. 51, b, Table 6 ID 6) was much more spiny (4.73 spines/µm dendritic path length) than AD1 (1.74 spines/µm dendritic path length) (Fig. 51, b, Table 6 ID1). This difference in spine density was also present at the apical oblique dendrites, but weaker than at the apical trunk (36.83 % and 66.36 % spine density present at the trunk and oblique respectively in AD1 compared to AD2). In order to normalize this effect to surface/dendritic diameter differences, each measured dendrite was approximated with a cylinder (h=10 µm, r=mean diameter/2) and the spine density per µm² surface was calculated (Table 6). All apical oblique dendrites carried more dendritic spines on their surface than apical trunk segments (two sample t-test, $p=1.4*10^{-3}$) (Fig. 51, f, Table 6).

Table 6: Spine densities on apical trunks & obliques. AD trunk + oblique diameters measured as described in IV 2.1. +- = SEM. Literature references apply for last four rows, ± = SD, range in brackets.

AD/oblique ID	Spines/µm dendritic path length	Mean Spine head diameter [µm]	Mean diameter [µm]	Surface in µm²/10 µm height	Spines/µm²
#1 trunk	1.75	0.46 ± 0.043	1.82	62.38	0.28
#1 obliques	1.44	0.55 ± 0.063	0.72	23.41	0.62
#2 trunk	1.73	0.59 ± 0.058	1.51	51.02	0.34
#2 obliques	1.50	0.54 ± 0.045	0.96	31.53	0.47
#3 trunk	3.21	0.47 ± 0.053	2.69	95.87	0.33
#3 obliques	2.10	0.50 ± 0.037	0.79	25.85	0.81
#4 trunk	2.50	0.51 ± 0.065	2.65	94.28	0.27
#4 obliques	1.67	0.61 ± 0.067	0.65	21.19	0.79
#5 trunk	6.51	0.51 ± 0.050	3.29	120.27	0.54
#5 obliques	3.32	0.61 ± 0.075	1.10	36.55	0.88
#6 trunk	4.74	0.59 ± 0.057	2.98	105.57	0.45

#6 obliques	2.17	0.60 ± 0.061	1.04	34.23	0.63
Rat visual cortex L5A trunk (LARKMAN, 1991b, 1991a)	2.10 ± 1.29 (0.37-4.82)				
Rat visual cortex L5A obliques	1.28 ± 0.55 (0.36 – 2.46)		1.1 ± 0.4		
Rat visual cortex L5B trunk	6.30 ±1.60 (2.69 – 8.71)				
Rat visual cortex L5B obliques	1.50 ± 0.35 (0.88 – 2.46)		1.3 ± 0.4		

While the spine density difference between AD1 and AD6 trunk stayed almost the same (62.2 %), this effect had vanished for their respective oblique segments (Table 6). The spine densities (per path length) were similar to what has been previously reported in literature for L5 pyramidal neurons (LARKMAN, 1991b) implying that spine densities might allow to distinguish L5A from L5B pyramidal neurons (Table 6). However, the data reported in LM literature showed large variation, came from rat and the present study lacked a positive control due to missing L5B somata.

During this investigation some very large spine heads (e.g. Fig. 53, a) originating from apical oblique dendrites were identified, raising the question about the overall spine head sizes as they matter in terms of synaptic strength. Ten spine head diameters from each apical trunk and ten spine head diameters from their oblique dendrites were measured. Each spine head diameter was averaged from three orthogonal lines' (each 3 dimensions) path lengths approximating the spine

head's volume. On average, the apical trunk spine heads spanned 0.52 µm (range: 0.24 – 0.93), the apical oblique spine heads 0.57 µm (range: 0.25 – 1.09) (Table 6, Fig. 53, b). Although, this difference was statistically insignificant (two sample t-test, $p=1.59*10^{-1}$), large spine heads (e.g. Fig. 53, a) originating from apical trunks have not been encountered by the author.

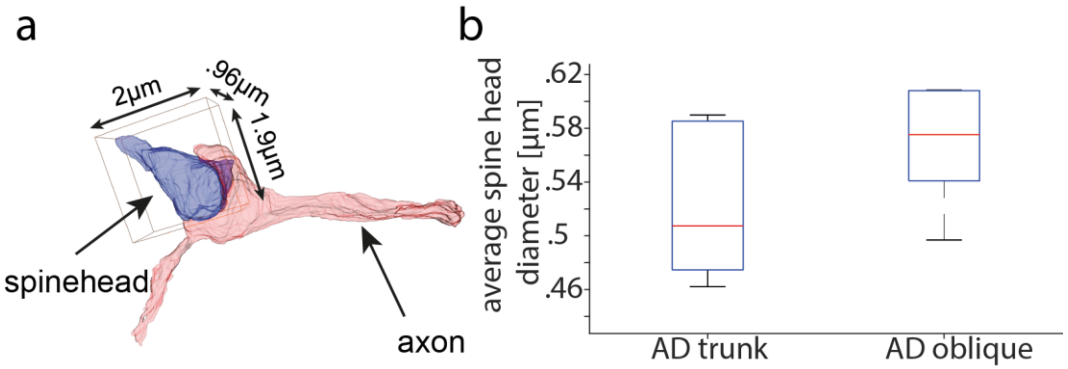

Figure 53: Spine head diameter. (a) Isosurface of volume traced exemplary super large spine head + innervating axon. (b) Averaged spine head diameter measured for apical trunks and obliques.

The trajectories of five axons could be reconstructed back to their originating soma (Fig. 54). Based on soma location, dendritic morphology and synaptic output target fractions three neurons were classified as L4 spiny stellate neurons, one as L4 star pyramidal neurons and one as L3 pyramidal neuron. Almost all other reconstructed axons were vertically oriented, some could be traced back to L3 (note the similarity between the two axons marked with asterisks in Fig. 54), the others were unfortunately running out of the dataset within L4.

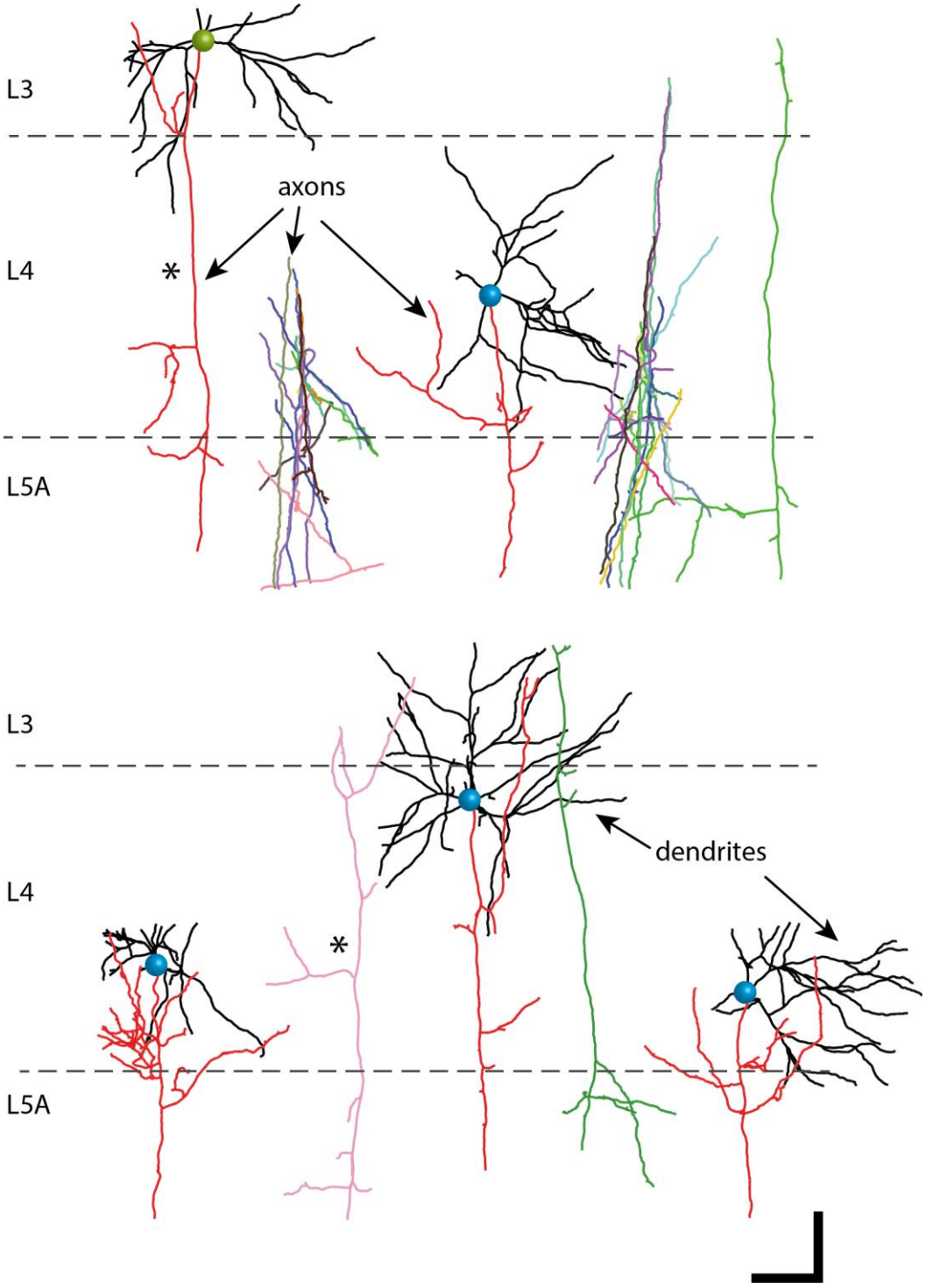

Figure 54: Apical oblique spine seeded axons. Dendrites plotted in black, axons in red. Other axons without identified soma plotted in random colors. Asterisks marks two very similar axons. Lateral shift applied for better visualization, scale bar = 50 µm.

4.2. Apical oblique shaft innervations

A total of 468 apical oblique dendrites from the previously analyzed deeper layer apical dendrite population (L5A + L5B neurons) (see V 2.1.) were reconstructed. On median, each apical dendrite carried 2 apical oblique dendrites (min = 0, max = 9) (Fig. 55, b).

In order to investigate dendritic shaft innervations, a total of 18 axons from five different apical oblique dendrites originating from two different apical trunks (carrying 2 & 7 apical obliques in total, respectively) were seeded (Fig. 55, a, b). As for previously described analyses (IV, 2.3.), all the synapses along the axons were annotated and the postsynaptic targets identified. The axons totaled a path length of 4.765 mm and established 238 synapses.

All axons were exclusively seeded from synapses on dendritic shafts. Surprisingly, it turned out that on average, these axons primarily targeted dendritic spines (51.12 % ± 8.65), indicating excitatory fiber qualities (see IV 1.1) (Fig. 55, c).

When looking at the single axonal output fractions (Fig. 55, d), it appeared that half of the axons (9/18) that were seeded from apical oblique dendritic shafts were excitatory and the other half inhibitory, based on their spine and shaft target fractions.

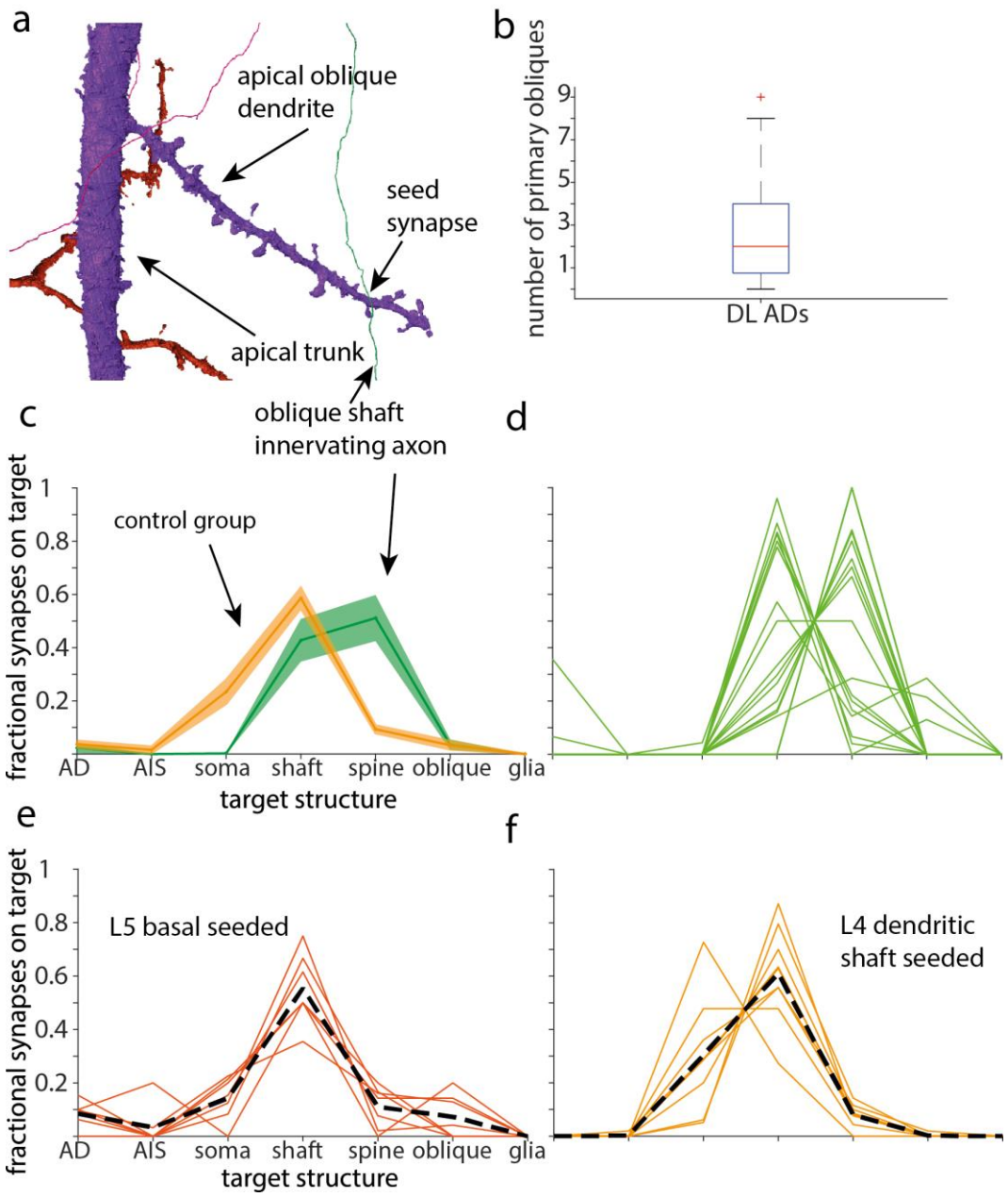

Figure 55: Apical oblique shaft innervation. (a) Isosurface of merger mode (III 3.5) traced apical dendrites and obliques. (b) Distribution of primary oblique dendrites over all DL ADs. (c) Connectomic phenotype of axon population seeded from apical oblique dendritic shafts (green) and control group (orange = axon population seeded from L4 sst dendritic shafts and L5A basal dendrites), solid line = mean, shading = SEM. (d) Single output fractions of the axons in (c). (e) Single output fractions of the axons seeded from L5 basal dendrites, mean indicated as black dashed line. (f) Single output fractions of the axons seeded from L4 sst dendritic shafts. (e, f) = Orange plot in (c).

In order to control this rather unexpected additional excitatory input on dendritic shafts, an axonal control group was reconstructed.

Seven axons were seeded from three different primary basal dendrites originating from two different L5A pyramidal neurons accounting for 1.500 mm axonal path length and establishing 138 synapses (Fig. 55, e). In addition, nine axons were seeded from four different dendritic shafts originating from three different L4 spiny stellate cells (Fig. 55, f), accounting for 2.323 mm axonal path length and forming 332 synapses. Neither the averaged output phenotype (Fig. 55, c) (mean = 9.32 % ± 1.49) nor any of the 16 axons seeded in the control group (Fig. 55, e, f) (max = 20 %) came even close to the fractional synapses established on spine heads by excitatory neurons. Hence, apical oblique dendrites appear to receive additional excitatory innervations on their dendritic shafts, which could not be found either on L5A basal dendrites or L4 spiny stellate dendritic shafts.

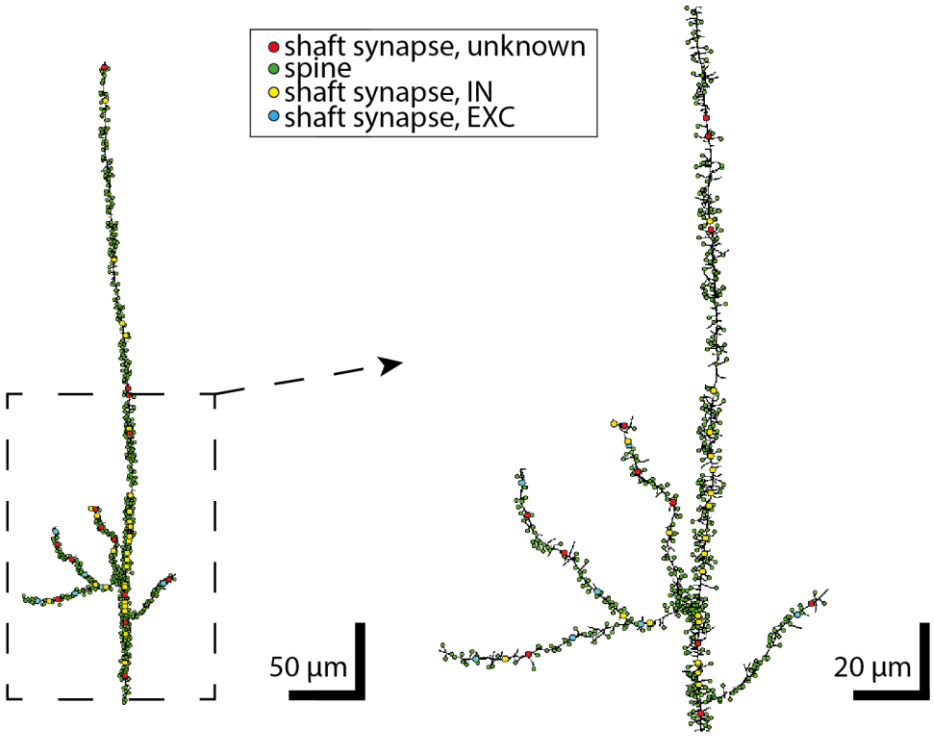

Figure 56: Dendritic shaft inputs on exemplary apical dendrite and its obliques. Note the numerous excitatory shaft innervations on the apical oblique shafts. Red synapses = formed by axons which could not be categorized as IN/EXC due to lack of reconstructed synapses/axonal path length (running out of the dataset).

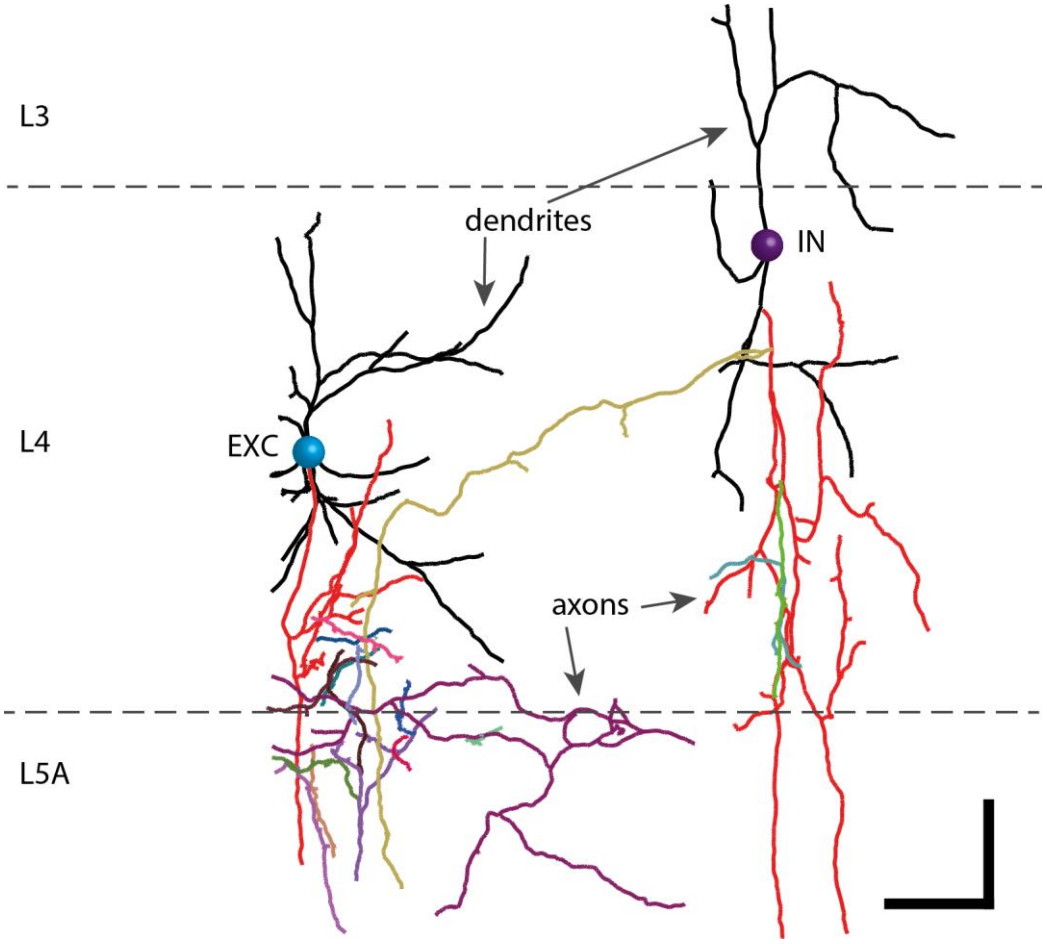

Figure 57: Apical oblique dendrite shaft innervating axons. Dendrites of the two identified neurons plotted in black, their axons plotted in red. Other axons without identified soma plotted in random colors. Lateral shift applied for better visualization, scale bar = 50 µm.

Two axons were reconstructable to their originating soma (Fig. 57). One of these neurons was classified as a L4 spiny stellate cell and the other one as a L4 Interneuron (presumably bipolar cell) based on dendritic and somatic morphology as well as axonal postsynaptic target fractions (Fig. 57).

V. DISCUSSION

Constituting 70-85 % of all neurons, pyramidal neurons are the dominant cell type in cerebral cortex. L5 pyramidal neurons receive both information from thalamic feed-forward streams and long-range cortical feedback at their distal apical tuft. The goal of this study was to provide first cellular level insights on the innervations of apical and apical oblique dendrites. The study was in particular focused on the question whether these structures receive specific synaptic inputs that exceed random wiring principles. These distinct morphological structures, displayed by all excitatory L5 neurons, most likely endow these neurons with the ability to integrate long range synaptic inputs with sensory afferences (in case of barrel cortex) shaping cortical output. The underlying mechanism of cortical signal computation and processing might be crucial to understand general neocortical operating principles.

Apical dendrites comprise two compartments, which have been electrophysiologically shown to endow L5 pyramidal neurons with the previously described signal integration mechanisms. One compartment is located at the distal apical tuft: the Ca^{2+} spike initiation zone. The other compartment is at the intermediate/proximal part of the apical dendrite: The majority of apical oblique dendrites originate within the upper L5A and L4 area and have been shown to reduce the compartment coupling for coincidence detection. This relation of functional/electrophysiological features (coincidence detection) and structural peculiarity might be fundamental for cortical circuit organization. In this context, this work yielded to address the so far unresolved questions whether apical dendrites receive specific/non-random inhibitory/excitatory tuning and how apical oblique dendrites could modulate the previously described compartment coupling mechanism in L5 pyramidal neurons on a cellular level. In general, it still remains unclear how brain circuitries are organized on a synaptic level. The null hypothesis of neuronal circuit organization states random wiring principles with synapse formation based on geometric proximity (Peters' rule). In contrast, the working hypothesis would assume specific innervations driven by other mechanisms than proximity/apposition of two neuronal processes.

In order to address these questions, the novel approach of single synapse

resolution, electron-microscopy based connectomics was used. This work presents promising biological results and provides an overview on this still highly developing field.

Despite recent developments which massively speed up data acquisition (e.g. Boergens et al., unpublished), it is still challenging to generate large volume 3D SBEM data containing complete neuronal circuits. The acquired 3D EM dataset spanned 424 x 428 x 84 µm³ and represents one of the largest datasets of this kind worldwide, enabling systematic innervation analyses on the latter described compartment of the apical dendrites within L4/L5A.

1. Apical trunk innervation

A large pool of apical dendrites was reconstructed in order to investigate whether apical dendrites receive cell type specific inhibition on their trunks. In order to address this question, all apical dendrites were classified, which was challenging in the case of infragranular neurons with apical dendrites passing through the dataset.

In an attempt to further distinguish those apical dendrites originating from deeper layers the diameter and spine densities of a small subset of apical dendrites was measured. It appeared that two apical dendrites were much larger than the average diameter measured for L5A and L6 neurons. Whether this feature could serve to distinguish L5B neurons requires further investigation with an even larger dataset. Spine density measurements for six apical dendrites revealed that two apical dendrites appeared spinier than the other four, which could not be completely explained by the larger diameter of the two apical dendrites. The spine densities (per path length) reported for the six apical dendrites were similar to what has been previously reported in literature for L5 pyramidal neurons (LARKMAN, 1991b) (Table 6). Since LM could not precisely measure the apical diameter, the measurements reported in LM literature were only done relative to dendritic path length (lack of surface) and the range of these observations was pretty large. Hence, even though spine density could serve as a differentiation feature between L5 excitatory neurons, the deeper layer apical dendrites were not further classified due to lack of a L5B control population as well as the previously described caveats (range, SD) and the fact that the LM data came from another species and cortex. In this context, one also has to point out that while spine density

measurement is rather “cheap” in labeled LM data, it is very time consuming and therefore costly in manually annotated 3D high resolution EM data.

While LM data only allows investigation of large, labeled boutons apposed to neuronal processes, which requires sparse labeling due to limited spatial resolution, the acquired EM data allows to precisely resolve (sometimes small) chemical synapses on postsynaptic targets. Axonal reconstructions were started with seed synapses from L4 star pyramid apical dendrites and from deeper layer apical dendrites with the question to what fraction of their total synapses these axons might continue innervating these structures. All the output synapses of the 37 axons were annotated and the postsynaptic structures classified, resulting in an output profile/axonal phenotype which was averaged over each of the two axon classes.

As expected, all reconstructed axons were classified as inhibitory interneurons based on their postsynaptic targets. The axon population that was seeded from deeper layer apical dendrites established 19.01 % ± 3.58 of all its annotated output synapses onto deeper layer apical dendrites, while sparing L4 star pyramidal apical dendrites almost completely (0.36 % ± 0.28). The axon class that was seeded from the latter kind of apical dendrite (L4 star pyramid) appeared to rather innervate somata than apical dendrites at all (soma = 20.45 % ± 2.89, 3.62 % ± 1.11 and 1.93 % ± 1.10 for L4 ADs and DL ADs, respectively). One has to point out that this way of seeding introduces a certain noise which will most likely vanish with very high numbers of reconstructed axons. This is caused by the fact that even axons that target e.g. apical dendrites very rarely/occasionally could be included in the axon population seeded from this structure, adding a false negative noise to potential wiring specificities of axon classes innervating these structures.

When considering this DL AD innervation preference present in the DL AD seeded axon population but missing completely in the other axon population, the following questions came up: 1.) is the distribution of axonal path length for both populations such that they could both target each type of AD – in order to address this question, the fractional path length for all axons relative to cortical depth was measured initially (Fig. 39, c). Ten axons from the initial pool of 47 seeded axons had insufficient path length within L4 and were therefore excluded from all subsequent analyses.

2.) Is there an innervation preference relative to dendritic path length distance from the soma (e.g. innervation hotspots?!), which might exclude L4 ADs to be targeted by the DL seeded axon population? DL ADs got on average targeted by both axon populations at similar locations (mean DL axons = 121.74 ± 10.46 µm, mean L4 axons = 139.85 ± 7.73 µm) (Fig. 44, c). L4 ADs got on average targeted more proximally by both axon populations (mean DL axons = 98.39 ± 47.43 µm, mean L4 axons = 50.01 ± 7.927 µm) (Fig. 44, a). When considering the output distributions of single axons of both populations (Fig. 44, b, d, e, f), this result maintained, which was not surprising if one compared the sample geometry with the fractional axonal path length distribution (Fig. 32, Fig. 39, c). The results could indicate one reason why DL AD seeded axons spare L4 ADs, but it does not explain the lack of any AD targeting preference for the other axon population. Although, the exact distance for most DL ADs synapses from their soma was unknown apical dendrite path length for the L4 ADs was very limited, both axon populations were multiply involved in proximal and distal synapse formations indicating their potential occurrence.

3.) Is fractional innervation preference related to fractional geometrical apposition of pre- and postsynaptic processes as claimed by Peters' rule (see II, 4.1)? This is still one of the key questions about neuronal circuit organization. In order to fully address this question one would need dense reconstructions of large neuronal volumes. As manual skeleton reconstructions and especially volume contouring are prohibitively time consuming, that could only be done with fully automated volume reconstructions at feasible time scales. While such effort on a smaller dataset with less image aberrations (which are very critical for automated algorithms) is currently made in the Helmstaedter laboratory (Berning, Boergens et al., in preparation), the availability of postsynaptic targets in a given volume around a given axon was approximated with a different approach. A set of axons that preferentially innervated DL ADs and a set of axons that preferentially targeted somata were picked. Virtual cylinders with a 3 µm radius around these axons were created and one node every 5 µm of axonal path length (at least 50 nodes per axon) was sampled within this cylindrical volume around the axon. By classifying all the neuronal processes the nodes were located, the neuropil surrounding a given axon was approximated, estimating the potential availability of postsynaptic targets. Axonal specificity should show up as overrepresentation

of innervated postsynaptic targets as predicted by geometrical proximity, while underrepresentation of innervated postsynaptic targets would imply avoidance of certain potential postsynaptic targets. If neuronal circuits were wired randomly, the actual innervation of postsynaptic targets should match their availability. Although, a very strict interpretation of Peters' rule might account for glia as an available target, glia was excluded from the analyses as no glia targeting axon was identified.

On average, the axons that were seeded from DL ADs innervated DL ADs ~double as frequently as target availability/proximity would predict (36.11 % ± 6.95 vs 16.38 % ± 3.65) (Fig. 46, a). In contrast, the availability of somata was higher than the actual synapse formation (11.27 % ± 4.04 vs. 1.91 ± 1.20, implying potential avoidance of soma innervations, but this difference was insignificant (two sample t-test, $p = 5.71*10^{-2}$). This effect was similar but less distinct for the other axon class: soma target fraction = 25.51 % ± 2.95 vs. 16.53 % ± 2.14) (availability). Not only different wiring patterns but also distinct axonal morphologies were found for the two axon classes. While trajectories of DL AD seeded axons followed the vertical orientation of the apical dendrites, the other axon class was much more locally and horizontally wired within L4 (Fig. 47). Based on their axonal and dendritic morphology the two identified neurons were classified as L4 basket cells.

Binarizing the connectomes (= multiple synapses on an AD/soma get accounted only once) of both axon classes adjusted these effects such that actual synapse fraction matched the fractional target availability. This finding is in accordance with the analysis on average synapse numbers established on apical dendrites and somata reported in this work (2.14 ± 0.26 synapses on DL ADs, 1.68 ± 0.08 synapses per soma) (Fig. 42). The lack of L4 AD innervation was well aligned to the very small representation of these structures in the volume around both axonal classes. Hence, the data suggests that DL ADs receive specific inhibitory innervation by axons that only sparsely innervate somata, while another inhibitory axon class seeded from L4 ADs does only sparsely innervate apical dendrites but targets preferentially somata. Geometric proximity might predict binary synapse formation but not the strength (synapse numbers) of a connection between two synaptic partners for both axon classes. One potential explanation might be that these inhibitory axons initially form rather random synapses based on geometric

apposition but the formation of multiple synapses on a given target is non-random and specific. The innervation domains of the two axonal classes were also displayed in their morphology.

2. Soma innervation

Strikingly, almost all (94 %) axons that were seeded from L4 ADs and only ~ half (55 %) of the axons that were seeded from DL ADs were targeting somata. This raised the question whether the soma innervating axons might follow certain wiring rules such as cell type specificity/bias as well. It appeared that DL AD seeded axons target L4 and L5 INs more frequently than the other axon class, but this effect was mainly driven by one axon and most of the L4 AD seeded axons couldn't innervate L5 INs due to lack of infragranular path length. All axons targeted primarily L4 spiny stellate cells and L4 star pyramidal neurons, which was not surprising given the dataset location (centered in L4) and the fractional occurrence of EXC and IN neurons. However, L4 star pyramidal neurons appeared as an overrepresented target (40 % and 29 % of all L4 excitatory targets for DL AD seeded and L4 AD seeded axons respectively) assuming a spatially homogeneous distribution of cell types within L4 and accounting for the fractional occurrence of this cell type (14 % measured for this dataset (n=40), 20-25 % in LM literature (rat)). Despite some L4 spiny neurons could not be classified as they were located at the very edge of the dataset, assuming these L4 spiny neurons were spiny stellate cells, the fractional innervation (of all L4 excitatory neurons) for star pyramidal neurons would still overcome random synapse fraction as predicted by cell type distribution (38.10 % and 24.19 % for DL AD seeded and L4 AD seeded axons respectively). Yet, it is unknown whether excitatory L4 neurons are equally distributed within L4 and one would need to classify all neurons within a dataset to exclude geometrical biases.

3. Apical oblique shaft innervation

Apical oblique dendrites have been electrophysiologically shown to modulate coincidence detection (SCHAEFER et al., 2003) and were thus subject of cellular level analyses in this work, too. It is known that the fraction of proximal oblique dendrites positively correlates with coupling (=the more proximal oblique dendrites the lower the threshold for Ca^{2+} spikes in the distal tuft) while an increase in distal oblique dendrites reduces coupling. The underlying mechanisms are currently interpreted as the following: 1.) Additional distal oblique dendrites increase the capacitive load for the back-propagating action potential, proximal oblique dendrites are pre-charged by current injection/stimulus. 2.) The initial threshold for somatic/axonal AP initiation is increased by proximal oblique dendrites. The additional charges present in the back-propagating APs increase coupling. As all this evidence was acquired with electrophysiology introducing charges itself, the underlying cellular mechanisms remained unsolved.

The acquired dataset was well aligned to the proximal portion of apical oblique dendrites allowing investigation of underlying cellular resolution innervation mechanisms potentially triggering the suggested mechanisms. In order to resolve these innervations, axons from apical oblique dendritic shafts were seeded, reconstructed and their synaptic outputs profiled.

Surprisingly, two almost perfectly separated axon classes were found: Based on their fractional target distribution, about half the axons were classified as excitatory and the other half inhibitory neurons. This was rather surprising as dendritic shafts are known to receive primarily inhibitory inputs. In order to control whether these additional excitatory shaft inputs are apical oblique specific, an axonal control group was seeded from L4 spiny stellate and L5A basal dendritic shafts.

Not a single excitatory axon innervating dendritic shafts could be identified in the control group. When all inputs on a single apical dendrite including its obliques were exemplary mapped, no excitatory synapses on the apical trunk were found either (Fig. 56). This finding might be a key feature endowing proximal apical oblique dendrites to increase coupling. Additional excitatory shaft innervations could pre-charge these dendrites such that they facilitate the occurrence of back-propagating action potentials.

Two axons could be traced back to their originating soma. One of these neurons was classified as L4 spiny stellate cell and the other one as L4 bipolar IN. Unfortunately, all the other axons ran out of the dataset, prohibiting identification of their cell type. Hence, the reported data could unfortunately not yet reveal a clearer picture about which excitatory neurons provide these additional excitatory inputs.

4. Apical oblique spine innervation

As the finding of additional excitatory shaft innervations was rather unexpected, it brought up the question whether the apical oblique dendrites and the apical trunk differ in spine densities and which axons might innervate these spines. Mapping the spine distributions in 2D (relative to dendritic path length) implied that apical trunks were spinier than their oblique dendrites. However, when the spine distribution was normalized to dendritic surface (3D, spines/µm²), it turned out that the oblique dendrites in fact carry even more spines than the trunk. Randomly picked spines were on average similar sized for apical trunk and apical oblique dendrites, but some huge outlier spines originating from apical oblique dendrites were detected which could not be found at the trunk. These large spine heads might be interesting with respect to synaptic strength and might be further studied in future fully automated volume reconstructions.

In order to reveal whether apical oblique spine heads receive specific synaptic inputs, a set of axons innervating these structures was seeded. All reconstructed axons were classified as excitatory neurons. Surprisingly, it was found that on average (and some axons in particular) this axon class targets spines originating from apical trunks rather frequently (16.69 % ± 1.74). These axons formed 26.81 % of their synapses on apical trunk or apical oblique related spine heads. Given the fact that ~17 % of the target spine heads could not be attached to their respective dendritic shaft as they became too thin (s/n not sufficient in some areas), this number might be even higher, suggesting potential, so far undescribed excitatory specificity.

In order to check whether this innervation preference could be predicted by geometric apposition or whether these innervations are specifically targeted, the

availability of postsynaptic targets in a given volume around a set of 10 axons was approximated with the same method as described in IV 2.3. The 10 axons innervated ad spines on average with 26.54 % ± 2.45 of their synapses. This was ~ 10 times more than the approximated availability of these structures around the axons would predict (on average: 2.44 % ± 0.61). The morphology of these axons revealed trajectories parallel to apical dendrites, which was also displayed by the large fraction of ADs measured in the availability graph (but not innervations!). Overall, the volume approximation around these ten axons did not even come close to the actual innervation fractions, suggesting that geometric apposition alone could not predict excitatory innervations.

The axonal paths of five neurons could be traced back to their originating soma. Three neurons were classified as L4 spiny stellate neurons, one as L4 star pyramidal neuron and one as L3 pyramidal neuron. Almost all other reconstructed axons were vertically oriented, some could be traced back to L3, implying that the majority of presynaptic partners might be L3 and L4 excitatory neurons.

Even though, due to their location it appears likely that apical oblique spines also receive thalamic inputs within L4, not a single axon was considered likely to originate from thalamus. Thalamic fibers are known to primarily target spine heads and form multi target boutons (RODRIGUEZ-MORENO et al., 2017), which in case of the latter criterion was not found in any of the analyzed axons.

5. Conclusions and outlook

Associating sensory perception from the environment with cortical feedback mechanisms appears to be a fundamental and outstanding function of the mammalian neocortex. For the first time, this work provides cellular resolution insights on the inhibitory and excitatory modulation of the neurons most likely involved in this process. The study shows specific inhibitory innervation of L5 pyramidal neurons' apical dendrites, which is only partially predictable by the geometric proximity of the involved structures. Specific innervation of these apical trunks is of great importance to prevent constant cortical bursting caused by unregulated back-propagation-activated calcium firing. This specificity was further enhanced by the trajectories of these axons which were found to run parallel to apical dendrites. In addition, the reported data suggests that apical oblique dendrites might influence the coupling mechanism via additional excitatory inputs on their dendritic shafts. For the first time, specific excitatory innervations of L5 apical trunk spine heads were found, which were not at all predictable by geometric apposition alone. These findings are contradictive to random wiring principles as postulated by Peters' rule and suggest specific synapse formation that overcomes geometric apposition.

Volume electron-microscopy has become a powerful tool to provide single-synapse resolution structural information of neuronal circuits. The acquired dataset allowed systematic investigation of the proximal apical dendrite compartment. As the technique of high resolution volume EM is still highly developing, mapping larger neuronal volumes within reduced time scales with fully automated reconstructions will become possible, so that layer 5 pyramidal neurons in its entirety will be subject of further connectomic analyses in the future and further insights on the outstanding mechanism of compartment coupling and its role in cortical processing will be gained. Control experiments to verify the reported findings in a second dataset are indicated, wiring specificity comparisons across species, especially to rat are warranted.

VI. SUMMARY

Retrieving information about the environment is fundamental for all species. While human beings primarily rely on visual perception, rodents like mice and rats gain the majority of sensory inputs via tactile information (VINCENT, 1912; DIAMOND et al., 2008). Deflections of individual whiskers get detected and projected to the somatosensory cortex one. These stimuli get individually processed in a highly specified sub-region of this neocortical area, the so-called barrel cortex. It has been of great interest over the last decades how single afferent stimuli derived from individual whiskers get processed in well circumscribed circuits, called barrels (FELDMEYER et al., 2013). One particular question in this context, which has been functionally approached extensively, is how neurons manage to associate external perceptions like whisker stimuli with intrinsic experiences or inputs from other cortical areas leading to cortical output and ultimately precise behavior (LARKUM, 2013). L5 pyramidal neurons have been shown to be endowed with peculiar electrophysiological and structural properties making them a promising candidate to fulfill this task. These neurons are considered to represent the cortical output neurons. In contrast to other cells, these neurons display a second dendritic AP initiation zone at their distal apical dendrite compartment. The occurrence of subthreshold EPSPs together with back-propagating APs trigger Ca^{2+} spikes at this second initiation zone, a phenomenon known as “coincidence detection” (LARKUM et al., 1999). This compartment coupling could be modulated by intrinsic structural alternations. It has been electrophysiologically shown that the number and distribution of apical oblique dendrites influence the occurrence of compartment coupling (SCHAEFER et al., 2003). While all available data derives from electrophysiology and functional imaging, it is structurally unknown how this mechanism could be modulated at a cellular innervation level. In this context it is generally unknown whether synaptic connections between neurons are established randomly, based on geometric proximity (Peters’ rule) or whether synapse formation follows highly specific wiring rules.

Electron microscopy alone provides the necessary imaging resolution to resolve even the smallest neuronal processes involved in synapse formation. The relatively novel technique of high-resolution connectomics aims at densely

mapping such synaptic wiring by the use of volume electron-microscopy (HELMSTAEDTER, 2013).

Using serial block-face electron microscopy (DENK and HORSTMANN, 2004), this study provides first cellular level insights on the innervation domains of the proximal apical trunk compartment and the apical oblique dendrites by visualizing and mapping chemical synapses in a 3D dataset from mouse barrel cortex. A set of 129 axons with a total path length of 57.75 mm establishing 4979 synapses were reconstructed. This work reveals that L5 apical dendrites receive specific inhibitory trunk innervations that were not found for L4 apical dendrites. Apical oblique dendrites receive additional excitatory shaft innervations, potentially pre-charging them and modifying the back-propagating potential. These additional excitatory shaft innervations were not found in a non-apical control group of dendrites. This work reports excitatory axons that preferentially innervate spine heads originating from apical dendrite trunks, for the first time implying excitatory innervation specificity. Geometric proximity as postulated by Peters' rule is shown to poorly predict excitatory innervations and to only partially predict inhibitory innervations. Although, this work provides first surprising results about the synaptic level peculiarities potentially modulating coincidence detection, further studies with combined functional and structural data on even larger neuronal tissue volumes are indicated to confirm and further explain these results.

VII. ZUSAMMENFASSUNG

Das Abrufen von Informationen über die Umgebung ist für jede Spezies von grundlegender Bedeutung. Während Menschen primär auf visuelle Wahrnehmung angewiesen sind, gewinnen Nagetiere wie Mäuse und Ratten die Mehrheit der sensorischen Inputs über taktile Informationen (VINCENT, 1912, DIAMOND et al., 2008). Verbiegungen von einzelnen Schnurrhaaren werden erkannt und zum somatosensorischen Kortex projiziert. Diese Stimuli werden in einem hoch spezifizierten Teilbereich dieses neokortikalen Bereichs, dem sogenannten „barrel cortex“ individuell verarbeitet. Es war in den letzten Jahrzehnten von großem Interesse, wie einzelne afferente Reize einzelner Schnurrhaare in anatomisch begrenzten Schaltkreisen, sogenannten „barrels“, verarbeitet werden (FELDMEYER et al., 2013). Eine besondere Frage in diesem Zusammenhang, die funktionell ausgiebig erforscht wurde, ist, wie Nervenzellen es schaffen, externe Wahrnehmungen wie Schnurrhaar-Stimuli mit intrinsischen Erfahrungen oder Inputs aus anderen kortikalen Bereichen zu verknüpfen um kortikale Ausgangssignale zu schalten die schließlich zu präzisen Verhaltensweisen führen (LARKUM, 2013). Es wurde gezeigt, dass Schicht fünf Pyramidenzellen mit besonderen elektrophysiologischen und strukturellen Eigenschaften ausgestattet sind, was sie zu einem vielversprechenden Kandidaten macht, um diese Aufgabe zu erfüllen. Diese Neurone gelten als kortikale Ausgangsneurone. Im Gegensatz zu anderen Zellen haben diese Neurone eine zweite dendritische Aktionspotenzial-Initiationszone an ihrem distalen apikalen Dendriten Kompartiment. Das Auftreten von unterschwelligen exzitatorischen postsynaptischen Potentialen (EPSPs) zusammen mit rückverbreitenden Aktionspotentialen löst Kalzium-Spikes in dieser zweiten Initiationszone aus, ein Phänomen, das als "Koinzidenzdetektion" bekannt ist (LARKUM et al., 1999). Diese Kompartimentkupplung kann durch intrinsische strukturelle Alternationen moduliert werden. Es wurde elektrophysiologisch gezeigt, dass die Anzahl und Verteilung der schrägen Apikaldendriten das Auftreten der Kompartimentkopplung beeinflussen (SCHAEFER et al., 2003). Während alle verfügbaren Daten aus der Elektrophysiologie und der funktionalen Bildgebung stammen, ist es strukturell unbekannt, wie dieser Mechanismus auf einer zellulären Innervationsebene moduliert werden könnte. In diesem Zusammenhang

ist es allgemein unbekannt, ob synaptische Verbindungen zwischen Neuronen nach dem Zufallsprinzip, basierend auf geometrischer Nähe („Peters-Regel“) oder ob die Synapsenbildung nach hochspezifischen Verbindungsregeln erfolgt.

Ausschließlich Elektronenmikroskopie liefert die notwendige Abbildungsauflösung, um auch die kleinsten neuronalen Prozesse, die an der Synapsenbildung beteiligt sind, darzustellen. Die relativ neuartige Technik der hochauflösenden Connectomics zielt darauf ab, mithilfe von Volumenelektronenmikroskopie (HELMSTAEDTER, 2013) genaue Kartierungen solcher synaptischer Schaltkreise zu erstellen.

Mit Hilfe der seriellen Block-Face-Elektronenmikroskopie (DENK und HORSTMANN, 2004) bietet diese Studie erste zelluläre Einblicke in die Innervationsdomänen des proximalen Teils des Apikaldendriten und der schrägen Apikaldendriten durch Visualisierung und Abbildung von chemischen Synapsen in einem 3D-Datensatz aus dem Mäuse „barrel cortex“. 129 Axone mit einer Gesamtlänge von 57,75 mm, die 4979 Synapsen formten, wurden rekonstruiert. Diese Arbeit zeigt, dass L5 Apikaldendriten spezifische inhibitorische Innervationen erhalten, die für L4 Apikaldendriten nicht gefunden wurden. Schräge apikal Dendriten erhalten zusätzliche exzitatorische Schaft-Innervationen, die sie möglicherweise voraufladen und das Rückverteilungspotential verändern. Diese zusätzlichen exzitatorischen Schaft-Innervationen wurden in einer nicht-apikalen Kontrollgruppe von Dendriten nicht gefunden. Diese Arbeit berichtet über exzitatorische Axone, die bevorzugt die Dornfortsätze apikaler Dendritstämme innervieren, was zum ersten Mal eine exzitatorische Innervationsspezifität impliziert. Die geometrische Nähe, wie sie von der „Peters-Regel“ postuliert wird, kann exzitatorische Innervationen schlecht und inhibitorische Innervationen nur teilweise vorhersagen. Obwohl diese Arbeit erste überraschende Ergebnisse über die synaptischen Besonderheiten bietet, die möglicherweise die Koinzidenzerkennung modulieren, sind weitere Untersuchungen mit kombinierten funktionalen und strukturellen Daten in noch größeren neuronalen Gewebevolumina angezeigt, um diese Ergebnisse zu bestätigen und weiter zu erklären.

VIII. LIST OF FIGURES

IX. LIST OF TABLES

X. LIST OF EQUATIONS

XI. REFERENCES

Agmon A, Connors BW. Repetitive burst-firing neurons in the deep layers of mouse somatosensory cortex. Neurosci Lett 1989; 99: 137-41.

Agmon A, Yang LT, O'Dowd DK, Jones EG. Organized growth of thalamocortical axons from the deep tier of terminations into layer IV of developing mouse barrel cortex. J Neurosci 1993; 13: 5365-82.

Amitai Y, Friedman A, Connors BW, Gutnick MJ. Regenerative activity in apical dendrites of pyramidal cells in neocortex. Cereb Cortex 1993; 3: 26-38.

Bayraktar T, Welker E, Freund TF, Zilles K, Staiger JF. Neurons immunoreactive for vasoactive intestinal polypeptide in the rat primary somatosensory cortex: morphology and spatial relationship to barrel-related columns. J Comp Neurol 2000; 420: 291-304.

Beierlein M, Gibson JR, Connors BW. Two dynamically distinct inhibitory networks in layer 4 of the neocortex. J Neurophysiol 2003; 90: 2987-3000.

Benshalom G, White EL. Quantification of thalamocortical synapses with spiny stellate neurons in layer IV of mouse somatosensory cortex. J Comp Neurol 1986; 253: 303-14.

Bernardo KL, McCasland JS, Woolsey TA, Strominger RN. Local intra- and interlaminar connections in mouse barrel cortex. J Comp Neurol 1990; 291: 231-55.

Berning M, Boergens KM, Helmstaedter M. SegEM: Efficient Image Analysis for High-Resolution Connectomics. Neuron 2015; 87: 1193-206.

Binzegger T, Douglas RJ, Martin KA. A quantitative map of the circuit of cat primary visual cortex. J Neurosci 2004; 24: 8441-53.

Bock DD, Lee WC, Kerlin AM, Andermann ML, Hood G, Wetzel AW, Yurgenson S, Soucy ER, Kim HS, Reid RC. Network anatomy and in vivo physiology of visual cortical neurons. Nature 2011; 471: 177-82.

Boergens KM, Berning M, Bocklisch T, Braunlein D, Drawitsch F, Frohnhofen J, Herold T, Otto P, Rzepka N, Werkmeister T, Werner D, Wiese G, Wissler H, Helmstaedter M. webKnossos: efficient online 3D data annotation for connectomics. Nat Meth 2017; advance online publication

Bohland JW, Wu C, Barbas H, Bokil H, Bota M, Breiter HC, Cline HT, Doyle JC, Freed PJ, Greenspan RJ, Haber SN, Hawrylycz M, Herrera DG, Hilgetag CC, Huang ZJ, Jones A, Jones EG, Karten HJ, Kleinfeld D, Kötter R, Lester HA, Lin JM, Mensh BD, Mikula S, Panksepp J, Price JL, Safdieh J, Saper CB, Schiff ND, Schmahmann JD, Stillman BW, Svoboda K, Swanson LW, Toga AW, Van Essen DC, Watson JD, Mitra PP. A Proposal for a Coordinated Effort for the Determination of Brainwide Neuroanatomical Connectivity in Model Organisms at a Mesoscopic Scale. PLoS Computational Biology 2009; 5: e1000334.

Boly M, Garrido MI, Gosseries O, Bruno MA, Boveroux P, Schnakers C, Massimini M, Litvak V, Laureys S, Friston K. Preserved feedforward but impaired top-down processes in the vegetative state. Science 2011; 332: 858-62.

Braitenberg V, Schüz A. Peters' Rule and White's Exceptions. In: Cortex: Statistics and Geometry of Neuronal Connectivity. Braitenberg V, Schüz A, eds. Berlin, Heidelberg: Springer Berlin Heidelberg 1998: 99-101.

Brecht M, Sakmann B. Dynamic representation of whisker deflection by synaptic potentials in spiny stellate and pyramidal cells in the barrels and septa of layer 4 rat somatosensory cortex. J Physiol 2002; 543: 49-70.

Briggman KL, Helmstaedter M, Denk W. Wiring specificity in the direction-selectivity circuit of the retina. Nature 2011; 471: 183-8.

Briggman KL, Bock DD. Volume electron microscopy for neuronal circuit

reconstruction. Curr Opin Neurobiol 2012; 22: 154-61.

Brown SP, Hestrin S. Intracortical circuits of pyramidal neurons reflect their long-range axonal targets. Nature 2009; 457: 1133-6.

Bullier J. Feedback connections and conscious vision. Trends Cogn Sci 2001; 5: 369-70.

Buzsaki G, Watson BO. Brain rhythms and neural syntax: implications for efficient coding of cognitive content and neuropsychiatric disease. Dialogues Clin Neurosci 2012; 14: 345-67.

Cauller L. Layer I of primary sensory neocortex: where top-down converges upon bottom-up. Behav Brain Res 1995; 71: 163-70.

Cauller LJ, Clancy B, Connors BW. Backward cortical projections to primary somatosensory cortex in rats extend long horizontal axons in layer I. J Comp Neurol 1998; 390: 297-310.

Chagnac-Amitai Y, Connors BW. Synchronized excitation and inhibition driven by intrinsically bursting neurons in neocortex. J Neurophysiol 1989; 62: 1149-62.

Chagnac-Amitai Y, Luhmann HJ, Prince DA. Burst generating and regular spiking layer 5 pyramidal neurons of rat neocortex have different morphological features. J Comp Neurol 1990; 296: 598-613.

Chiaia NL, Rhoades RW, Bennett-Clarke CA, Fish SE, Killackey HP. Thalamic processing of vibrissal information in the rat. I. Afferent input to the medial ventral posterior and posterior nuclei. J Comp Neurol 1991; 314: 201-16.

Chiaia NL, Fish SE, Bauer WR, Bennett-Clarke CA, Rhoades RW. Postnatal blockade of cortical activity by tetrodotoxin does not disrupt the formation of vibrissa-related patterns in the rat's somatosensory cortex. Brain Res Dev Brain

Res 1992; 66: 244-50.

Chklovskii DB, Vitaladevuni S, Scheffer LK. Semi-automated reconstruction of neural circuits using electron microscopy. Curr Opin Neurobiol 2010; 20: 667-75.

Chmielowska J, Carvell GE, Simons DJ. Spatial organization of thalamocortical and corticothalamic projection systems in the rat SmI barrel cortex. J Comp Neurol 1989; 285: 325-38.

Connors BW, Gutnick MJ, Prince DA. Electrophysiological properties of neocortical neurons in vitro. J Neurophysiol 1982; 48: 1302-20.

Connors BW, Gutnick MJ. Intrinsic firing patterns of diverse neocortical neurons. Trends Neurosci 1990; 13: 99-104.

Cowan AI, Stricker C. Functional connectivity in layer IV local excitatory circuits of rat somatosensory cortex. J Neurophysiol 2004; 92: 2137-50.

Czeiger D, White EL. Comparison of the distribution of parvalbumin-immunoreactive and other synapses onto the somata of callosal projection neurons in mouse visual and somatosensory cortex. J Comp Neurol 1997; 379: 198-210.

Daw MI, Ashby MC, Isaac JT. Coordinated developmental recruitment of latent fast spiking interneurons in layer IV barrel cortex. Nat Neurosci 2007; 10: 453-61.

de Kock CP, Bruno RM, Spors H, Sakmann B. Layer- and cell-type-specific suprathreshold stimulus representation in rat primary somatosensory cortex. J Physiol 2007; 581: 139-54.

de Nó RL (1922) La corteza cerebral del ratón:(Primera contribución.-La corteza acústica). Tipografía Artística

De Vivo L, Bellesi M, Marshall W, Bushong EA, Ellisman MH, Tononi G, Cirelli

C. Ultrastructural evidence for synaptic scaling across the wake/sleep cycle. Science 2017; 355: 507-10.

DeFelipe J, Hendry SH, Jones EG, Schmechel D. Variability in the terminations of GABAergic chandelier cell axons on initial segments of pyramidal cell axons in the monkey sensory-motor cortex. J Comp Neurol 1985; 231: 364-84.

DeFelipe J, Farinas I. The pyramidal neuron of the cerebral cortex: morphological and chemical characteristics of the synaptic inputs. Prog Neurobiol 1992; 39: 563-607.

Denk W, Strickler JH, Webb WW. Two-photon laser scanning fluorescence microscopy. Science 1990; 248: 73-6.

Denk W, Horstmann H. Serial block-face scanning electron microscopy to reconstruct three-dimensional tissue nanostructure. PLoS Biol 2004; 2: e329.

Deschenes M, Veinante P, Zhang ZW. The organization of corticothalamic projections: reciprocity versus parity. Brain Res Brain Res Rev 1998; 28: 286-308.

Diamond ME, von Heimendahl M, Knutsen PM, Kleinfeld D, Ahissar E. 'Where' and 'what' in the whisker sensorimotor system. Nat Rev Neurosci 2008; 9: 601-12.

Dörfl J. The innervation of the mystacial region of the white mouse: A topographical study. Journal of Anatomy 1985; 142: 173-84.

Douglas RJ, Martin KA. A functional microcircuit for cat visual cortex. J Physiol 1991; 440: 735-69.

Douglas RJ, Martin KA. Recurrent neuronal circuits in the neocortex. Curr Biol 2007; 17: R496-500.

Eberle AL, Mikula S, Schalek R, Lichtman J, Knothe Tate ML, Zeidler D. High-resolution, high-throughput imaging with a multibeam scanning electron microscope. J Microsc 2015; 259: 114-20.

Fairen A, Valverde F. A specialized type of neuron in the visual cortex of cat: a Golgi and electron microscope study of chandelier cells. J Comp Neurol 1980; 194: 761-79.

Fatt P. Sequence of events in synaptic activation of a motoneurone. J Neurophysiol 1957; 20: 61-80.

Feldman ML, Peters A. The forms of non-pyramidal neurons in the visual cortex of the rat. J Comp Neurol 1978; 179: 761-93.

Feldmeyer D, Egger V, Lubke J, Sakmann B. Reliable synaptic connections between pairs of excitatory layer 4 neurones within a single 'barrel' of developing rat somatosensory cortex. J Physiol 1999; 521 Pt 1: 169-90.

Feldmeyer D, Lubke J, Silver RA, Sakmann B. Synaptic connections between layer 4 spiny neurone-layer 2/3 pyramidal cell pairs in juvenile rat barrel cortex: physiology and anatomy of interlaminar signalling within a cortical column. J Physiol 2002; 538: 803-22.

Feldmeyer D, Roth A, Sakmann B. Monosynaptic connections between pairs of spiny stellate cells in layer 4 and pyramidal cells in layer 5A indicate that lemniscal and paralemniscal afferent pathways converge in the infragranular somatosensory cortex. J Neurosci 2005; 25: 3423-31.

Feldmeyer D, Lubke J, Sakmann B. Efficacy and connectivity of intracolumnar pairs of layer 2/3 pyramidal cells in the barrel cortex of juvenile rats. J Physiol 2006; 575: 583-602.

Feldmeyer D. Excitatory neuronal connectivity in the barrel cortex. Front

Neuroanat 2012; 6: 24.

Feldmeyer D, Brecht M, Helmchen F, Petersen CC, Poulet JF, Staiger JF, Luhmann HJ, Schwarz C. Barrel cortex function. Prog Neurobiol 2013; 103: 3-27.

Felleman DJ, Van Essen DC. Distributed hierarchical processing in the primate cerebral cortex. Cereb Cortex 1991; 1: 1-47.

Fox K (2008a) Barrel Cortex. Cambridge University Press. 51-5

Fox K (2008b) Barrel Cortex. Cambridge University Press. 6-7

Fox K (2008c) Barrel Cortex. Cambridge University Press. 56

Frick A, Feldmeyer D, Helmstaedter M, Sakmann B. Monosynaptic connections between pairs of L5A pyramidal neurons in columns of juvenile rat somatosensory cortex. Cereb Cortex 2008; 18: 397-406.

Furuta T, Kaneko T, Deschenes M. Septal neurons in barrel cortex derive their receptive field input from the lemniscal pathway. J Neurosci 2009; 29: 4089-95.

Gibson JR, Beierlein M, Connors BW. Two networks of electrically coupled inhibitory neurons in neocortex. Nature 1999; 402: 75-9.

Gilbert CD, Kelly JP. The projections of cells in different layers of the cat's visual cortex. J Comp Neurol 1975; 163: 81-105.

Gottlieb JP, Keller A. Intrinsic circuitry and physiological properties of pyramidal neurons in rat barrel cortex. Exp Brain Res 1997; 115: 47-60.

Gray EG. Axo-somatic and axo-dendritic synapses of the cerebral cortex: an electron microscope study. J Anat 1959; 93: 420-33.

Hallas BH, Jacquin MF. Structure-function relationships in rat brain stem subnucleus interpolaris. IX. Inputs from subnucleus caudalis. J Neurophysiol 1990; 64: 28-45.

Harris RM, Woolsey TA. Morphology of golgi-impregnated neurons in mouse cortical barrels following vibrissae damage at different post-natal ages. Brain Res 1979; 161: 143-9.

Hayworth KJ, Kasthuri N, Schalek R, Lichtman JW. Automating the Collection of Ultrathin Serial Sections for Large Volume TEM Reconstructions. Microscopy and Microanalysis 2006; 12: 86-7.

Hayworth KJ, Xu CS, Lu Z, Knott GW, Fetter RD, Tapia JC, Lichtman JW, Hess HF. Ultrastructurally smooth thick partitioning and volume stitching for large-scale connectomics. Nat Methods 2015; 12: 319-22.

Helmstaedter M, Briggman KL, Denk W. 3D structural imaging of the brain with photons and electrons. Curr Opin Neurobiol 2008a; 18: 633-41.

Helmstaedter M, Staiger JF, Sakmann B, Feldmeyer D. Efficient recruitment of layer 2/3 interneurons by layer 4 input in single columns of rat somatosensory cortex. J Neurosci 2008b; 28: 8273-84.

Helmstaedter M, Sakmann B, Feldmeyer D. The relation between dendritic geometry, electrical excitability, and axonal projections of L2/3 interneurons in rat barrel cortex. Cereb Cortex 2009a; 19: 938-50.

Helmstaedter M, Sakmann B, Feldmeyer D. Neuronal correlates of local, lateral, and translaminar inhibition with reference to cortical columns. Cereb Cortex 2009b; 19: 926-37.

Helmstaedter M, Feldmeyer D. Axons Predict Neuronal Connectivity Within and Between Cortical Columns and Serve as Primary Classifiers of Interneurons in a

Cortical Column. In: New Aspects of Axonal Structure and Function. Feldmeyer D, Lübke JHR, eds. Boston, MA: Springer US 2010: 141-55.

Helmstaedter M, Briggman KL, Denk W. High-accuracy neurite reconstruction for high-throughput neuroanatomy. Nat Neurosci 2011; 14: 1081-8.

Helmstaedter M. Cellular-resolution connectomics: challenges of dense neural circuit reconstruction. Nat Methods 2013; 10: 501-7.

Helmstaedter M, Briggman KL, Turaga SC, Jain V, Seung HS, Denk W. Connectomic reconstruction of the inner plexiform layer in the mouse retina. Nature 2013; 500: 168-74.

Henderson TA, Jacquin MF. What Makes Subcortical Barrels? In: The Barrel Cortex of Rodents. Jones EG, Diamond IT, eds. Boston, MA: Springer US 1995: 123-87.

Holcomb PS, Hoffpauir BK, Hoyson MC, Jackson DR, Deerinck TJ, Marrs GS, Dehoff M, Wu J, Ellisman MH, Spirou GA. Synaptic inputs compete during rapid formation of the calyx of Held: a new model system for neural development. J Neurosci 2013; 33: 12954-69.

Hua Y, Laserstein P, Helmstaedter M. Large-volume en-bloc staining for electron microscopy-based connectomics. Nat Commun 2015; 6: 7923.

Hubel DH, Wiesel TN. Shape and arrangement of columns in cat's striate cortex. J Physiol 1963; 165: 559-68.

Inda MC, Defelipe J, Munoz A. The distribution of chandelier cell axon terminals that express the GABA plasma membrane transporter GAT-1 in the human neocortex. Cereb Cortex 2007; 17: 2060-71.

Jacquin MF, Chiaia NL, Haring JH, Rhoades RW. Intersubnuclear connections

within the rat trigeminal brainstem complex. Somatosens Mot Res 1990; 7: 399-420.

Jacquin MF, Renehan WE, Rhoades RW, Panneton WM. Morphology and topography of identified primary afferents in trigeminal subnuclei principalis and oralis. J Neurophysiol 1993; 70: 1911-36.

Jain V, Seung HS, Turaga SC. Machines that learn to segment images: a crucial technology for connectomics. Curr Opin Neurobiol 2010; 20: 653-66.

Jiang X, Shen S, Sinz F, Reimer J, Cadwell CR, Berens P, Ecker AS, Patel S, Denfield GH, Froudarakis E, Li S, Walker E, Tolias AS. Response to Comment on “Principles of connectivity among morphologically defined cell types in adult neocortex”. Science 2016; 353: 1108.

Jones EG. Varieties and distribution of non-pyramidal cells in the somatic sensory cortex of the squirrel monkey. J Comp Neurol 1975; 160: 205-67.

Jones EG, Diamond IT (1995) The barrel cortex of rodents

Jones EGH, S.H.C. Basket Cells. In: Cerebral Cortex: Plenum Press New York 1984: 556.

Kasthuri N, Hayworth KJ, Berger DR, Schalek RL, Conchello JA, Knowles-Barley S, Lee D, Vazquez-Reina A, Kaynig V, Jones TR, Roberts M, Morgan JL, Tapia JC, Seung HS, Roncal WG, Vogelstein JT, Burns R, Sussman DL, Priebe CE, Pfister H, Lichtman JW. Saturated Reconstruction of a Volume of Neocortex. Cell 2015; 162: 648-61.

Keller A, White EL. Synaptic organization of GABAergic neurons in the mouse SmI cortex. J Comp Neurol 1987; 262: 1-12.

Killackey HP. Anatomical evidence for cortical subdivisions based on vertically

discrete thalamic projections from the ventral posterior nucleus to cortical barrels in the rat. Brain Res 1973; 51: 326-31.

Kim HG, Connors BW. Apical dendrites of the neocortex: correlation between sodium- and calcium-dependent spiking and pyramidal cell morphology. J Neurosci 1993; 13: 5301-11.

Kim JS, Greene MJ, Zlateski A, Lee K, Richardson M, Turaga SC, Purcaro M, Balkam M, Robinson A, Behabadi BF, Campos M, Denk W, Seung HS, EyeWirers. Space-time wiring specificity supports direction selectivity in the retina. Nature 2014; 509: 331-6.

Knott G, Marchman H, Wall D, Lich B. Serial section scanning electron microscopy of adult brain tissue using focused ion beam milling. J Neurosci 2008; 28: 2959-64.

Koelbl C, Helmstaedter M, Lubke J, Feldmeyer D. A barrel-related interneuron in layer 4 of rat somatosensory cortex with a high intrabarrel connectivity. Cereb Cortex 2015; 25: 713-25.

Koralek KA, Jensen KF, Killackey HP. Evidence for two complementary patterns of thalamic input to the rat somatosensory cortex. Brain Res 1988; 463: 346-51.

Kornfeld J, Benezra SE, Narayanan RT, Svara F, Egger R, Oberlaender M, Denk W, Long MA. EM connectomics reveals axonal target variation in a sequence-generating network. Elife 2017; 6

Kumar P, Ohana O. Inter- and intralaminar subcircuits of excitatory and inhibitory neurons in layer 6a of the rat barrel cortex. J Neurophysiol 2008; 100: 1909-22.

Land PW, Simons DJ. Cytochrome oxidase staining in the rat SmI barrel cortex. J Comp Neurol 1985; 238: 225-35.

Larkman A, Mason A. Correlations between morphology and electrophysiology of pyramidal neurons in slices of rat visual cortex. I. Establishment of cell classes. J Neurosci 1990; 10: 1407-14.

Larkman AU. Dendritic morphology of pyramidal neurones of the visual cortex of the rat: I. Branching patterns. J Comp Neurol 1991a; 306: 307-19.

Larkman AU. Dendritic morphology of pyramidal neurones of the visual cortex of the rat: III. Spine distributions. J Comp Neurol 1991b; 306: 332-43.

Larkum M. A cellular mechanism for cortical associations: an organizing principle for the cerebral cortex. Trends Neurosci 2013; 36: 141-51.

Larkum ME, Zhu JJ, Sakmann B. A new cellular mechanism for coupling inputs arriving at different cortical layers. Nature 1999; 398: 338-41.

Larkum ME, Zhu JJ, Sakmann B. Dendritic mechanisms underlying the coupling of the dendritic with the axonal action potential initiation zone of adult rat layer 5 pyramidal neurons. J Physiol 2001; 533: 447-66.

Larkum ME, Senn W, Luscher HR. Top-down dendritic input increases the gain of layer 5 pyramidal neurons. Cereb Cortex 2004; 14: 1059-70.

Larkum ME, Nevian T, Sandler M, Polsky A, Schiller J. Synaptic integration in tuft dendrites of layer 5 pyramidal neurons: a new unifying principle. Science 2009; 325: 756-60.

Larsen DD, Wickersham IR, Callaway EM. Retrograde tracing with recombinant rabies virus reveals correlations between projection targets and dendritic architecture in layer 5 of mouse barrel cortex. Front Neural Circuits 2007; 1: 5.

Le Be JV, Silberberg G, Wang Y, Markram H. Morphological, electrophysiological, and synaptic properties of corticocallosal pyramidal cells in

the neonatal rat neocortex. Cereb Cortex 2007; 17: 2204-13.

Lee KJ, Woolsey TA. A proportional relationship between peripheral innervation density and cortical neuron number in the somatosensory system of the mouse. Brain Res 1975; 99: 349-53.

Lee LJ, Erzurumlu RS. Altered parcellation of neocortical somatosensory maps in N-methyl-D-aspartate receptor-deficient mice. J Comp Neurol 2005; 485: 57-63.

Lee WC, Bonin V, Reed M, Graham BJ, Hood G, Glattfelder K, Reid RC. Anatomy and function of an excitatory network in the visual cortex. Nature 2016; 532: 370-4.

Lefort S, Tomm C, Floyd Sarria JC, Petersen CC. The excitatory neuronal network of the C2 barrel column in mouse primary somatosensory cortex. Neuron 2009; 61: 301-16.

Li X, Glazewski S, Lin X, Elde R, Fox K. Effect of vibrissae deprivation on follicle innervation, neuropeptide synthesis in the trigeminal ganglion, and S1 barrel cortex plasticity. J Comp Neurol 1995; 357: 465-81.

Lin CS, Lu SM, Schmechel DE. Glutamic acid decarboxylase immunoreactivity in layer IV of barrel cortex of rat and mouse. J Neurosci 1985; 5: 1934-9.

Lu SM, Lin RC. Thalamic afferents of the rat barrel cortex: a light- and electron-microscopic study using Phaseolus vulgaris leucoagglutinin as an anterograde tracer. Somatosens Mot Res 1993; 10: 1-16.

Lubke J, Egger V, Sakmann B, Feldmeyer D. Columnar organization of dendrites and axons of single and synaptically coupled excitatory spiny neurons in layer 4 of the rat barrel cortex. J Neurosci 2000; 20: 5300-11.

Lubke J, Roth A, Feldmeyer D, Sakmann B. Morphometric analysis of the

columnar innervation domain of neurons connecting layer 4 and layer 2/3 of juvenile rat barrel cortex. Cereb Cortex 2003; 13: 1051-63.

Ma PM, Woolsey TA. Cytoarchitectonic correlates of the vibrissae in the medullary trigeminal complex of the mouse. Brain Res 1984; 306: 374-9.

Ma PM. The barrelettes--architectonic vibrissal representations in the brainstem trigeminal complex of the mouse. I. Normal structural organization. J Comp Neurol 1991; 309: 161-99.

Mao T, Kusefoglu D, Hooks BM, Huber D, Petreanu L, Svoboda K. Long-range neuronal circuits underlying the interaction between sensory and motor cortex. Neuron 2011; 72: 111-23.

Markram H, Toledo-Rodriguez M, Wang Y, Gupta A, Silberberg G, Wu C. Interneurons of the neocortical inhibitory system. Nat Rev Neurosci 2004; 5: 793-807.

Martinotti C. Contributo allo studio della corteccia cerebrale, ed all'origine central dei nervi. Ann Freniatr Sci Affini. 1889;

McCormick DA, Connors BW, Lighthall JW, Prince DA. Comparative electrophysiology of pyramidal and sparsely spiny stellate neurons of the neocortex. J Neurophysiol 1985; 54: 782-806.

Merchan-Perez A, Rodriguez JR, Gonzalez S, Robles V, Defelipe J, Larranaga P, Bielza C. Three-dimensional spatial distribution of synapses in the neocortex: a dual-beam electron microscopy study. Cereb Cortex 2014; 24: 1579-88.

Meyer HS, Wimmer VC, Hemberger M, Bruno RM, de Kock CP, Frick A, Sakmann B, Helmstaedter M. Cell type-specific thalamic innervation in a column of rat vibrissal cortex. Cereb Cortex 2010a; 20: 2287-303.

Meyer HS, Wimmer VC, Oberlaender M, de Kock CP, Sakmann B, Helmstaedter M. Number and laminar distribution of neurons in a thalamocortical projection column of rat vibrissal cortex. Cereb Cortex 2010b; 20: 2277-86.

Meyer HS, Schwarz D, Wimmer VC, Schmitt AC, Kerr JN, Sakmann B, Helmstaedter M. Inhibitory interneurons in a cortical column form hot zones of inhibition in layers 2 and 5A. Proc Natl Acad Sci U S A 2011; 108: 16807-12.

Meyer K. Primary sensory cortices, top-down projections and conscious experience. Prog Neurobiol 2011; 94: 408-17.

Mikula S, Binding J, Denk W. Staining and embedding the whole mouse brain for electron microscopy. Nat Methods 2012; 9: 1198-201.

Mikula S, Denk W. High-resolution whole-brain staining for electron microscopic circuit reconstruction. Nat Methods 2015; 12: 541-6.

Mikula S. Progress Towards Mammalian Whole-Brain Cellular Connectomics. Front Neuroanat 2016; 10: 62.

Mikula S. In-Chamber Reel-to-Reel System for Random-Access Volume Electron Microscopy. Microscopy and Microanalysis 2017; 23: 154-5.

Mishchenko Y, Hu T, Spacek J, Mendenhall J, Harris KM, Chklovskii DB. Ultrastructural analysis of hippocampal neuropil from the connectomics perspective. Neuron 2010; 67: 1009-20.

Morgan JL, Berger DR, Wetzel AW, Lichtman JW. The Fuzzy Logic of Network Connectivity in Mouse Visual Thalamus. Cell 2016; 165: 192-206.

Mosconi TM, Rice FL. Sensory innervation of the mystacial pad fur of the ferret. Neurosci Lett 1991; 121: 199-202.

Mountcastle VB. Modality and topographic properties of single neurons of cat's somatic sensory cortex. J Neurophysiol 1957; 20: 408-34.

Mountcastle VB, Davies PW, Berman AL. Response properties of neurons of cat's somatic sensory cortex to peripheral stimuli. J Neurophysiol 1957; 20: 374-407.

Mountcastle VB, Powell TP. Neural mechanisms subserving cutaneous sensibility, with special reference to the role of afferent inhibition in sensory perception and discrimination. Bull Johns Hopkins Hosp 1959; 105: 201-32.

Mountcastle VB. "An Organizing Principle for Cerebral Function: The Unit Model and the Distributed System". In: The Mindful BrainMIT Press: MIT Press 1978: 7-41.

Niedworok CJ, Schwarz I, Ledderose J, Giese G, Conzelmann KK, Schwarz MK. Charting monosynaptic connectivity maps by two-color light-sheet fluorescence microscopy. Cell Rep 2012; 2: 1375-86.

Oberlaender M, Boudewijns ZS, Kleele T, Mansvelder HD, Sakmann B, de Kock CP. Three-dimensional axon morphologies of individual layer 5 neurons indicate cell type-specific intracortical pathways for whisker motion and touch. Proc Natl Acad Sci U S A 2011; 108: 4188-93.

Osten P, Margrie TW. Mapping brain circuitry with a light microscope. Nat Methods 2013; 10: 515-23.

Palade GE. A study of fixation for electron microscopy. J Exp Med 1952; 95: 285-98.

Palmer LM, Schulz JM, Murphy SC, Ledergerber D, Murayama M, Larkum ME. The cellular basis of GABA(B)-mediated interhemispheric inhibition. Science 2012; 335: 989-93.

Pascual-Leone A, Walsh V. Fast backprojections from the motion to the primary visual area necessary for visual awareness. Science 2001; 292: 510-2.

Pasternak JR, Woolsey TA. The number, size and spatial distribution of neurons in lamina IV of the mouse SmI neocortex. J Comp Neurol 1975; 160: 291-306.

Peters A, Feldman ML. The projection of the lateral geniculate nucleus to area 17 of the rat cerebral cortex. I. General description. J Neurocytol 1976; 5: 63-84.

Peters A, Kimerer LM. Bipolar neurons in rat visual cortex: a combined Golgi-electron microscope study. J Neurocytol 1981; 10: 921-46.

Peters A, Payne BR. Numerical relationships between geniculocortical afferents and pyramidal cell modules in cat primary visual cortex. Cereb Cortex 1993; 3: 69-78.

Peters A. Examining neocortical circuits: Some background and facts. Journal of Neurocytology 2002; 31: 183-93.

Pichon F, Nikonenko I, Kraftsik R, Welker E. Intracortical connectivity of layer VI pyramidal neurons in the somatosensory cortex of normal and barrelless mice. Eur J Neurosci 2012; 35: 855-69.

Porter JT, Cauli B, Staiger JF, Lambolez B, Rossier J, Audinat E. Properties of bipolar VIPergic interneurons and their excitation by pyramidal neurons in the rat neocortex. Eur J Neurosci 1998; 10: 3617-28.

Porter JT, Johnson CK, Agmon A. Diverse types of interneurons generate thalamus-evoked feedforward inhibition in the mouse barrel cortex. J Neurosci 2001; 21: 2699-710.

Potez S, Larkum ME. Effect of common anesthetics on dendritic properties in layer 5 neocortical pyramidal neurons. J Neurophysiol 2008; 99: 1394-407.

Radnikow G, Feldmeyer D, Lubke J. Axonal projection, input and output synapses, and synaptic physiology of Cajal-Retzius cells in the developing rat neocortex. J Neurosci 2002; 22: 6908-19.

Ragan T, Kadiri LR, Venkataraju KU, Bahlmann K, Sutin J, Taranda J, Arganda-Carreras I, Kim Y, Seung HS, Osten P. Serial two-photon tomography for automated ex vivo mouse brain imaging. Nat Methods 2012; 9: 255-8.

Ramón y Cajal S (1899) Textura del sistema nervioso del hombre y de los vertebrados : estudios sobre el plan estructural y composición histológica de los centros nerviosos adicionados de consideraciones fisiológicas fundadas en los nuevos descubrimientos. Madrid : N. Moya, 1899-1904.

Reid RC, Alonso JM. Specificity of monosynaptic connections from thalamus to visual cortex. Nature 1995; 378: 281-4.

Reyes A, Lujan R, Rozov A, Burnashev N, Somogyi P, Sakmann B. Target-cell-specific facilitation and depression in neocortical circuits. Nat Neurosci 1998; 1: 279-85.

Reyes A, Sakmann B. Developmental switch in the short-term modification of unitary EPSPs evoked in layer 2/3 and layer 5 pyramidal neurons of rat neocortex. J Neurosci 1999; 19: 3827-35.

Rice FL, Gomez C, Barstow C, Burnet A, Sands P. A comparative analysis of the development of the primary somatosensory cortex: interspecies similarities during barrel and laminar development. J Comp Neurol 1985; 236: 477-95.

Riddle DR, Purves D. Individual variation and lateral asymmetry of the rat primary somatosensory cortex. J Neurosci 1995; 15: 4184-95.

Rockland KS, Pandya DN. Laminar origins and terminations of cortical connections of the occipital lobe in the rhesus monkey. Brain Res 1979; 179: 3-

20.

Rodriguez-Moreno J, Rollenhagen A, Arlandis J, Santuy A, Merchan-Pérez A, DeFelipe J, Lübke J, Clasca F. Quantitative 3D Ultrastructure of Thalamocortical Synapses from the “Lemniscal” Ventral Posteromedial Nucleus in Mouse Barrel Cortex. Cereb Cortex 2017;

Schaefer AT, Larkum ME, Sakmann B, Roth A. Coincidence detection in pyramidal neurons is tuned by their dendritic branching pattern. J Neurophysiol 2003; 89: 3143-54.

Schalek R, Kasthuri N, Hayworth K, Berger D, Tapia J, Morgan J, Turaga S, Fagerholm E, Seung H, Lichtman J. Development of High-Throughput, High-Resolution 3D Reconstruction of Large-Volume Biological Tissue Using Automated Tape Collection Ultramicrotomy and Scanning Electron Microscopy. Microscopy and Microanalysis 2011; 17: 966-7.

Schiller J, Schiller Y, Stuart G, Sakmann B. Calcium action potentials restricted to distal apical dendrites of rat neocortical pyramidal neurons. J Physiol 1997; 505 (Pt 3): 605-16.

Schubert D, Staiger JF, Cho N, Kotter R, Zilles K, Luhmann HJ. Layer-specific intracolumnar and transcolumnar functional connectivity of layer V pyramidal cells in rat barrel cortex. J Neurosci 2001; 21: 3580-92.

Schubert D, Kotter R, Zilles K, Luhmann HJ, Staiger JF. Cell type-specific circuits of cortical layer IV spiny neurons. J Neurosci 2003; 23: 2961-70.

Seligman AM, Hanker JS, Wasserkrug H, Dmochowski H, Katzoff L. Histochemical demonstration of some oxidized macromolecules with thiocarbohydrazide (tch) or thiosemicarbazide (TSC) and osmium tetroxide. J Histochem Cytochem 1965; 13: 629-39.

Shepherd GM, Stepanyants A, Bureau I, Chklovskii D, Svoboda K. Geometric and functional organization of cortical circuits. Nat Neurosci 2005; 8: 782-90.

Shu Y, Hasenstaub A, McCormick DA. Turning on and off recurrent balanced cortical activity. Nature 2003; 423: 288-93.

Silberberg G, Markram H. Disynaptic inhibition between neocortical pyramidal cells mediated by Martinotti cells. Neuron 2007; 53: 735-46.

Simons DJ, Woolsey TA. Morphology of Golgi-Cox-impregnated barrel neurons in rat SmI cortex. J Comp Neurol 1984; 230: 119-32.

Soltani A, Koch C. Visual saliency computations: mechanisms, constraints, and the effect of feedback. J Neurosci 2010; 30: 12831-43.

Somogyi P. A specific 'axo-axonal' interneuron in the visual cortex of the rat. Brain Res 1977; 136: 345-50.

Somogyi P, Freund TF, Cowey A. The axo-axonic interneuron in the cerebral cortex of the rat, cat and monkey. Neuroscience 1982; 7: 2577-607.

Staffler B, Berning M, Boergens KM, Gour A, van der Smagt P, Helmstaedter M. SynEM, automated synapse detection for connectomics. Elife 2017; 6

Staiger JF, Zilles K, Freund TF. Distribution of GABAergic elements postsynaptic to ventroposteromedial thalamic projections in layer IV of rat barrel cortex. Eur J Neurosci 1996; 8: 2273-85.

Staiger JF, Flagmeyer I, Schubert D, Zilles K, Kotter R, Luhmann HJ. Functional diversity of layer IV spiny neurons in rat somatosensory cortex: quantitative morphology of electrophysiologically characterized and biocytin labeled cells. Cereb Cortex 2004; 14: 690-701.

Staiger JF, Loucif AJ, Schubert D, Mock M. Morphological Characteristics of Electrophysiologically Characterized Layer Vb Pyramidal Cells in Rat Barrel Cortex. PLoS One 2016; 11: e0164004.

Stuart G, Schiller J, Sakmann B. Action potential initiation and propagation in rat neocortical pyramidal neurons. J Physiol 1997a; 505 (Pt 3): 617-32.

Stuart G, Spruston N, Sakmann B, Hausser M. Action potential initiation and backpropagation in neurons of the mammalian CNS. Trends Neurosci 1997b; 20: 125-31.

Stuart GJ, Sakmann B. Active propagation of somatic action potentials into neocortical pyramidal cell dendrites. Nature 1994; 367: 69-72.

Szentágothai J. The ‘module-concept’ in cerebral cortex architecture. Brain Research 1975; 95: 475-96.

Takemura SY, Bharioke A, Lu Z, Nern A, Vitaladevuni S, Rivlin PK, Katz WT, Olbris DJ, Plaza SM, Winston P, Zhao T, Horne JA, Fetter RD, Takemura S, Blazek K, Chang LA, Ogundeyi O, Saunders MA, Shapiro V, Sigmund C, Rubin GM, Scheffer LK, Meinertzhagen IA, Chklovskii DB. A visual motion detection circuit suggested by Drosophila connectomics. Nature 2013; 500: 175-81.

Tapia JC, Kasthuri N, Hayworth KJ, Schalek R, Lichtman JW, Smith SJ, Buchanan J. High-contrast en bloc staining of neuronal tissue for field emission scanning electron microscopy. Nat Protoc 2012; 7: 193-206.

Thomson AM, Deuchars J. Synaptic interactions in neocortical local circuits: dual intracellular recordings in vitro. Cereb Cortex 1997; 7: 510-22.

Titze B, Denk W. Automated in-chamber specimen coating for serial block-face electron microscopy. J Microsc 2013; 250: 101-10.

Tomassy GS, Berger DR, Chen HH, Kasthuri N, Hayworth KJ, Vercelli A, Seung HS, Lichtman JW, Arlotta P. Distinct profiles of myelin distribution along single axons of pyramidal neurons in the neocortex. Science 2014; 344: 319-24.

Turaga SC, Murray JF, Jain V, Roth F, Helmstaedter M, Briggman K, Denk W, Seung HS. Convolutional networks can learn to generate affinity graphs for image segmentation. Neural Comput 2010; 22: 511-38.

Valente S, Ringwood J, Mangourova V, Lowry J (2012) Investigation of events in the EEG signal correlated with changes in both oxygen and glucose in the brain. IET Irish Signals and Systems Conference (ISSC 2012), 28-29 June 2012. 1-6

Van Der Loos H. Barreloids in mouse somatosensory thalamus. Neurosci Lett 1976; 2: 1-6.

Veinante P, Deschenes M. Single- and multi-whisker channels in the ascending projections from the principal trigeminal nucleus in the rat. J Neurosci 1999; 19: 5085-95.

Veinante P, Lavallee P, Deschenes M. Corticothalamic projections from layer 5 of the vibrissal barrel cortex in the rat. J Comp Neurol 2000a; 424: 197-204.

Veinante P, Jacquin MF, Deschenes M. Thalamic projections from the whisker-sensitive regions of the spinal trigeminal complex in the rat. J Comp Neurol 2000b; 420: 233-43.

Viaene AN, Petrof I, Sherman SM. Properties of the thalamic projection from the posterior medial nucleus to primary and secondary somatosensory cortices in the mouse. Proc Natl Acad Sci U S A 2011; 108: 18156-61.

Vincent SB (1912) The functions of the vibrissae in the behavior of the white rat, [Cambridge, Mass. 81 p.

Wang Y, Gupta A, Toledo-Rodriguez M, Wu CZ, Markram H. Anatomical, physiological, molecular and circuit properties of nest basket cells in the developing somatosensory cortex. Cereb Cortex 2002; 12: 395-410.

Wang Y, Toledo-Rodriguez M, Gupta A, Wu C, Silberberg G, Luo J, Markram H. Anatomical, physiological and molecular properties of Martinotti cells in the somatosensory cortex of the juvenile rat. J Physiol 2004; 561: 65-90.

Wanner AA, Genoud C, Masudi T, Siksou L, Friedrich RW. Dense EM-based reconstruction of the interglomerular projectome in the zebrafish olfactory bulb. Nat Neurosci 2016; 19: 816-25.

Watson ML. Staining of tissue sections for electron microscopy with heavy metals. II. Application of solutions containing lead and barium. J Biophys Biochem Cytol 1958; 4: 727-30.

Welker C, Woolsey TA. Structure of layer IV in the somatosensory neocortex of the rat: description and comparison with the mouse. J Comp Neurol 1974; 158: 437-53.

White EL, Hersch SM. A quantitative study of thalamocortical and other synapses involving the apical dendrites of corticothalamic projection cells in mouse SmI cortex. J Neurocytol 1982; 11: 137-57.

White EL, Keller A. Intrinsic circuitry involving the local axon collaterals of corticothalamic projection cells in mouse SmI cortex. J Comp Neurol 1987; 262: 13-26.

White EL, Peters A. Cortical modules in the posteromedial barrel subfield (Sml) of the mouse. J Comp Neurol 1993; 334: 86-96.

White JG, Southgate E, Thomson JN, Brenner S. The structure of the nervous system of the nematode Caenorhabditis elegans. Philos Trans R Soc Lond B Biol

Sci 1986; 314: 1-340.

Williams SR, Stuart GJ. Mechanisms and consequences of action potential burst firing in rat neocortical pyramidal neurons. J Physiol 1999; 521 Pt 2: 467-82.

Williams SR, Stuart GJ. Dependence of EPSP efficacy on synapse location in neocortical pyramidal neurons. Science 2002; 295: 1907-10.

Wimmer VC, Bruno RM, de Kock CP, Kuner T, Sakmann B. Dimensions of a projection column and architecture of VPM and POm axons in rat vibrissal cortex. Cereb Cortex 2010; 20: 2265-76.

Woodruff AR, Anderson SA, Yuste R. The enigmatic function of chandelier cells. Front Neurosci 2010; 4: 201.

Woolsey TA, Van der Loos H. The structural organization of layer IV in the somatosensory region (SI) of mouse cerebral cortex. The description of a cortical field composed of discrete cytoarchitectonic units. Brain Res 1970; 17: 205-42.

Woolsey TA, Welker C, Schwartz RH. Comparative anatomical studies of the SmL face cortex with special reference to the occurrence of "barrels" in layer IV. J Comp Neurol 1975; 164: 79-94.

Wyffels JT. Principles and Techniques of Electron Microscopy: Biological Applications, Fourth Edition, by M. A. Hayat. Microsc Microanal 2001; 7: 66.

Xu X, Callaway EM. Laminar specificity of functional input to distinct types of inhibitory cortical neurons. J Neurosci 2009; 29: 70-85.

Yanez IB, Munoz A, Contreras J, Gonzalez J, Rodriguez-Veiga E, DeFelipe J. Double bouquet cell in the human cerebral cortex and a comparison with other mammals. J Comp Neurol 2005; 486: 344-60.

Yuste R, Gutnick MJ, Saar D, Delaney KR, Tank DW. Ca2+ accumulations in dendrites of neocortical pyramidal neurons: an apical band and evidence for two functional compartments. Neuron 1994; 13: 23-43.

Zhang ZW, Deschenes M. Intracortical axonal projections of lamina VI cells of the primary somatosensory cortex in the rat: a single-cell labeling study. J Neurosci 1997; 17: 6365-79.

XII. DANKSAGUNG

Mein besonderer Dank gilt Herrn Dr. Moritz Helmstaedter und Frau Prof. Dr. Heidrun Potschka für die Betreuung der Arbeit. Bei Herrn Dr. Helmstaedter möchte ich mich insbesondere für die Planung und Anleitung des Projekts, die zahlreichen wissenschaftlichen Diskussionen sowie das Ermöglichen mehrerer internationaler Konferenzbesuche bedanken.

Dr. Yunfeng Hua danke ich für die umfassende Unterstüzung und Beratung, die Einarbeitung in das Labor sowie die gemeinsame Zeit an Projekten und auf Konferenzen, die ich in sehr guter Erinnerung behalten werde. Desweiteren möchte ich mich bei ihm für die zahlreichen interessanten wissenschaftlichen und privaten Diskussionen sowie das Korrekturlesen dieser Arbeit bedanken.

Helene Schmidt und Kevin Boergens danke ich für die Hilfe und Anleitung bei der Bedienung des Magellan SBEM Setups. Kevin Boergens möchte ich außerdem für die zahlreichen erheiternden und phantasievollen Gespräche danken.

Manuel Berning danke ich für die ausgiebigen Hilfestellungen beim Programmieren, sowie bei Problemen aller Art. Einen Kollegen wie ihn kann man sich nur wünschen, ich werde unsere Diskussionen, die manchmal auch in den Bereich der Philosophie abdrifteten vermissen.

Philipp Bastians möchte ich für die Einführung in das Labor in Martinsired, das Quanta SBEM Setup, gemeinsame Experimente, die gemeinsame Doktorandenzeit, die gemeinsamen Laufeinheiten und sein stets offenes Ohr danken, er war in schwierigen Zeiten immer sehr hilfreich und wird mir als Freund erhalten bleiben.

Benedikt Staffler, Allessandro Motta und Emmanuel Klinger möchte ich für ihre Hilfe bei Codeproblemen und die interessanten Gespräche danken.

Jakob Strähle möchte ich für den wissenschaftlichen Austausch sowie die vielen unterhaltsamen Gespräche danken.

Heiko Wissler danke ich für 3D –Visualisierungen sowie Fehlerbehebungen bei WebKnossos.

Anjali Gour danke ich für den wissenschaftlichen Austausch sowie die

Bereitstellung einer Visualisierung für diese Arbeit (Figure 26).

Ein besonderer Dank geht auch an meine Familie, die mich stets unterstützt hat und maßgeblich zu meinem bisherigen Lebensweg beigetragen hat. Meiner Freundin Mona Schleibinger danke ich für ihre verständnisvolle und liebevolle Art, die mir bei der Anfertigung dieser Arbeit viel Kraft gegeben hat. Ebenso bedanke ich mich bei meinen Freunden Victor Güttler, Mark Rassner und Felix Busch, die mich seit nunmehr 20 Jahren auf meinem Lebensweg begleiten und mir stets mit gutem Rat und ihrer Freundschaft zur Seite standen. Zuletzt danke ich Jens Becker und Teut Kürn für die gemeinsame Studienzeit, ihre Freundschaft und ihre persönlichen Ratschläge.